

# 國立交通大學

光電工研究所  
博士論文

光電式次兆赫波發射器及其應用  
之研究

A Study of Sub-THz Impulse Radio  
Photonic Devices and Application

研究生：黎宇泰

指導教授：潘犀靈 教授

趙如蘋 教授

中華民國九十八年七月

光電式次兆赫波發射器及其應用之研究

A Study of Sub-THz Impulse Radio Photonic  
Devices and Application

研 究 生：黎宇泰                      Student : Yu-Tai Li  
指 導 教 授：潘犀靈 博士            Advisor: Prof. Ci-Ling Pan  
                 趙如蘋 博士                      Prof. Ru-Pin Chao Pan

國 立 交 通 大 學  
光 電 工 程 研 究 所  
博 士 論 文

A Thesis  
Submitted to Department of Photonics  
National Chiao Tung University  
in Partial Fulfillment of the Requirements  
for the Degree of  
Doctor  
in  
Electro-Optical Engineering

July 2009  
Hsinchu, Taiwan, Republic of China

中 華 民 國 九 十 八 年 七 月

# 光電式次兆赫波發射器及其應用之研究

研究生：黎宇泰

指導教授：潘犀靈 教授

趙如蘋 教授

國立交通大學光電工程研究所

## 摘要

在本論文中，我們研究可利用短脈衝雷射激發之次兆赫波(0.1~1THz)發射器，包括結合高速光電二極體和印刷天線之次兆赫波發射器以及光導天線兩種型式。不同型式的元件可產生不同波段之脈衝訊號，我們探討此頻段相關量測系統，元件特性，以及探討其在寬頻傳輸之應用。

首先我們以波長為 800nm 短脈衝鈦藍寶石雷射激發，以產生出高功率次兆赫波輻射，並予以調制；本研究中首先探討分別由改良利用低溫成長砷化鎵(LTG-GaAs)為基材的分離式傳輸複合光二極體 (STR-PD)以及以砷化鎵/砷化鋁鎵(GaAs/AlGaAs)為基材的單載子傳輸光二極體(UTC-PD)，並結合溝槽天線以及單極圓碟微波天線之次兆赫波激發器之輻射效率以及其操作行為，以符合寬頻通訊實驗所需。研究中成功分別驗證了：(1)中心頻率 100GHz(約 75GHz~120GHz)以及(2)中心頻率 500GHz 的高功率輻射元件之可行性。我們並詳細的探討此兩種不同的高速二極體結合相同結構之寬頻天線對於兆赫波發射之效果，研究顯示此兩種設計存在截然不同電流響應機制，但皆具有高功率之輻射輸出功率。

此外，短脈衝雷射亦可激發光導天線以產生兆赫輻射。我們嘗試利用製作程序較為簡單之多重氧離子佈值之砷化鎵(GaAs:O) 光導天線取代傳統低溫砷化鎵

(LT-GaAs)做為激發器，並探討其性質差異。我們量測多重氧離子佈植砷化鎵 ( $2.5 \times 10^{13}$  ions/cm<sup>2</sup> (500 keV & 800 keV),  $4 \times 10^{13}$  ions/cm<sup>2</sup> (1200 keV) 薄膜材料和低溫成長之砷化鎵製程之光導天線，驗證其材料替代之可行性。本研究除探討此兩種光導天線在高偏壓下操作之飽和現象外，亦驗證其產生連續兆赫波之可行性。

對於兆赫波與次兆赫波之量測，除了可利用 800nm 之鈦藍寶石鎖模脈衝雷射以及 1550nm 光纖雷射做為激發源外，本研究中也架設了利用 800nm 雷射二極體拍頻連續波激發系統，可做為連續波兆赫波激發之用。在量測此高頻微波的功率方面，除了分別利用熱輻射儀量測並比較各元件之絕對功率外，也架設基於低溫砷化鎵光導天線之時域光譜儀，以量測元件輻射出來之電場以及傅式轉換後之頻譜。為了進一步展示次兆赫波寬頻通訊系統，也架設了一利用高速號角天線(W 頻段, 75~110 GHz)做為接受器之寬頻通訊系統，以提高系統之資料傳輸率。

最後在次兆赫波發射器在寬頻通訊應用部分，我們分別做了以下展示: (1) 以 Manchester 編碼用改善通訊系統之傳輸品質以及(2)以光纖鎖模脈衝雷射(波長為 1550nm)為系統光源以產生寬頻載波(W 頻段, 75~110GHz)，並量測此系統之最高資料傳輸率。在第一部份我們在利用鈦藍寶石鎖模雷射做為激發光源，並以低溫砷化鎵光導天線做為系統之傳輸接收器，成功的將誤碼率由  $10^{-8}$  降低到  $10^{-12}$ 。在第二部分，我們利用了光纖鎖模雷射之高脈衝重覆率的優點，成功的展示了在 W 頻段下 2.5Gbit/s 的高資料傳輸率。

# A Study of Sub-THz Impulse Radio Photonic Devices and Application

Student: Yu-Tai Li

Advisor: Prof. Ci-Ling Pan

Prof. Ru-Pin Chao Pan

Institute of Electro-Optical Engineering  
College of Electrical Engineering and Computer Science  
National Chiao Tung University

## **ABSTRACT**

This study investigates of the key components of optical electrical devices operating in the THz and Sub-THz range (0.1~1THz), including photoconductive (PC) antennas and photonic transmitters (PTs). PTs are integrated high speed photo diodes with printed planar antennas designed based on the required radiation frequency range. This study also examines related high frequency measurement systems and broadband communication applications.

The feasibility of several novel photonic transmitters is demonstrated first, which are designed for high peak power generation and wireless ultra-wideband (UWB) communication. Initially, the feasibility of a PT composed of a low-temperature-grown GaAs (LTG-GaAs) based separated-transport-recombination photodiode (STR-PD)

and a micromachined slots antenna is demonstrated. Under femto-second (fs) optical pulse illumination, this device radiates strong electrical pulses (300 mW peak power) at a designed frequency of 500GHz. A traditional LTG-GaAs based PT under high, externally applied electrical fields ( $>50\text{kV/cm}$ ) is then eliminated using our STR-PD based PTs (STR-PTs). Monolithic integration of a GaAs/AlGaAs based uni-traveling-carrier photodiode (UTC-PD) with a broadband micromachined antenna creates UTC-PD based PTs (UTC-PTs) that can also radiate strong sub-THz pulses (20mW peak-power) with a narrow pulse-width ( $<2\text{ps}$ ) and wide bandwidth (100~250GHz). The bias dependent peak output-power of both PTs (UTC- and STR-PD based) makes them highly promising for use as a data modulator/emitter for a photonic UWB system.

This study also describes in detail the characterization of two high power PTs based on two high power photodiodes, UTC-PD and STR-PD. Both PDs have the same depletion layer thickness, i.e. the same theoretical RC-limited bandwidth, and are monolithically integrated with the same broadband micro-machined circular disk monopole antennas. However, the STR-PD based transmitter exhibits a significantly different dynamic and static performance from that of the UTC-PD based transmitter due to a low temperature grown GaAs (LTG-GaAs) based recombination center inside the active region, as well as a much thinner thickness of an effective depletion layer. Under optical pulse excitation ( $\sim 480\text{pJ/pulse}$ ), the STR-PD based transmitter exhibits a markedly lower maximum average output photocurrent (1.2mA vs. 0.3mA) than that of the UTC-PD transmitter. This is despite the fact that the radiated electrical pulse width and maximum peak power, which are determined by the same THz time domain spectroscopic (TDS) system, of both devices are comparable.

Next, high power THz generation by using PC antennas is studied by comparing

the emission properties of LT-GaAs PC antennas with GaAs:O PC antennas in the pulse and CW mode. GaAs:O PC antennas can generate a higher THz power than LT-GaAs based both in the pulsed and CW modes. The bandwidths of GaAs:O PC antennas and LT-GaAs PC antennas are measured at approximately 1THz both under pulse (TDS) and CW (photomixing) pumping. However, the THz power of LT-GaAs PC antenna becomes saturated in CW mode, while GaAs:O does not. This finding suggests that GaAs:O PC antenna is a more reliable THz emitter than LT-GaAs, which is difficult to reproduce.

To excite THz and Sub-THz radiation, not only are a Ti:Sapphire laser ( $\lambda=800\text{nm}$ ) and fiber mode locked laser ( $\lambda=1550\text{nm}$ ) used, but a CW excitation system is also established, which consists of two laser diodes ( $\lambda=800\text{nm}$ ). The radiated powers of all devices are compared using a Helium-cooled bolometer. Additionally, radiated electrical fields are measured by a TDS system, which is based on LTG-PC antennas. The power spectrum of devices can be determined following fast Fourier transformation (FFT). A wideband communication system is also adopted by using a high speed horn (W band, 75~110GHz) antenna as a receiver to demonstrate the effectiveness of sub-THz wideband communication, which displays an improved data transmission rate.

Finally, this study demonstrates the feasibility of wideband communication applications by using our sub-THz emitters as follows: (1) Communication quality of the LTG-GaAs PC antennas based TDS system is improved by using Manchester coding; and (2) A wideband carrier (W band, 75~110GHz) is generated by using a fiber mode-locked laser as system optical source and determining its maximum data transmission rate. In (1), the Ti: Sapphire laser is adopted as the excitation source and we demonstrate that the bit error rate (BER) improved from  $10^{-8}$  to  $10^{-12}$  by using

Manchester coding. In (2), data transmission of 2.5Gbit/s at W band is successfully demonstrated by utilizing the advantage of a high repetition rate of fiber mode-locked laser.



# Acknowledgements

The author would like to express his gratitude to Professor Ci-Ling Pan and Professor Ru-Pin Pan for providing the opportunity to conduct this research and their advice and supervision during research period.

I am also grateful for the assistance of Professor Jin-Wei Shi and Professor Chi-Wai Chow, especially for their contribution to patiently guide me on my research.

Thanks are also given to group members of the Laser and Electro-Optic (LEO) Laboratory and Liquid Physics Laboratory. I need to appreciate many friends in both groups for their support and company. Without you, it must be very hard to finish many experiments smoothly.

I would also like to thank many friends and cooperation partners whether in the assistance about my life or research. It is really glad and helpful for me to meet you during these years.

Special thanks to my parents, dear members of my family, and my girl friend. Because of your consideration and encouragement, I could concentrate on my research work.

Finally, the thesis is dedicated to all the people who care for me.

Thanks all of you, sincerely.

# Contents

光電式次兆赫波發射器及其應用之研究.....	i
A Study of Sub-THz Impulse Radio Photonic Devices and Application.....	iii
Acknowledgements.....	vii
Contents .....	viii
List of Figures.....	xi
List of Tables Pages .....	xvii
Chapter 1 Introduction .....	1
1-1 THz Gap .....	1
1-2 THz Impulse Radio Communication.....	4
1-3 Generation of Sub-THz Pulses .....	10
1-4 Photodiode Based Photonic Transmitters.....	13
1-5 Low Temperature Grown Based GaAs (LTG-GaAs) or Ion-implanted Materials Based PC Antennas .....	15
1-6 Organization of Dissertation.....	16
Reference .....	19
Chapter 2 THz Photonic Transmitters.....	24
2-1 Introduction .....	24
2-2 Basic Theory.....	27
2-3 Separated-Transport-Recombination Photodiode (STR-PD) .....	31
2-4 Uni-Traveling-Carrier Photodiode (UTC-PD) .....	37
2-5 STR-PD Integrated with Slot Antennas.....	41
2-6 STR/ UTC-PD integrated with Circular Antenna.....	44

Reference .....	48
Chapter 3 Photoconductive Antennas .....	53
3-1 Introduction .....	53
3-2 Basic Theory .....	56
3-3 Material of Photoconductive Antenna .....	61
3-4 Antenna Types .....	63
3-5 Properties of Photoconductive Antennas .....	64
Reference .....	69
Chapter 4 Experimental Methods for Characterization of THz Waves .....	74
4-1 Introduction .....	74
4-2 Power Measurement .....	75
4-2-1 Bolometer .....	75
4-3 Waveform of Spectrum Measurement .....	78
4-3-1 Martin-Puplett Polarization Interferometer .....	78
4-3-2 THz Time Domain Spectrometer .....	82
Reference .....	84
Chapter 5 Performances of THz and Sub-THz Emitters.....	85
5-1 LTG-GaAs & GaAs :O PC Antennas under Pulse Excitation .....	85
5-2 LTGaAs & GaAs :O PC Antennas under CW Excitation.....	91
5-3 STR-PD Combined with Slot Antennas .....	97
5-4 Comparison of UTC-PT and STR-PT .....	101
Reference .....	112
Chapter 6 Sub-THz Impulse Radio Communication.....	115
6-1 Introduction .....	115
6-2 Frequency Response of Communication Link System.....	117

6-3 Manchester Coding to Improve Link Reliability.....	120
6-4 Impulse Radio Communication under 1550nm Wavelength.....	123
Reference .....	129
Chapter 7 Conclusion and Future Work.....	131
7-1 Conclusion.....	131
7-2 Future Work .....	133
Appendix A .....	135
Publication list .....	137
Curriculum Vita.....	141

# List of Figures

## Chapter 1

Figure 1- 1 Electromagnetic wave spectrum .....	1
Figure 1- 2 Some examples of THz application .....	2
Figure 1- 3 Terahertz gap with respect to source technology. ....	3
Figure 1- 4 The regulated spectrum as designated by the U.S. Federal Communications Commission .....	5
Figure 1- 5 Progress of transmission bits rate for different communication technology .....	6
Figure 1- 6 Diagram of radio-over-fiber communication system .....	7
Figure 1- 7 A vision proposed from NTT to transmitted data >10Gbit/s wireless ....	8
Figure 1- 8 Transmission spectrums .....	9
Figure 1- 9 Attenuation spectrums in rainy day .....	10
Figure 1- 10 Commercial Ti: Sapphire mode locked laser .....	12
Figure 1- 11 Commercial compact Ti: Sapphire mode locked laser .....	12
Figure 1- 12 Schematic of optical heterodyne signal generation in an photonic local oscillator (PLO) .....	13
Figure 1- 13 Schematic of a photonic transmitter consisting of a TWPD monolithically integrated with a planar full-wave single slot antenna	14

## Chapter 2

Figure 2- 1 (a) Vertically incident PD and (b) edge coupled incident PD .....	28
Figure 2- 2 Scheme of travelling wave photodiode .....	30

Figure 2- 3 An effective diagram of the device .....	30
Figure 2- 4(a)Equivalent circuit of photo diode and (b) simplified equivalent circuit of photo diode.....	31
Figure 2- 5 A schematic drawing of energy band and electric field distributed for traditional GaAs PD under high power excitation.....	32
Figure 2- 6 Traditional LTG-GaAs PD energy band diagram and electrical field distribution.....	34
Figure 2- 7 A scheme of change for trap energy band .....	34
Figure 2- 8 Schematic diagram of energy band and electrical field for STR-PD....	35
Figure 2- 9 A schematic diagram of electrical field distribution for STR-PD while applied higher external field.....	36
Figure 2- 10 Schematic epi-layer structure of GaAs/AlGaAs based UTC-PD.....	38
Figure 2- 11 A schematic diagram of UTC-PD while electrical holes relaxed by anode.....	38
Figure 2- 12 A schematic band diagram of UTC-PD while incident light of wavelength 800nm.....	39
Figure 2- 13 A schematic diagram of UTC-PD design .....	39
Figure 2- 14 Top-view of fabricated photonic-transmitter.....	43
Figure 2- 15 Top-view and cross-sectional view of the demonstrated sub-THz PT.	45
Figure 2- 16 Conceptual band diagrams of the demonstrated .....	45

### Chapter 3

Figure 3- 1 A schematic diagram for pulsed THz generation by PC antenna.....	57
Figure 3- 2 The simulated curves of two wave with slightly different frequencies. .....	61

Figure 3- 3 Schematic diagram of the PC antenna .....	64
Figure 3- 4 The measurement of carrier life time with both materials .....	65
Figure 3- 5 I-V Curve of GaAs:O and LTG-GaAs .....	66
Figure 3- 6 Current density v.s. Electrical field of LTG-GaAs and GaAs:O .....	66
Figure 3- 7 I-V curve of GaAs:O antennas and LT-GaAs antennas under pulse excitation.....	67
Figure 3- 8 I-V curve of GaAs:O antennas and LT-GaAs antenna under CW laser pumping .....	68

#### **Chapter 4**

Figure 4- 1 Schematic diagram of a bolometer and its structure drawing .....	76
Figure 4- 2 Schematic of experiment setup for measure the electric characteristics of PC antenna.....	78
Figure 4- 3 Schematic of a Martin-Puplett-type Fourier Transform Infrared Spectrometer (FTIR) system.....	80
Figure 4- 4 The reflectivity of the electric field dependent with frequency under (a) parallel and (b) perpendicular component. ....	81
Figure 4- 5 Terahertz Time-Domain Spectroscopy .....	82
Figure 4- 6 A picture of measured photonic transmitter in a TDS system.....	83

#### **Chapter 5**

Figure 5- 1(a) Photocurrent-bias (b)THz power-bias curve of GaAs:O and LT-GaAs antenna with the same antenna structure.....	86
Figure 5- 2 THz time domain waveform of (a) GaAs:O and (b) LT-GaAs at constant pump power 30mW .....	87

Figure 5- 3 THz spectrum of (a) GaAs:O and (b) LT-GaAs at constant pump power 30mW.....	88
Figure 5- 4 (a) Time domain waveform (b) Spectrum for both materials .....	89
Figure 5- 5 (a) The amplitude-pump power curve at bias voltage 80V (b) The THz power-electric field curve at 30mW.....	90
Figure 5- 6 (a) Photocurrent-bias voltage curve and (b) THz power-bias voltage curve of GaAs:O and LT-GaAs fabricated with the same dipole antenna .....	91
Figure 5- 7 (a) Photocurrent-bias voltage curve of both materials and (b) photocurrent ratio of GaAs:O divide to LT-GaAs.....	92
Figure 5- 8 (a) Different dosage density of GaAs:N and LT-GaAs (b) Different dosage density of GaAs:N and LT-GaAs[48] .....	93
Figure 5- 9 photocurrent-electric field curve and THz power-DC photocurrent curve for GaAs:O and LT-GaAs DC .....	93
Figure 5- 10 CW THz power-optical pump power for both materials.....	94
Figure 5- 11 (a) Photocurrent-electric field curve and (b) THz power-electric field curve.....	95
Figure 5- 12 THz spectrum of both materials measured by CW heterodyne system .....	96
Figure 5- 13 The Fourier-transformed spectra of our photonic-transmitters with different active lengths, 23 $\mu$ m (a) and 60 $\mu$ m (b).....	98
Figure 5- 14 The measured sub-THz intensity vs. optical pumping power under different reverse bias voltages .....	99
Figure 5- 15 The measured sub-THz intensity vs. reverse bias voltages under different optical pumping power for our photonic-transmitters with a	



23 $\mu$ m active length.....	100
Figure 5- 16 The bias dependent measured sub-THz power of (a) UTC-PT, (b) STR-PT, and (c) LTG-GaAs based PC under different optical pulse energy excitation. (d) shows the top-view of PC dipole antenna .....	102
Figure 5- 17 The power dependent measured sub-THz power of (a) UTC-PT and (b) STR-PT under different reverse bias voltage.....	104
Figure 5- 18 Bias-dependent sub-THz power of (a) UTC-PT and (b) STR-PT with a longer active length of 60 $\mu$ m under different injected optical pulse energy.....	106
Figure 5- 19 The radiated waveform of sub-THz pulses for UTC-PT (a) and STR-PT (b).....	107
Figure 5- 20 The normalized power spectrum of (a) UTC-PT, STR-PT and (b) LTG-GaAs based PC antenna. The inset shows the measured waveform of PC antenna.....	108
Figure 5- 21 Bias dependent waveforms of the radiated sub-THz pulses for (a) UTC-PT and (b) the normalized and enlarged main peak. The inset shows the normalized peak values versus reverse bias.....	110
Figure 5- 22 Bias dependent waveforms of the radiated sub-THz pulses for (a) STR-PT (b) and the normalized and enlarged main peak. The inset shows the normalized peak values versus reverse bias.....	110

## Chapter 6

Figure 6- 1 Schematic diagram of spiral antenna on LTG-GaAs PC antenna based TDS system for Sub-THz communication link .....	118
Figure 6- 2 Frequency response of spiral antenna based communication link	

system .....	118
Figure 6- 3 The input image signal from CCD and received signal after current amplifier .....	119
Figure 6- 4 Schematic diagram of sub-THz communication link system by using Photonic transmitter and W-band power detector .....	119
Figure 6- 5 Frequency response of communication link based on photonic transmitter and W-band power detector .....	120
Figure 6- 6 The schematic experiment setup of TDS based transmission system.	121
Figure 6- 7 Signal coding : (a) OOK coding (b) Manchester coding, and (c) differentially detected Manchester coding .....	122
Figure 6- 8 Signal coding : (a) OOK coding (b) Manchester coding, (c) half-bit delayed and (d) differentially detected Manchester coding .....	122
Figure 6- 9 Measured power spectrum and the inset shows the electrical field ....	122
Figure 6- 10 Bit error rate (BER) versus data rate of OOK transmission in our system .....	123
Figure 6- 11 Measured bit error rate (BER) versus different bias voltage applied on emitter by using Manchester and OOK coding respectively. ....	123
Figure 6- 12 Top view of NBUTC-PT. ....	124
Figure 6- 13 A schematic setup of impulse communication link with optical modulation. ....	125
Figure 6- 14 A schematic setup of impulse communication link with bias modulation. ....	125
Figure 6- 15 Picture of receiver end .....	126
Figure 6- 16 Power spectrum measured at different position. ....	127
Figure 6- 17 BER versus distance under different modulation speed.....	127

# List of Tables Pages

Table 1 Specification of the bolometer used in our measurement .....	76
Table 2 The list of measurement results of UTC-PT and STR-PT .....	109
Table 3 Detail epitaxial structure of UTC-PD .....	135
Table 4 Detail epitaxial structure of STR-PD .....	136

# Chapter 1 Introduction

## 1-1 THz Gap

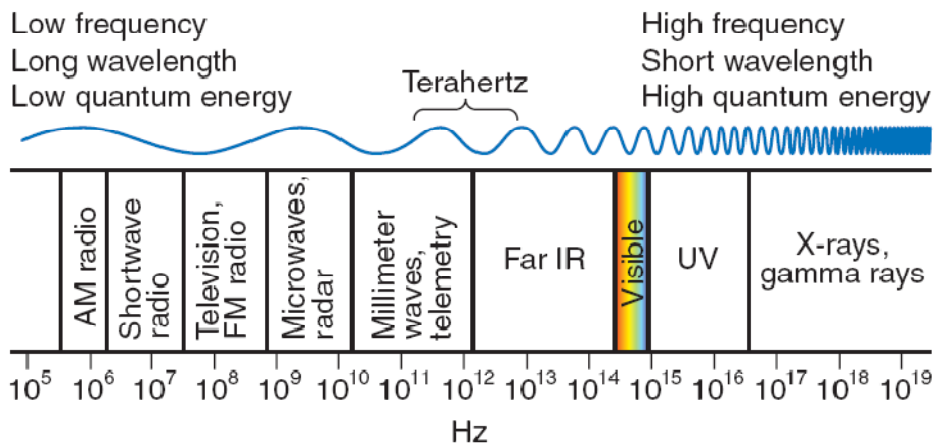


Figure 1- 1 Electromagnetic wave spectrum

Terahertz (THz) wave (or Tray) and sub-THz is the electromagnetic wave located between microwaves and infrared light (Fig. 1.1[2]). The THz gap ranges from 0.1 THz to 10 THz, where 1 THz equals 33 wave numbers or 300  $\mu\text{m}$  or 4mev. Lower frequencies, e.g., RFs for AM and FM radio as well as microwaves, are based on electric generation controlled by the classical transport of electrons. Radio reception and cellular telephony indoors are allowed for most dielectric materials that are transparent at these frequencies.

Higher frequencies in the spectrum, e.g., IR radiation, visible light and UV, can be generated by quantum transitions. Such frequencies can generate extremely high intensities using lasers and often propagate in a free space based on the laws of geometrical optics. Located between these two regions is the THz regime, which represents the transition between the electric and photonic sources. Thus,

electromagnetic radiation in the THz range can be generated both ways. Until recently, the THz region of the electromagnetic spectrum was almost always inaccessible because of inefficient sources and detectors in this gap. This region has attracted considerable attention owing its increasingly diverse array of applications, ranging from communications, security screening to medicine and nondestructive evaluation. [1]

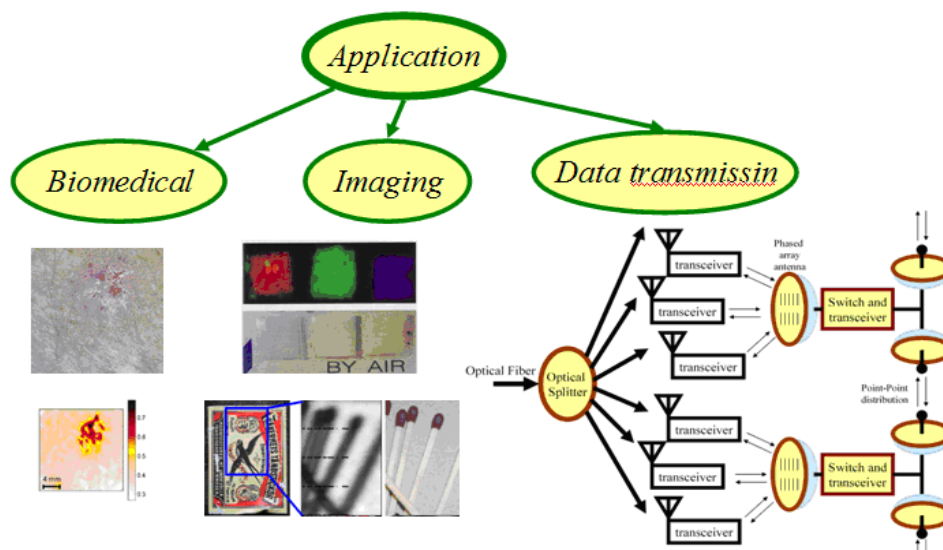


Figure 1- 2 Some examples of THz application

In the 1960s, astrophysics research sparked interest in developing THz detectors because the rotational spectra of some gases of astrophysical and environmental interest fall within this range. In 1975, a pioneering work on picoseconds(ps) photoconductivity in silicon [3,4] led to the development of photoconductive and electro optic methods [5], capable of generating and detecting radiation in the THz frequency range.

An important property of Terahertz is that it does not harm biological cells or the human body owing to its low photon energy. Terahertz is roughly one million

times weaker than an X-ray photon, subsequently not incurring damage often associated with ionizing radiation such as X-ray. This property makes the T-ray diagnostic procedure an interesting complement to X-ray radiography. Additionally, each material has its own intrinsic absorption and reflection characteristics in the THz region (referred to as THz finger print), making it useful for identifying their characteristics while it is difficult to distinguish from appearance. Important detective applications are thus possible when combining with another feature of terahertz wave, i.e. it is highly transparent to most non-metallic and non-polar media but highly reflected by metal and absorbed by liquid (like water) or vapor. Such behavior can be exploited to see through packaging and identify metal inside, without damaging the package nondestructive detection. Therefore, terahertz wave has tremendous applications in biomedical science, e.g., skin cancer detection [6], DNA analyzers [7], THz imaging [8], security screening in airports [9], mail inspection [10]) and semiconductor manufacturing [11]. In addition to these applications, several communications applications are available where THz waves will provide new capabilities.

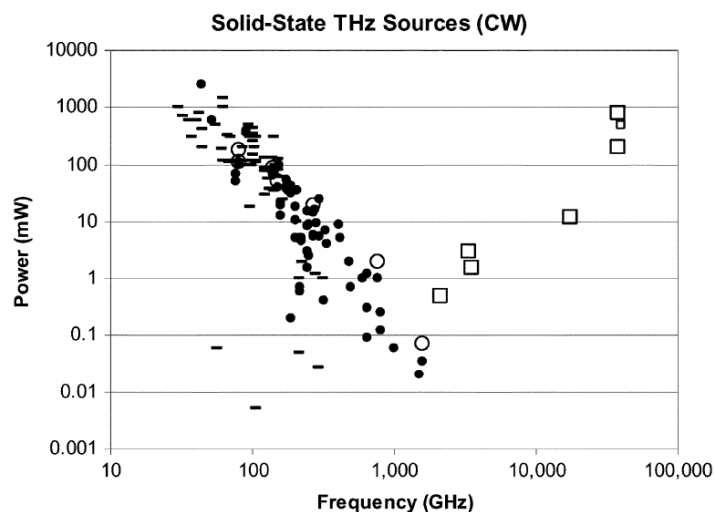


Figure 1- 3 Terahertz gap with respect to source technology.

(Quantum cascade lasers (□) are progressing downward from higher frequencies, while electronic technology is progressing upward. Frequency multipliers (●) dominate other electronic devices (—) above about 150 GHz. )

Obviously, terahertz technology has many current and future applications, likely playing a larger societal role as other developed bands have such as microwave and infrared bands. This has not yet occurred largely owing to the complexity in achieving a mature technology level in this spectral region. Below 100 GHz, it is common for electronic devices such as amplifiers and oscillators. Above 10 THz, solid-state lasers, light-emitting diodes and optical detectors are also available. Nevertheless, in between, neither of these technologies are particularly practical, resulting in a technology gap in terms of both sources and detectors. Figure 1.3 shows a graph of output power versus frequency for Terahertz gap with respect to source technology. [12] Other CW technologies, including tube devices, e.g., backward wave oscillators, can yield much more power.

## **1-2 THz Impulse Radio Communication**

### **THz and Sub THz communication**

THz and Sub THz communication can refer to either effective data rates up to 100 GHz ~ 1THz bit/s normally on an optical carrier) or communication with a sub-THz or THz carrier wave, which is the focus on this study. Although greater bandwidths can be obtained at optical wavelengths with point-to-point optical communications, communications at THz frequencies are extremely attractive for several reasons. According to the U.S. Frequency Allocation chart in Fig. 2,

frequencies (exceeding OR above) 300 GHz are unallocated by the Federal Communications Commission. [1] THz communication is in the infant stage of development, with the first data transmission in this frequency range reported recently. As for the frequency around sub-THz (>100GHz), much space is to be developed. Recently, because some pass bands incur a reasonable loss (e.g., 65~160GHz and 220~300GHz), the millimeter wave (MMW) band above 60GHz (V-band) or 100GHz (W-band) has received increasing attention as a carrier frequency for advanced communication system.

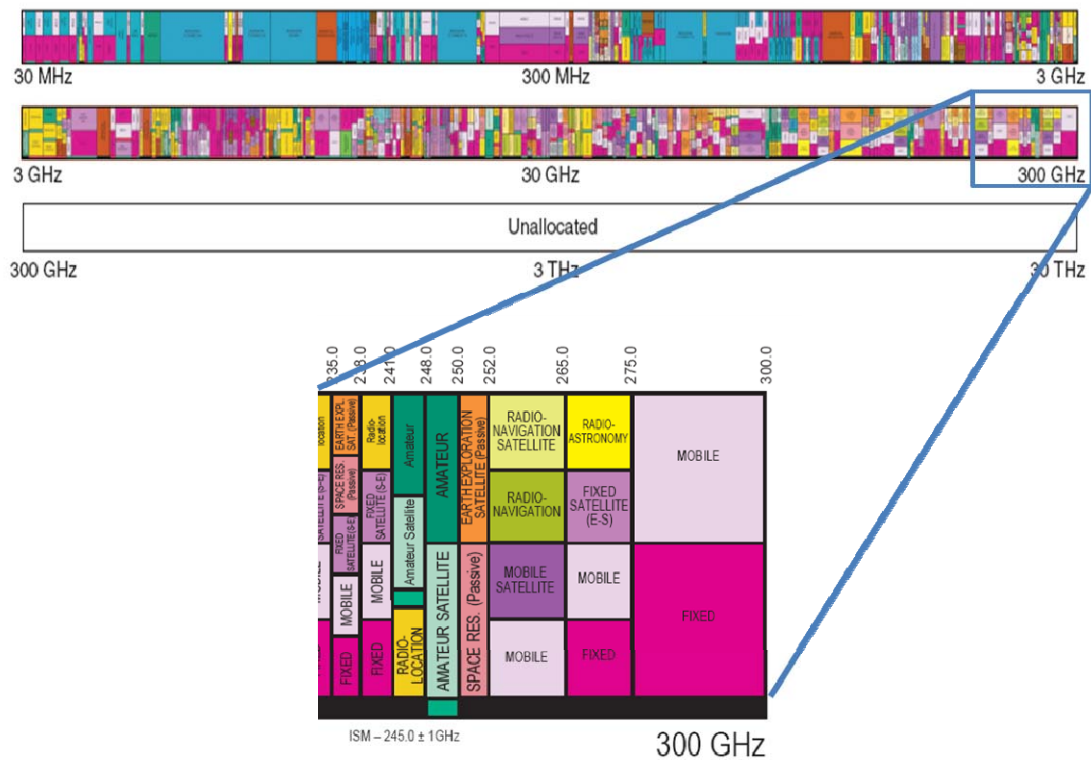


Figure 1- 4 The regulated spectrum as designated by the U.S. Federal Communications Commission

(The regulated spectrum as designated by the U.S. Federal Communications Commission and the THz region, which is completely unallocated at the time of writing. Source:

<http://www.ntia.doc.gov/osmhome/allochrt.pdf>.) The inset shows the enlarged figure of



regulated spectrum around 300GHz.)

### Wireless communication and Radio-over –fiber

Figure 1.5 illustrates the progress of transmission bits rate for various communication technologies, including wire line and wireless communication. Obviously, wireless communications is advancing to where the focus is shifting from voice to multimedia services. The underlying technology does not appeal to consumers; individuals merely require reliable and cost effective communication systems, capable of supporting all media without time or location constraints. Additionall, an increasing number of new wireless subscribers demand more capacity despite the fact that the radio spectrum is limited. Wideband radio links increasingly communication systems.

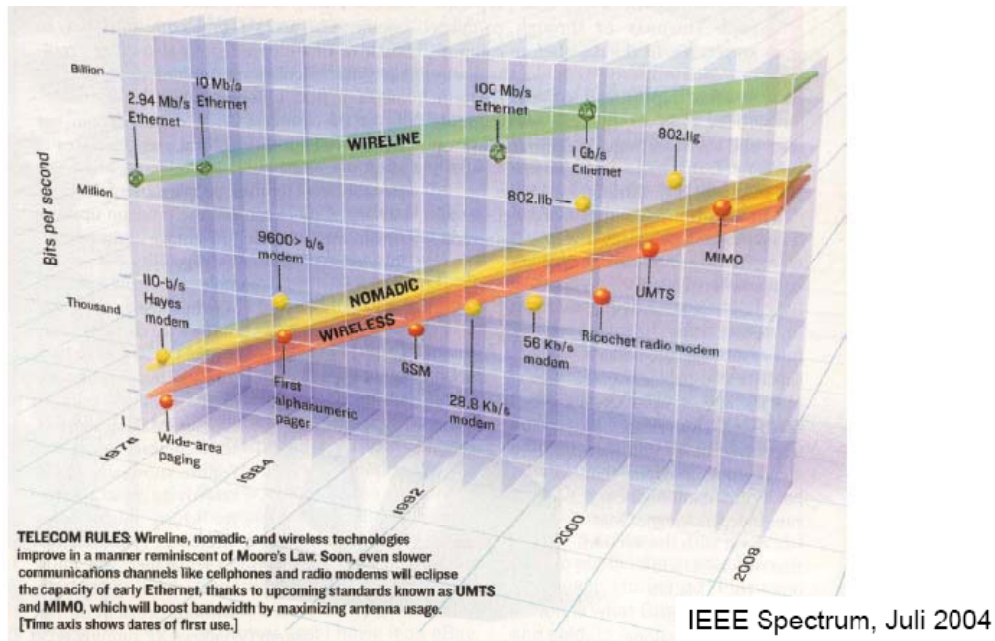


Figure 1- 5 Progress of transmission bits rate for different communication technology

The high capacity of optical networks should be integrated with the flexibility of radio networks to satisfy this increasing demand. Such a requirement can be satisfied

with micro/pico cellular architectures for the above mentioned wideband demands, especially by using fiber based wireless access schemes such as radio-over-fiber (RoF). Such a concept can easily support high speed multimedia, as shown in Fig. 1-6 . RoF communication systems have received considerable interest recently owing to their promising role in satisfying the significantly increasing demand for data capacity [13]. In this system, the high speed data signal is transmitted by an optical fiber for long-haul communication and, then, radiated to a free space for metro environment wireless access by converting the optical signal into an electrical radio signal. A vision from NTT is also proposed in the Fig. 1-7, in which data (including movies or music) can be downloaded from an access point to our portable devices wirelessly and at a high speed rate of up to 10 Gbits/s. Nevertheless, the low frequency band contains too much congestion to develop a >10Gb/s Ethernet, necessitating that the data signal is carried via higher frequency bands.

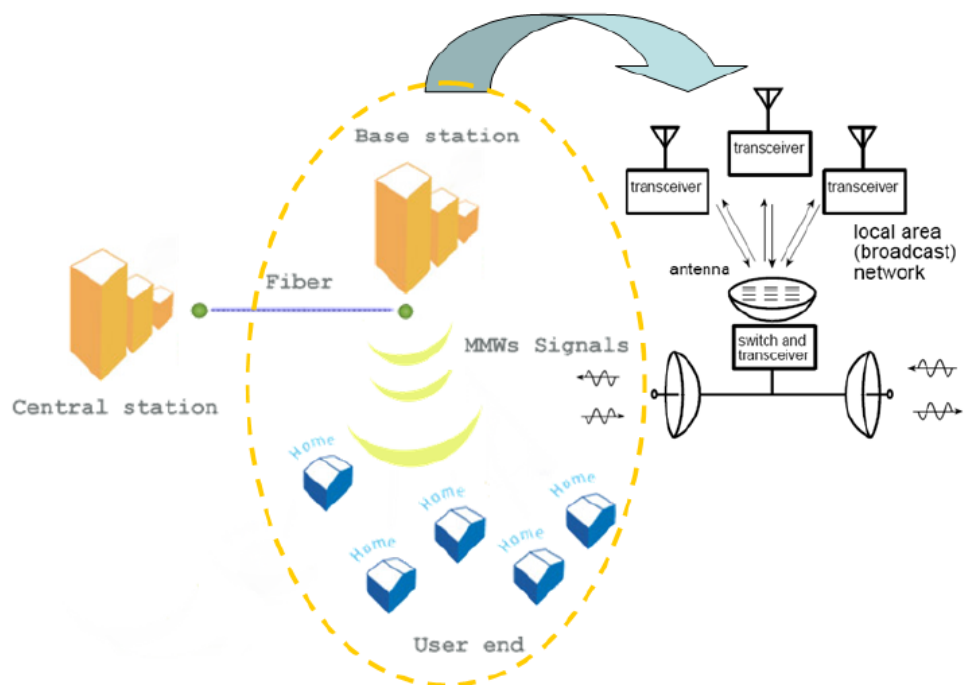


Figure 1- 6 Diagram of radio-over-fiber communication system

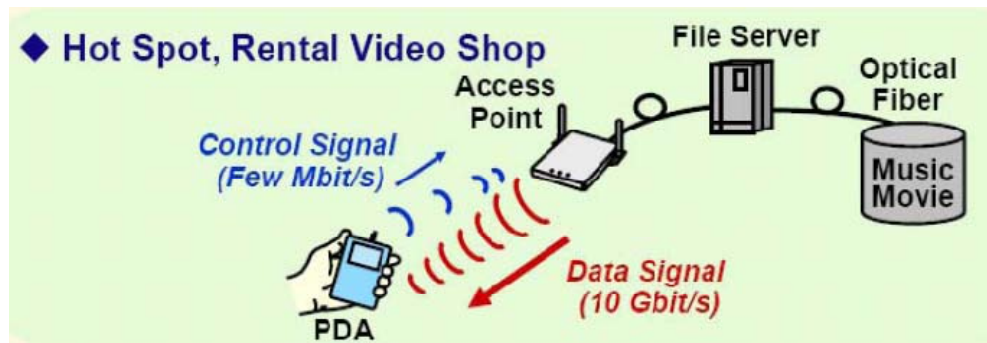


Figure 1- 7 A vision proposed from NTT to transmitted data >10Gbit/s wireless

### Impulse radio technology

As mentioned above, the transmission rate in local area networks (LANs) and personal area networks (PANs) must be (increased OR improved) owing to the rapidly increasing data volume handled by (household and office users OR individual users in both household and offices). In wired communications, 10-Gb/s Ethernet (10GbE) has already been standardized and is commercially available (Fig. 1-5). However, (it : what is it?) is only 54 Mb/s for the maximum transmission rate of wireless LANs, i.e. two orders of magnitude slower than that of 10GbE. Consequently, impulse radio (IR) technology has attracted considerable interest owing to its potential to fill this gap [14], [15]. Moreover, IR has other advantages similar to those of ultra wide band communication (UWB) such as secrecy and low power consumption. Therefore, our research of photonic schemes has attempted to derive solutions in order to enhance the transmission performance of IR systems [16], [17]. This is because photonic approaches perform better than electronic ones in terms of generating and detecting short pulse signals at a high repetition frequency in the above fiber-optic transmission systems [18]. Funk et al. demonstrated the feasibility of a photoconductive correlation switch for a receiver in an IR system and reduced interference rejection at a bit rate of 38 Mb/s[17].

### Disadvantages of communications

Communications at sub-THz frequencies is limited by strong absorption caused by water vapor through the atmosphere, as shown in Figs. 1-8 and 1-9. Another limitation is the low efficiency and relatively low power available from available sources. For a 1-mW source and a detection sensitivity of 1 pW, the working dynamic range is generally 60 dB, allowing communications at a range of 500 m in an atmospheric transmission window with an attenuation of <100 dB/km.[2]

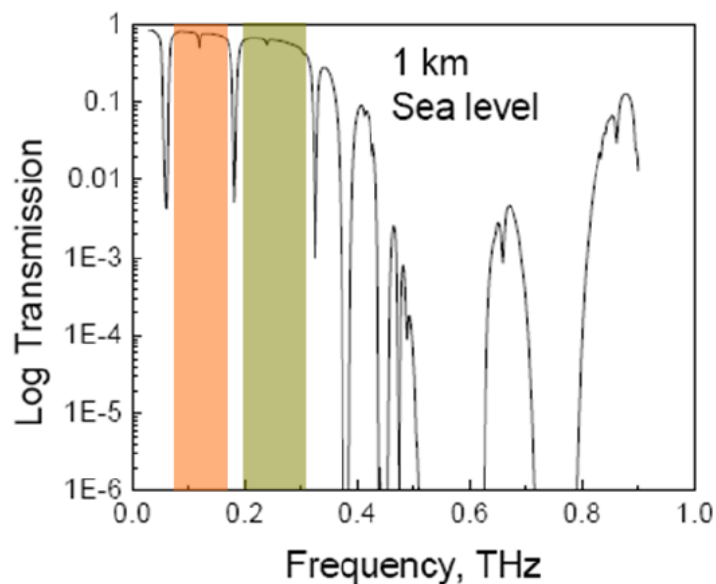


*Figure 1- 8 Transmission spectrums*

Regardless of the above limitations, this frequency range still has promising communications applications. For instance, atmospheric absorption does not inhibit satellite-to-satellite communications, except for paths grazing the earth atmosphere. Among the advantages of using THz technology is a larger bandwidth, thus yielding a transmission rate higher than that in microwave communications without (switching OR having to switch) to a different set of hardware components such as lasers for optical communications. Indoor wireless communications with THz may

also provide multiple data channels with gigabit per second or a larger capacity. The data bandwidth exceeds wireless protocols such as IEEE 802.11b, and the propagation distance, although limited, resembles line-of-sight IR.

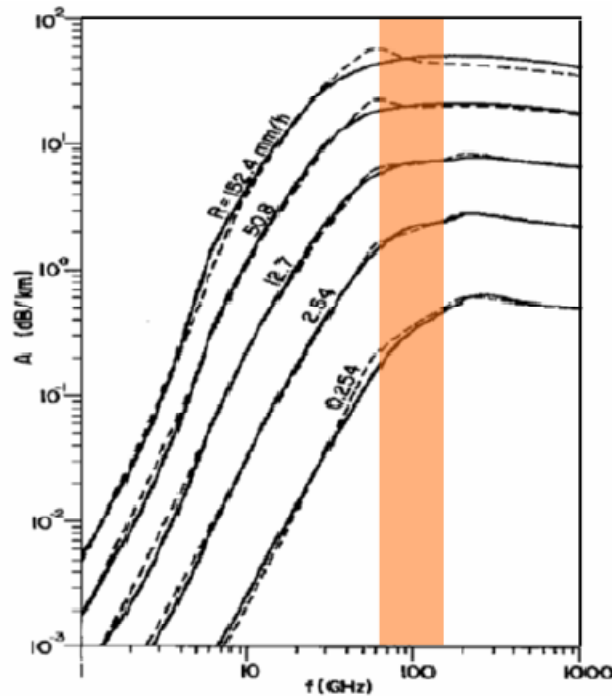


Figure 1- 9 Attenuation spectrums in rainy day

### 1-3 Generation of Sub-THz Pulses

As mentioned in the above section, IR technology can satisfy the demand for low transmit power, high bit rate wireless communications. However, RF impulses generated from pure electronic devices, which normally last one nanosecond or longer, limit the maximum bit rate in wireless communications. Shock wave nonlinear transmission line (belonging to NLTL) [19] can be used to generate THz by using short electrical pulses, which often incur an enormous propagation loss in the free space. The pulse signal can be distributed through a low loss optical fiber. An optical

pulse triggered photoconductive (PC) antenna or photonic transmitter (PT) is a promising alternative to radiate the converted electrical signal to the user end. By using photonic technologies such as an optical pulse triggered photoconductive antenna, short pulses lasting only a few picoseconds can be generated and received [20,21]. Based on the maturity of high performing optical pulse sources with wavelengths around 800nm, e.g., solid-state Ti:sapphire mode-locked lasers (Fig. 1-10 and 1-11), low-temperature-grown-GaAs (LTG-GaAs) based photodetectors are regarded as a promising choice for serving as a photonic transmitter to generate continuous wave (CW) THz signal or THz pulses at such an optical wavelength regime [19,22].

A Ti:Sapphire laser provides short pulse (several fs) width and high peak power with repetition rate around 100MHz and can be operated easily under room temperature. Furthermore, other compact commercial products with a higher repetition rate have been proposed (Fig. 1-11), which has the potential for use in constructing a compact system with a higher data rate transmission. Communication links on the sub-THz signal are also demonstrated through either a modulating photoconductive antenna or photonic transmitter [23,24].

This study discusses two photonic transmitters, PD based photonic transmitters (PTs) and LTG-GaAs or ion-implanted materials based photoconductive (PC) antennas. Both devices can generate a short transient current and then radiate sub-THz from integrated antennas while the transient current oscillates in the antennas. PD based PTs are integrated into the design of printed planar antenna with high speed photo diodes, as introduced in the next section. The next section also introduces several promising PDs with a high speed and high output power combined with different designs of antennas. As for the photoconductive antenna, an appropriate

material for photoconductive antennas is discussed. Moreover, the emission properties of LT-GaAs PC antennas are compared with those of GaAs:O substrate to study high power THz generation by using PC antennas.



*Figure 1- 10 Commercial Ti: Sapphire mode locked laser*



*Figure 1- 11 Commercial compact Ti: Sapphire mode locked laser*

## 1-4 Photodiode Based Photonic Transmitters

To alleviate the limitations of all-electronic local oscillators (LOs), a photonic LO (PLO) capable of operating up to (sub-) THz frequencies has received increasing interest. [25] Generally, in a PLO, a (sub-) THz signal is generated by square-law detection of a highly stable phase-locked optical heterodyne signal that uses an ultrafast photodiode (PD). Given its dependence on the beat-frequency difference between the two optical carriers of the heterodyne signal, the frequency of the generated (sub) THz signal can be easily tuned over an ultra wide range by varying the frequency of an optical carrier. In this study, a mode locked pulse laser, which could be viewed as a combination of many frequencies, is used to excite our PLO. A PLO consists mainly of a highly stable optical source and a high-speed PD in the remote photonic (sub) THz transmitter (Fig. 1-12). [25] Figure 1-13 also shows an example of a photonic transmitter consisting of a TWPD monolithically integrated with a planar full-wave single slot antenna. Nevertheless, in contrast with typical GaAs based p-i-n photodiodes (PDs), the decreasing trend of external efficiency for the LTG-GaAs-based PDs is inevitable owing to the existence of recombination centers in the photo-absorption layer [26].

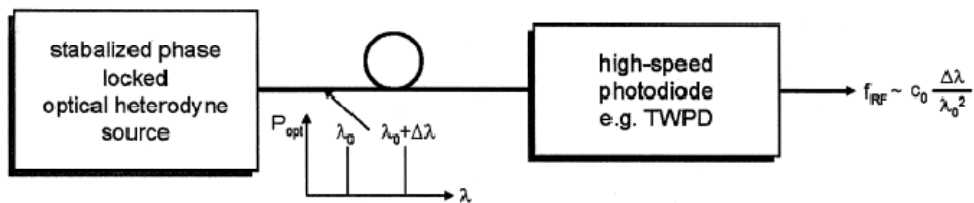
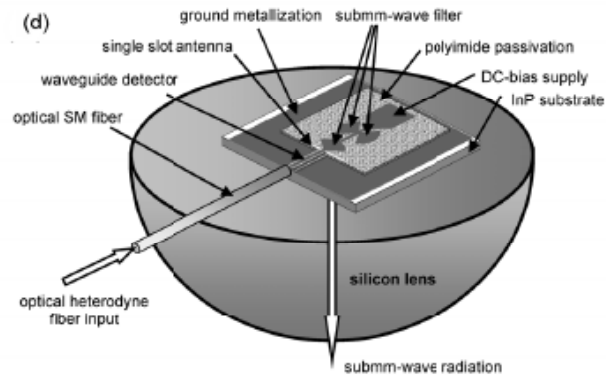


Figure 1- 12 Schematic of optical heterodyne signal generation in an photonic local oscillator (PLO).





*Figure 1- 13 Schematic of a photonic transmitter consisting of a TWPD monolithically integrated with a planar full-wave single slot antenna*

Another attractive alternative for photonic transmitter applications is InGaAs-InP based UTC-PD structures [27]. However, in the case of InP based UTC-PDs under  $0.8 \mu\text{m}$  wavelength excitation, the incident photons produce sufficient photon energy to induce absorption in the entire epi-layer structure. Therefore, our previous study developed a high-speed GaAs/AlGaAs based UTC-PD [28], which consists of a GaAs based p-type photo-absorption layer and an  $\text{Al}_{0.15}\text{Ga}_{0.85}\text{As}$  based collector layer to avert undesired photo-absorption that occurs in the collector layer under  $800\text{nm}$  wavelength excitation. This study analyzes the power and bias dependent behaviors of a novel sub-THz photonic-transmitter (PT), which is composed of our edge-coupled GaAs/AlGaAs based UTC-PD [28] and a micromachined frequency-independent circular disk monopole antenna [29], capable of eliminating the additional integration of silicon lens with a photonic transmitter [26].

## **1-5 Low Temperature Grown Based GaAs (LTG-GaAs) or Ion-implanted Materials Based PC Antennas**

Compared with above photonic transmitters, PC antennas provide another alternative means of generating radiation with a higher frequency (up to 1~2THz). The radiation frequency bandwidth depends mainly on PC material properties. The fact that PC devices can generate both broadband THz wave (photocurrent acceleration) and a narrow band THz wave (photomixing) explains why the photoconductive method has become a conventional approach for THz wave generation used in laboratories. The photoconductive approach uses high-speed photoconductors as transient current sources for radiating antennas. Notable examples include LTG GaAs [30], ErAs:GaAs [31] for 800nm light, and LTG InGaAs, InGaAs:Br<sup>+</sup> [32] for 1550nm light.

Among the many (attractive OR important) properties of LTG-GaAs include a high dark resistivity ( $>10^6 \Omega\text{cm}$  [33]), short carrier lifetime(0.25 ps[31, 35]), high carrier mobility ( $200 \mu\text{m}/\text{V}\cdot\text{s}$  [36]), and high breakdown voltage( $>5\times 10^5 \text{ V}/\text{cm}$ [37]). Consequently, LTG GaAs is the commonly used material for 800nm pumping PC devices. Nevertheless, these excellent characteristics are difficult to (replicate OR reproduce). Such difficulty is owing to that the quality of LTG GaAs depends not only on the preparation temperature but also on the post thermal annealing conditions. Consequently, some materials grown by ion implantation method have the potential to be a reliable complement of LTG GaAs because controlling the ion dosage and implant energy precisely can overcome the reproducibility limitation of LTG GaAs.

As the energy level formed by oxygen ions in GaAs (approaches OR is close to) the Fermi level, the O<sup>+</sup> implanted GaAs become almost electrically neutral, thus producing a relatively higher resistance. This study also attempts to elucidate this oxygen ion implanted GaAs material and its THz wave generation properties under both pulsed and CW modes. Its performance is also compared with that of LTG GaAs materials, such as comparing the performance of THz generation with that of LTG GaAs, the saturation behavior and its materials, the maximum output power of THz wave from GaAs:O based PC devices, as well as the screening behavior under CW background illumination. Other interesting research areas for GaAs:O based PC devices include optimization of the generation performance, system compacting) and unique applications.

## **1-6 Organization of Dissertation**

This dissertation is organized as follows:

Chapter 2 introduces high-power and high-speed photodiodes (UTC-PD) and separated-transport-recombination photodiode (STR-PD). By inserting a LTG-GaAs layer that has an extremely long carrier time to serve as a recombination center, STR-PD performs better in terms of speed and power than a control PD that has a pure intrinsic photo absorption layer. Next, the feasibility of a photonic structure is demonstrated, which consists of STR-PD and a micromachined co-planar-waveguide (CPW) fed slots antenna with resonant frequency 500GHz. Next, two high-power photodiodes (UTC-PD and STR-PD) are integrated with the same planar antenna (circular disk monopole antenna with a center frequency around 150GHz) to serve as photonic transmitters. This chapter describes the design principles and device

structure in detail.

Chapter 3 introduces several photoconductive antennas consisting of different materials and printed antennas. The basic theories of THz radiation generated from photoconductive (PC) antenna are introduced first. An attempt is then made to identify the proper material type of printed antennas. Next, except for the conventional material LTG-GaAs, the ion implantation method of oxygen and its parameters selection are introduced. Finally, to optimize the preparation conditions, additional properties of important materials such as the carrier concentration, resistivity, carrier mobility and the carrier lifetime are tested and measured. Exactly how LT-GaAs and GaAs:O emitters affect THz radiation of PC antennas is elucidated by comparing their electrical characteristics.

Chapter 4 describes the experimental setup and measurement method to identify radiation properties of our emitters in sub-THz and THz. The radiated absolute power is (determined OR measured) using a liquid helium-cooled Si bolometer which has been calibrated carefully using a blackbody source. Chapter 4 also introduces a horn antenna owing to its feasibility for a lower band detection (W band, around 100GHz) and higher modulation speed. As for the electrical field measurements, two systems of FTIR and PC sampling are used. Based on use of fast Fourier transforms, the radiation bandwidth of devices is estimated to identify the reliability of our designed devices.

Chapter 5 summarizes in detail all measurement results for both PCs and photonic transmitters. Our discussion of PCs focuses mainly on comparing the properties of PCs: based LT-GaAs and GaAs:O. Preliminary results indicate that GaAs:O is at least as good as LT-GaAs in (generating OR producing OR making) high power THz emitters under both pulse and CW excitation. However, when LT-GaAs is

used as the active layer, STR-PT combined with slot antenna can radiate a high output power at a frequency around 0.5THz. Additionally, a further comparison is made of THz emitters made by two high-power photodiodes (UTC-PD and STR-PD) by summarizing the measurement results of both PDs combined with the same antenna type. Moreover, the properties of photonic transmitters are compared with those of PC antennas.

Chapter 6 demonstrates the possibility of wideband communication applications by using our sub-THz emitters. First, we improve communication quality of the LTG-GaAs PC antennas based TDS system by using Manchester coding. Next, a wideband carrier (W band, 75~110GHz) is generated by using a fiber mode-locked laser as system optical source and determining its maximum data transmission rate.

Conclusions are finally drawn in Chapter 7, along with recommendations for future research.

## Reference

- [1] M. Tonouci, "Cutting-edge terahertz technology," *Nat. Photonics*, vol 1, pp.97-105, Feb., 2007.
- [2] Michael J. Fitch and Robert Osiander, "Terahertz Waves for Communications and Sensing" *Johns Hopkins Apl Technical Digest*, Vol. 25, 4, 2004.
- [3] Auston, D. H., "Picosecond Optoelectronic Switching and Gating in Silicon," *Appl. Phys. Lett.* 26, 101–103,1975.
- [4] LeFur, P., and Auston, D. H., "A Kilovolt Picosecond Optoelectronic Switch and Pockels Cell," *Appl. Phys. Lett.* 28, 21–33, 1976.
- [5] Valdmani, J. A., Mourou, G., and Gabel, C. W., "Picosecond Electrooptic Sampling System," *Appl. Phys. Lett.* 41, 211–212 , 1982.
- [6] E. Pickwell and V. P. Wallace, "Biomedical applications of terahertz technology," *Journal of Physics D-Applied Physics*, vol. 39, pp. R301-R310, Sep 7 2006.
- [7] M. Brucherseifer, M. Nagel, P. H. Bolivar, H. Kurz, A. Bosserhoff, and R. Buttner, "Label-free probing of the binding state of DNA by time-domain terahertz sensing," *Appl. Phys. Lett.*, vol. 77, pp. 4049-4051, Dec 11 2000.
- [8] X. C. Zhang, "Terahertz wave imaging: horizons and hurdles," *Physics in Medicine and Biology*, vol. 47, pp. 3667-3677, Nov 7 2002.
- [9] J. W. Shockley; W. T. Read, "Statistics of the Recombinations of Holes and Electrons," *Physical Review* pp. 835 - 842, 1952.
- [10] A. W. M. Lee and Q. Hu, "Real-time, continuous-wave terahertz imaging by use of a microbolometer focal-plane array," *Optics Letters*, vol. 30, pp. 2563-2565, Oct 1 2005.

- [11] D. Grischkowsky, S. Keiding, M. Vanexter, and C. Fattinger, "Far-Infrared Time-Domain Spectroscopy with Terahertz Beams of Dielectrics and Semiconductors," *Journal of the Optical Society of America B-Optical Physics*, vol. 7, pp. 2006-2015, Oct 1990.
- [12] Crowe, T. W., Bishop, W. L., Perterfeld, D. W., Hesler, J. L. & Weikle, R. M. Opening the terahertz window with integrated diode circuits. *IEEE J. Solid-State Circuits* 40, 2104–2110 (2005).
- [13] A. Hirata, T. Kosugi, H. Takahashi, R. Yamaguchi, F. Nakajima, T. Furuta, H. Ito, H. Sugahara, Y. Sato, and T. Nagatsuma, "120-GHz-Band Millimeter-Wave Photonic Wireless Link for 10-Gb/s Data Transmission," *IEEE Trans. Microwave Theory Tech.*, vol. 54, pp. 1937-1944, May. 2006.
- [14] L. Larson, D. Laney, and J. Jamp, "An Overview of Hardware Requirements for UWB Systems: Interference Issues and Transceiver Design Implications," in *Tech. Dig. MILCOM2003*, Oct. 2003, pp. 863-867.
- [15] S. Iida, K. Tanaka, H. Suzuki, N. Yoshikawa, N. Shoji, B. Griffiths, D. Mellor, F. Hayden, I. Butler, and J. Chatwin, "A 3.1 to 5 GHz CMOS DSSS UWB Transceiver for WPANs," in *Tech. Dig. ISSCC 2005*, Feb. 2005, pp. 214- 215.
- [16] E. E. Funk and C. H. Lee, "Free-Space Power Combining and Beam Steering of Ultra-Wideband Radiation Using an Array of Laser-Triggered Antennas," *IEEE Trans. Microwave Theory Tech.*, vol. 44, pp. 2039-2042, Nov.1996.
- [17] E. E. Funk, S. Ramsey, C. H. Lee, and J. Craven, "A Photoconductive Correlation Receiver for Wireless Digital Communications," in *Tech. Dig. MWP'98*, Oct. 1998, pp. 21-24.
- [18] K. Uchiyama and T. Morioka, "All-Optical Signal Processing for 160 Gbit/s/channel OTDM/ WDM Systems," in *Tech. Dig. OFC'01*, March 2001,

paper ThH2-1.

- [19] M. J. W. Rodwell, S. T. Allen, R. Y. Yu, M. G. Case, U. Bhattacharya, M. Reddy, E. Carman, M. Kamegawa, Y. Konishi, J. Pustl, R. Pullela, “Active and nonlinear wave propagation devices in ultrafast electronics and optoelectronics [and prolog]” Proceedings of the IEEE, vol. 82, pp. 1037-1059, Jul., 1994.
- [20] S. M. Duffy, S. Verghese, K. A. McIntosh, A. Jackson, A. C. Gossard, and S. Matsuura, “Accurate modeling of dual dipole and slot elements used with photomixers for coherent terahertz output power,” IEEE Trans. Microwave Theory Tech., vol. 49, pp. 1032-1038, June, 2001.
- [21] Yu-Tai Li, J.-W. Shi, Ci-Ling Pan, C.-H. Chiu, W.- S. Liu, N.-W. Chen, C.-K. Sun, and J.-I. Chyi, “Sub-THz photonic transmitters based on separated-transport-recombination photodiodes and a micromachined slot antenna,”
- [22] H. Ito, T. Furuta, F. Nakajima, K. Yoshino, T. Ishibashi, “Photonic Generation of Continuous THz Wave Using Uni-Traveling-Carrier Photodiode,” J. of Lightwave Technol., vol. 23, pp. 4016-4021, Dec., 2005.
- [23] Togo, H., Sah, P.-C.P., Shimizu, N., Nagatsuma, T. “Gigabit impulse radio link using photonic signal-generation techniques,” European Microwave Conference 2005, vol. 1, pp. 4-7, Oct., 2005.
- [24] T. -A. Liu, G. -R. Lin, Y.-C. Chang, C.-L. Pan, “Wireless audio and burst communication link with directly modulated THz photoconductive antenna,”
- [25] A. Stöhr, A. Malcoci, A. Sauerwald, I. C. Mayorga, R. Güsten, and D. S. Jäger, “Ultra-wide-band traveling-wave photodetectors for photonic local oscillators,” J. Lightw. Technol., vol. 21, no. 12, pp. 3062–3070, Dec. 2003.
- [26] Yu-Tai Li, J.-W. Shi, Ci-Ling Pan, C.-H. Chiu, W.- S. Liu, N.-W. Chen, C.-K. Sun,



- and J.-I. Chyi, "Sub-THz Photonic Transmitters Based on Separated-Transport-Recombination Photodiodes and a Micromachined Slot Antenna," *IEEE Photon. Technol. Lett.*, vol. 19, pp. 840-842, June, 2007.
- [27] H. Ito, T. Furuta, F. Nakajima, K. Yoshino, T. Ishibashi, "Photonic generation of continuous THz wave using uni-traveling-carrier photodiode," *J. of Lightwave Technol.*, vol. 23, pp. 4016-4021, Dec., 2005.
- [28] J.-W. Shi, Y.-T. Li, C.-L. Pan, M. L. Lin, Y. S. Wu, W. S. Liu, and J.-I. Chyi, "Bandwidth enhancement phenomenon of a high-speed GaAs-AlGaAs based unitraveling carrier photodiode with an optimally designed absorption layer at an 830nm wavelength" *Appl. Phys. Lett.*, vol. 89, pp.053512, 2006.
- [29] Y.-C. Liang and N.-W. Chen, "An ultra-broadband coplanar waveguide-fed circular monopole antenna," *EuCAP 2007*, Edinburgh, UK, Nov. 2007.
- [30] Y. Cai, I. Brener, J. Lopata, J. Wynn, L. Pfeiffer, and J. Federici, "Design and performance of singular electric field terahertz photoconducting antennas," *Applied Physics Letters*, vol. 71, pp. 2076-2078, Oct 13 1997.
- [31] J. E. Bjarnason, T. L. J. Chan, A. W. M. Lee, E. R. Brown, D. C. Driscoll, M. Hanson, A. C. Gossard, and R. E. Muller, "ErAs : GaAs photomixer with two-decade tunability and 12 mW peak output power," *Applied Physics Letters*, vol. 85, pp. 3983-3985, Nov 1 2004.
- [32] J. Mangeney, A. Merigault, N. Zerounian, P. Crozat, K. Blary, and J. F. Lampin, "Continuous wave terahertz generation up to 2 THz by photomixing on ion-irradiated In<sub>0.53</sub>Ga<sub>0.47</sub>As at 1.55 μm wavelengths," *Applied Physics Letters*, vol. 91, pp. -, Dec 10 2007.
- [33] P. Kordos, M. Marso, and M. Mikulics, "Performance optimization of GaAs-based photomixers as sources of THz radiation," *Applied Physics*

a-Materials Science & Processing, vol. 87, pp. 563-567, Jun 2007.

- [34] K. A. McIntosh, E. R. Brown, K. B. Nichols, O. B. McMahon, W. F. DiNatale, and T. M. Lyszczarz, "Terahertz photomixing with diode lasers in low-temperature-grown GaAs," *Applied Physics Letters*, vol. 67, pp. 3844-3846, Dec 25 1995.
- [35] E. R. Brown, "A photoconductive model for superior GaAs THz photomixers," *Applied Physics Letters*, vol. 75, pp. 769-771, Aug 9 1999.
- [36] E. R. Brown, F. W. Smith, and K. A. McIntosh, "Coherent Millimeter-Wave Generation by Heterodyne Conversion in Low-Temperature-Grown GaAs Photoconductors," *Journal of Applied Physics*, vol. 73, pp. 1480-1484, Feb 1 1993.
- [37] M. Y. Frankel, J. F. Whitaker, G. A. Mourou, F. W. Smith, and A. R. Calawa, "High-Voltage Picosecond Photoconductor Switch Based on Low-Temperature-Grown GaAs," *Ieee Transactions on Electron Devices*, vol. 37, pp. 2493-2498, Dec 1990.

# Chapter 2 THz Photonic Transmitters

## 2-1 Introduction

Because many applications in sub-THz or THz band need compact, convenient, broadband THz sources with high output power. Some proposed applications include sub-THz sources, Gunn diodes, resonant tunneling diodes [1,2], and quantum cascade THz lasers [3-5]. Currently, several related products like THz image systems, THz spectroscopy kits, etc are now commercially available. These systems usually constructed with Ti:sapphire mode-locked laser ( $\lambda=800\text{nm}$ ) and compact THz emitter modules. It's attractive to replace these modules by compact photonic-transmitters (PTs), which are composed of an antenna and a high speed and power photodiode (PD) [6-9]. The PTs have the advantages of simplicity, room-temperature operation, tunable THz wavelength, and easy integrability with other semiconductor devices.

In order to further improve the maximum transmission distance in a sub-terahertz (sub-THz) IR communication links [10-12], it is necessary to have a PD which can sustain its high-speed performance and deliver high output power under intense optical pulse excitation. There are two major strategies to meet this challenge [13]. One is to distribute and make uniform the photocurrents along edge-coupled PDs by improving the structure of optical and electrical waveguides, for example, the velocity matched distributed photodetector (VMDP) [14] and evanescent coupled photodiode (ECPD) [15,16]; the other strategy involves minimizing the space-charge screening (SCS) effect [13, 17] in the photo-absorption volume. Under intense optical power illumination, the photo-generated carriers will induce a strong space-charge field,

screen out the external applied electrical field, and seriously limit the output saturation power of the PD. By increasing the drift-velocity of photo-generated carriers, such as with the structure of a uni-traveling carrier PD, excellent high-speed and high-power performance has been demonstrated [18].

Under 1.55  $\mu\text{m}$  long wavelength excitation, an InP/InGaAs based UTC-PD based photonic-transmitter has been shown to generate a continuous wave (CW) output power at 1.04THz of as high as 2.3 W [18]. In the case of an InP based UTC-PD operated under 0.8  $\mu\text{m}$  wavelength excitation, the incident photon will have enough photon energy to induce the absorption process in the InP based collector layer. The presence of photo-generated holes in the collector layer will degrade the high-power performance of the UTC-PD. We overcome this problem with our demonstrated high-speed GaAs/AlGaAs based UTC-PD [19], which is composed of a GaAs based p-type photo-absorption layer and an  $\text{Al}_{0.15}\text{Ga}_{0.85}\text{As}$  based collector layer. Undesired photo-absorption under 800nm wavelength excitation is avoided with this device. We have also demonstrated a high-power photonic-transmitter that operates under 800nm optical short-pulse excitation [20].

It is also possible to minimize the SCS effect by decreasing the thickness of the depletion layer which has a direct effect on the carrier transit time, such as the structure of a partially depleted absorber photodiode [21]. However, PDs with thin depletion layers usually suffer from problems of low quantum efficiency and very limited RC bandwidth. In order to overcome the above-mentioned problems, we have demonstrated a p-i-n photodiode structure: the Separated-Transport-Recombination photodiode (STR-PD), which can greatly relieve the trade-off between output saturation power, quantum efficiency, and electrical bandwidth performance [22]. In the demonstrated GaAs based STR-PD, a

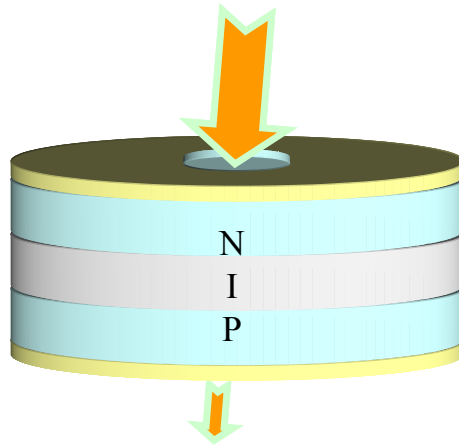
LTG-GaAs layer is adopted, which has an extremely short carrier lifetime (less than 1ps) [23], to serve as the recombination center in the active photo-absorption region. The STR-PD exhibits superior electrical bandwidth performance under a higher output current regime without seriously sacrificing responsivity compared to that of the control p-i-n PD (with a pure intrinsic GaAs based photo-absorption layer) [25]. In this study, the integration of the STR-PD with a narrow-band slot-antenna to produce an STR-PD based photonic transmitter will be described previously in section 2-5. After that, we integrate two different kinds of high-power photodiodes (UTC-PD and STR-PD) with the same type of planar antenna (circular disk monopole antenna) to serve as photonic transmitters. We also compare their dynamic performance using the same THz time-domain spectroscopic system. These two different devices exhibit distinct dynamic behaviors and very different mechanisms of saturation. Under high optical pulse energy excitation ( $\sim 480\text{pJ/pulse}$ ), the STR-PD based transmitter exhibits much a lower maximum average output photocurrent (1.2mA vs. 0.3mA) than that of the UTC-PD transmitter. The radiated electrical envelop-width ( $\sim 50\text{ps}$ ) and maximum peak-power ( $\sim 9\text{mW}$ ) of both devices are comparable. This indicates that although the DC responsivity of the recombination center in the STR-PD is degraded, the high-speed and output power performance of the device have been effectively improved and the DC component of the photocurrent eliminated. The smaller DC photocurrent implies that device-heating problems of STR-PD based transmitters during high-power operation will be decreased. The dynamic measurement results reveal that although the working principles for the high-power performance of the STR-PD and UTC-PD are totally different, both devices exhibit comparable and promising high-speed and high-power performance for applications in THz photonic transmitters.

## 2-2 Basic Theory

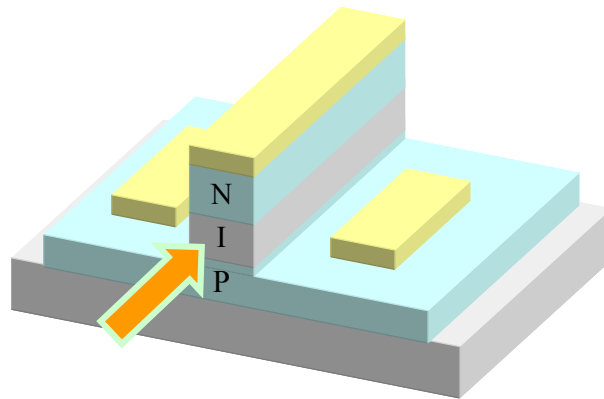
As implied in the name, photodiode is a device that transform optical signal to electrical signal. Thus, properties of bandwidth, transform efficiency and output saturated current are all aims of high speed and high efficiency PDs. [24] In order to achieve the above goals, not only geometrical structure but epi-layer structure is need to be designed well.

According to their geometry, structures of PDs could be classified into two types of vertically incidence (VPD) and edge coupled incidence (WGPD). [24] As for vertical incidence PDs, incident light can't be absorbed completely after passing through absorption layer once due to the fixed thickness, thus quantum efficiency decrease seriously. This phenomenon could be improved by adding a reflector at the bottom of devices to help the number of times of light reflection. However, it could limit RC bandwidth of devices seriously. In the other side, edged incident photodiodes are provided with higher quantum efficiency because incident light could be absorbed while propagate in the waveguide at the same time., which structure is adopted in our designed components.

The design of travelling wave (TWPD).[25][26] are adopted to solve the problems mentioned above. Such design could not only reduce the influence of mismatch between optical velocity and electrical velocity but achieve best bandwidth through design of co-plane electrode shape which match with external resistance. In addition to geometrical structure, material of epi-layer structure also limit frequency response, quantum efficiency and saturation current of devices.



(a)



(b)

*Figure 2- 1 (a) Vertically incident PD and (b) edge coupled incident PD*

After carrier generation from absorption area, the distribution and transmission of carriers influence frequency response. In some designed epi-layer structure, carrier life time influence frequency response seriously.

### **Principal of traveling wave photodiode and frequency limitation**

Traveling wave photodiode is a waveguide photodiode, which incident light inject into devices from edge side and the direction of light propagation and photo current is the same. The main limitation of bandwidth is caused by mismatch of optical and electrical velocity. [26] The best design is to match optical and electrical velocity of devices and to match external resistance with its electrode, which could

minimum reflection.

In the PIN ridge waveguide structure, the higher refraction index in the intrinsic layer could serve as transmission layer to guide light. It could be an absorption layer due to its lower band gap. Such kind of structure is like a microwave transmission line which light is absorbed while propagating in the waveguide. As a result, an effective circuit of transmission line is used to design our structure which combining stripe transmission line and planar electrode than increase operation speed of devices.

### **Travelling Wave Photodiode effective circuit**

In order to improve speed of devices, we have to design our devices by simplify devices structure as an effective circuit and then analysis them. A model with distributed current is used to explain speed limitation of devices. When light incident into our devices, carriers are generated in the inner absorption layer and accelerated by induced electrical field, which cause distributed photocurrent as shown in figure 2-2. According to theorem of transmission line, it will cause microwave signal parallel with light and collected in the output port.

As shown in figure 2-2, photo current is generated in the intrinsic layer while light is absorbed, which cause main capacitance of devices. Thus, value of capacitance is decided by thickness of waveguide and absorption layer directly. The equivalent circuit of active area of devices is shown in figure 2-3. In the theory of transmission line, intrinsic capacitance  $C_i$  is defined directly by the thickness of  $d_i$  and width  $w$ , which is written as  $C_i = \frac{\epsilon w}{d_i}$ .  $C_{to}$ ,  $C_t$ ,  $C_b$ ,  $C_{bc}$  is capacitance between metal and capacitance of semi-conductor, which has lower influence and shown in figure 2-3. On the other side, under reverse bias, photo current is generated while electrical field crossed in absorption area, which also induced the inductance of magnetic field  $L_m$ .



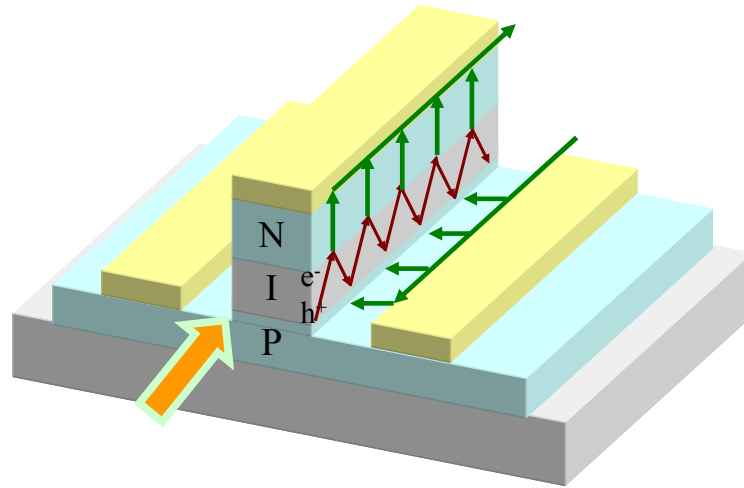


Figure 2- 2 Scheme of travelling wave photodiode

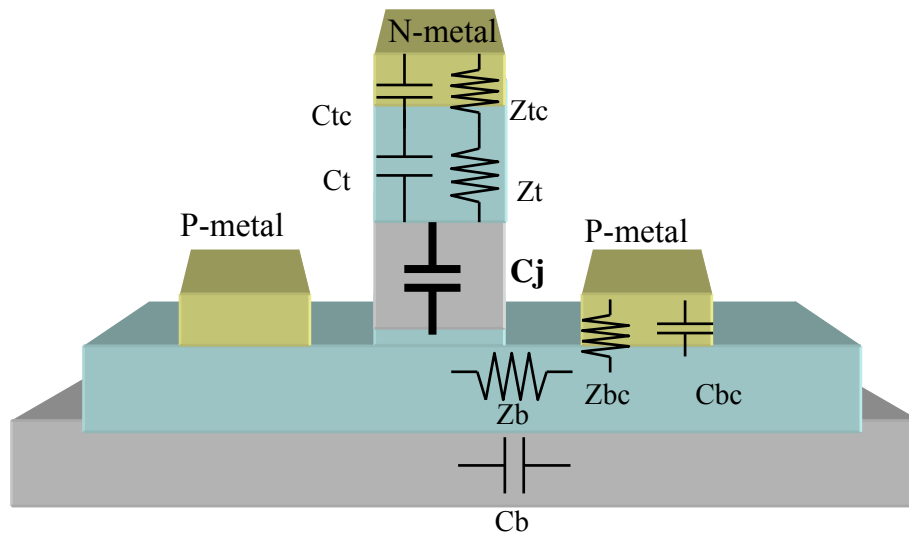
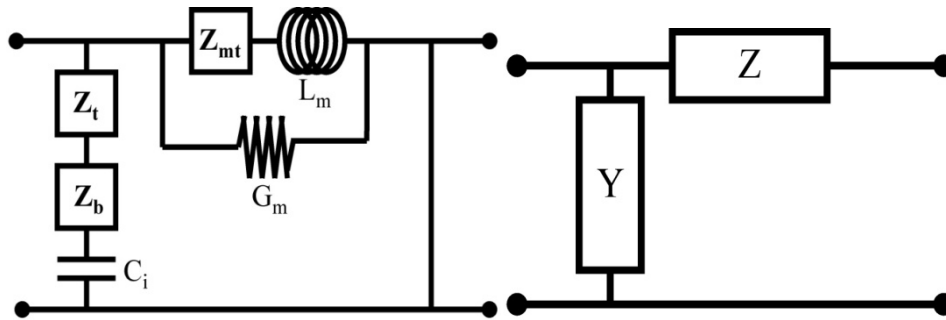


Figure 2- 3 An effective diagram of the device

Induced photocurrent generated by carriers in absorption area would pass through conductor layer which is the both side of intrinsic layer. As a result, both two conductor layer are equivalent with resistance  $Z_t$  and  $Z_b$ . Photocurrent is generated from intrinsic layer and then transmission with connected gold wire finally. Because current distribution, it is generated not only the resistance between metal and semiconductor  $Z_{ct}$ ,  $Z_{cb}$  and metal inductance  $L_m$ , but also skin effect on metal

surface. Such effect could be seen as parallel connection of resistance  $Z_{mt}$  and conductance  $G_m$  as shown in *figure 2-4*.



*Figure 2- 4(a)Equivalent circuit of photo diode and (b) simplified equivalent circuit of photo diode.*

Therefore we may know by the transmission line definition that the part the characteristic impedance is  $Z_0 = \sqrt{\frac{Z}{Y}}$ , The microwave propagation constant is  $\gamma_m = \sqrt{ZY} = \alpha_m + j \cdot \beta_m$ . Therefore after we obtain the part structure transmission electric properties, then simulate the frequency response of devices and to study its bandwidth performance.

## **2-3 Separated-Transport-Recombination Photodiode (STR-PD)**

### *Principal and problem of epi-layer structure for traditional photodiode*

In the traditional photodiode structure, we proposed two traditional photodiodes, make the principle discussion and analyze the epi-layer structure separately, which may affect bandwidth limitation and output power seriously. The encountered

problem and induced bottleneck is introduced as follows:

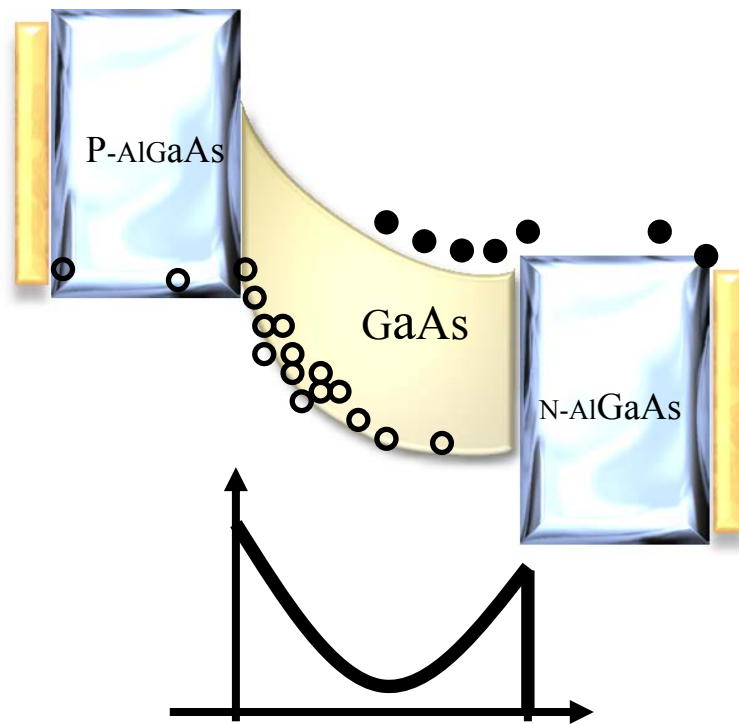


*Figure 2- 5 A schematic drawing of energy band and electric field distributed for traditional GaAs PD under high power excitation*

### ***Traditional PIN GaAs based Photodiode***

The traditional PIN GaAs PD is refers to that its material of absorption layer is composed by using only GaAs, which may reduce RC bandwidth limitation by increasing thickness of absorption layer. However, such reconstruct increase carrier drift time and lower devices speed and saturation current. In the other side, if we decrease absorption layer to achieve higher saturation current, problems caused such as serious bandwidth limitation and lower quantum efficiency. Moreover, under high input power excitation, too much photo carrier generated may cause the speed slow electricity hole accumulates in inner absorption layer, which will form a built-in field. [25-26] Such built-in field would screen external field and reduce devices speed and

output saturation current, which is so-called space charge screen effect. The trade-off problem between RC bandwidth limitation, carrier drift time and saturation current become a complex and hard test while design our devices.

### ***Traditional PIN LT-GaAs based PD***

Traditional PIN LTG-GaAs PD stands for its absorption layer are composed of by only low temperature grown GaAs. [24] Because there are lots of defects in LTG-GaAs, drift carrier generated will be captured and recombined, which means short carrier life time as shown in *figure 2-8*. [27] In other words, speed limitation of devices would transform from carrier drift time to carrier life time, this may improve devices speed a lot. By this method, trade off problem between capacitance bandwidth limitation and carrier drift time will be solved. It also improves space charge effect in this structure under higher input power excitation.

However, because LTG-GaAs in absorption layer is material with short carrier life time, most generated photo-carrier will be recombined and reduce quantum efficiency seriously. In the other side, there are much defects exists in absorption layer which may induce effect like heavy doping in absorption layer while applied external electrical field on the devices Thus depletion layer will exist in the junction layer between absorption layer and conduction layer. As a result, electrical field would be applied in conduction layer and lower internal electrical field in the absorption layer, which may limit carrier speed and limit speed and efficiency of devices.

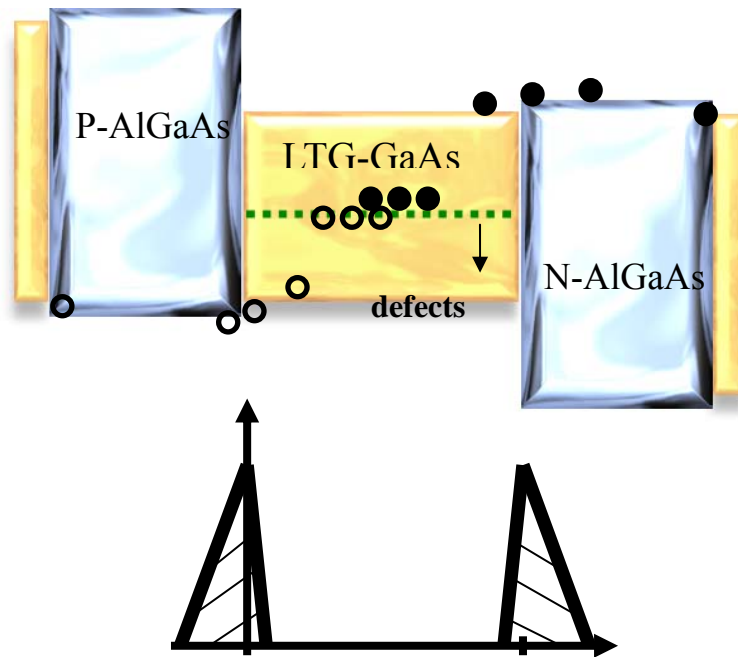


Figure 2- 6 Traditional LTG-GaAs PD energy band diagram and electrical field distribution.

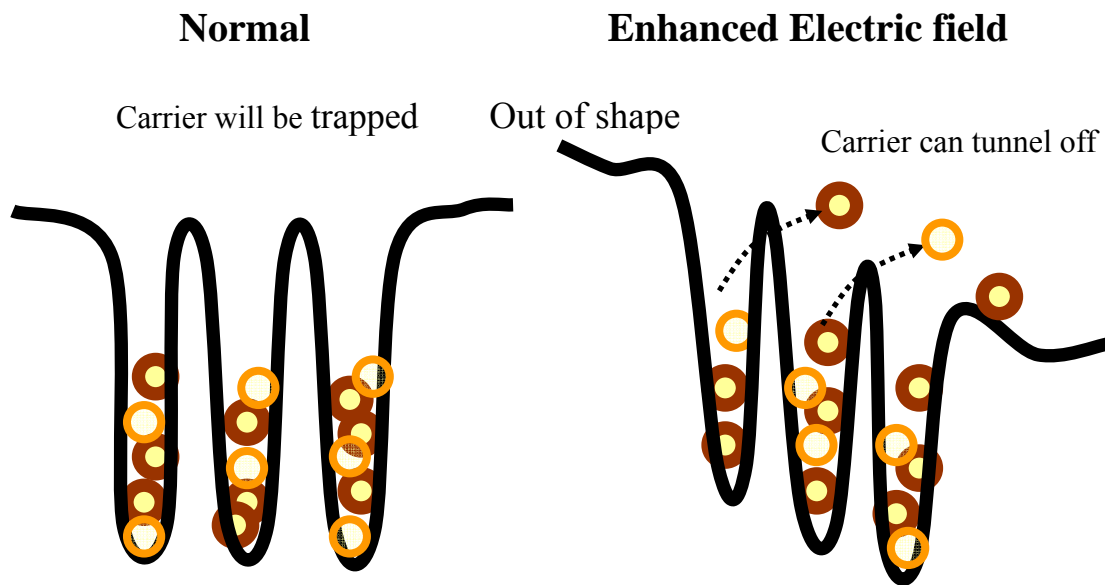


Figure 2- 7 A scheme of change for trap energy band

In order to apply electrical field in the absorption area, higher applied voltage on the devices is needed. However, when we apply higher voltage on the absorption area, speed of devices is not increased as expected. This is because carrier life time

increasing effect for LTG-GaAs, which means trap energy will change shape due to column effect under high applied voltage. [29-30] such effect may cause trapped carriers escaped from trap state in tuning mechanism, which means poor recombination effect and poor operation speed.

***Separated transmission recombined travelling wave PD (STR-PD)***

According to above two type traditional photodiode, we can learn trade off problems of speed, efficiency and saturation power will cause problem of design devices. Thus we propose a new type photo diode to solve the problem-- Separated transmission recombined travelling wave photo diode (STR-PD).

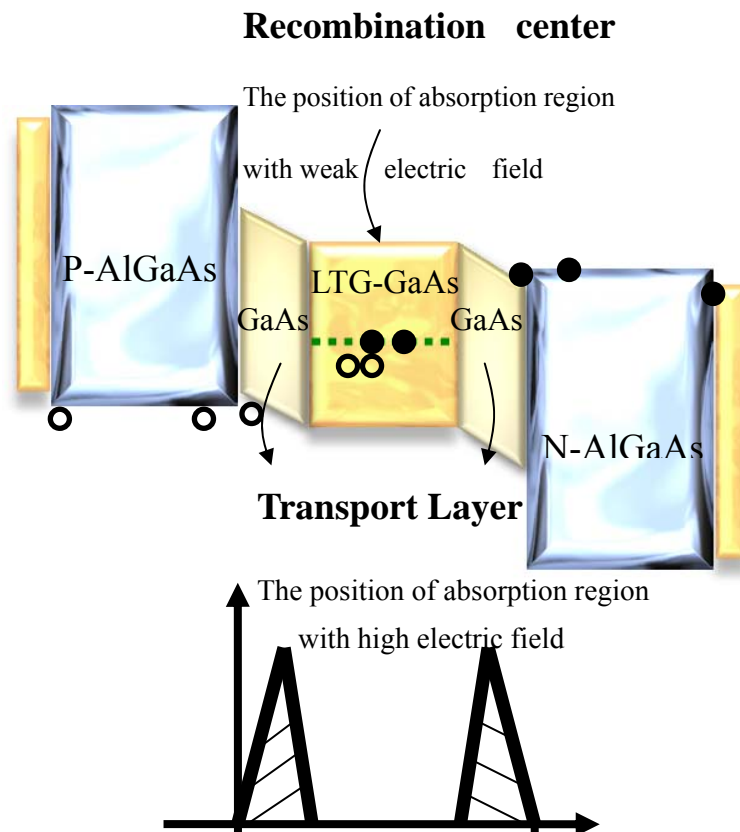


*Figure 2- 8 Schematic diagram of energy band and electrical field for STR-PD.*

We adopt travelling wave photo-diode type in PD's structure and recombination center (LTG-GaAs) in absorption layer. The STR-PD is composed of inserted LTG-GaAs in intrinsic layer GaAs and shown in figure 2-10.

***Principal of STR-PD***

Because we insert recombination center (LTG-GaAs) in absorption area, total absorption layer thickness become thinner and thus capacitance smaller. Besides, due to carriers in recombination center with slower speed trapped by defects, we could replace carrier drift time limitation by carrier life time. The higher speed performance is expected for carrier trapped time  $\ll$  carrier life time. The key point is we solved trade off problem between RC value and carrier drift time by inserted LTG-GaAs in traditional PIN PD, which we can improve devices performance a lot.

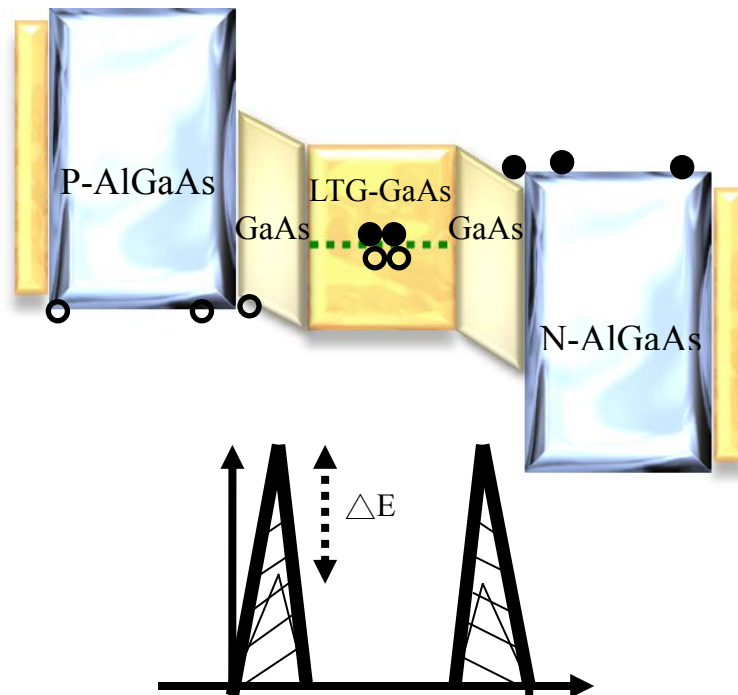


*Figure 2- 9 A schematic diagram of electrical field distribution for STR-PD while applied higher external field.*

Moreover, demanded thickness of conductor layer (intrinsic GaAs) could be thinner due to designed thickness of recombination center, thus higher saturation current could be expected while operated under this condition. As shown in figure 2-11, higher external electrical field mainly applied in collector layer which located on both side of LTG-GaAs having lots of defects and behavior like heavy doping. External electrical field is avoided to fall into recombination center, which avert life time increasing effect mentioned above under high external electrical field. Besides, under high power excitation, screen effect induced by accumulated electrical holes in absorption area would weaken electrical field in absorption center. However, the recombination center could trap carriers rapidly thus increase speed performance and maximum saturation current under high power excitation.

## **2-4 Uni-Traveling-Carrier Photodiode (UTC-PD)**

In order to solve the problem of lower quantum efficiency for LTG-GaAs based PD, we propose a novel design which has high speed and quantum efficiency by optimum doping concentration of absorption layer— uni-carrier transportation GaAs/AlGaAs Photodiode (GaAs/AlGaAs based UTC PD). The above mentioned travelling wave type PD is adopted in geometry structure for the novel device. In the other side, its epi-layer structure is shown in figure 2-12 that absorption layer is located in the p-doping area. The structure of UTC-PD includes P-type absorption layer with narrow energy band and N-type light doping with broad energy band as collector layer. Because quasi-neutral P-type absorption layer could relax major carriers (electrical holes) to contact metal, electrons are the only transmission carriers in UTC-PD.



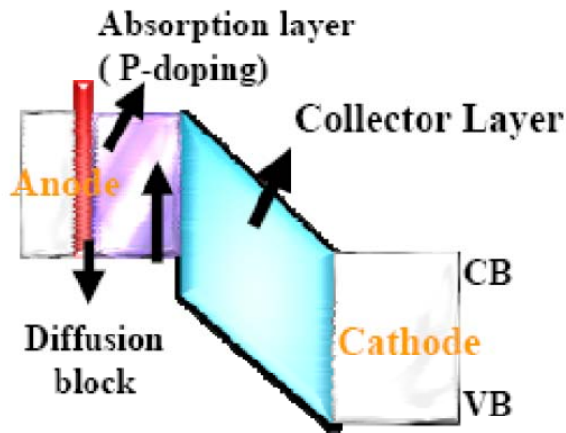


Figure 2- 10 Schematic epi-layer structure of GaAs/AlGaAs based UTC-PD

The transmission time of electrons determine transmission time of UTC-PD. Because it's fast for electrons to pass through conductor layer, we can reduce RC bandwidth limitation without sacrificing thickness of absorption area. Both electrons and electrical holes are not to be sacrificed and thus quantum efficiency could be increased. Moreover, a different space charge screening effect compared with traditional photo detector formed by electrons in intrinsic layer, which provided UTC-PD high output saturation current and high speed performance.

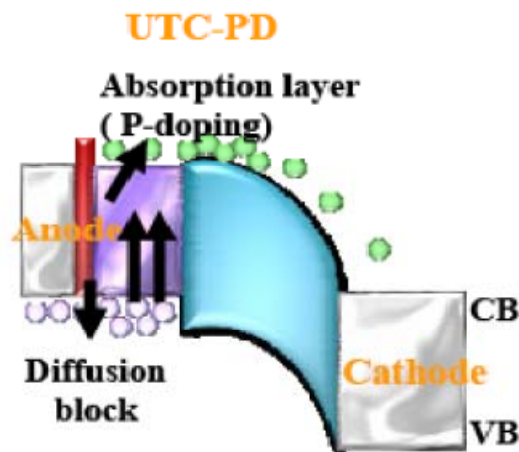


Figure 2- 11 A schematic diagram of UTC-PD while electrical holes relaxed by anode

Recently, InGaAs-InP based UTC-PD has been widely used in 1550 nm wavelength which is suitable for optical communication.[20] However, under light excitation with wavelength of 800nm, InGaAs-InP based UTC-PD has a problem that too much unwanted carriers generated in collector layer after InP absorbed light easily. Such unnecessary electrical pairs left in absorption area induce screening effect influence speed performance of device seriously, which has shown in figure 2-14.

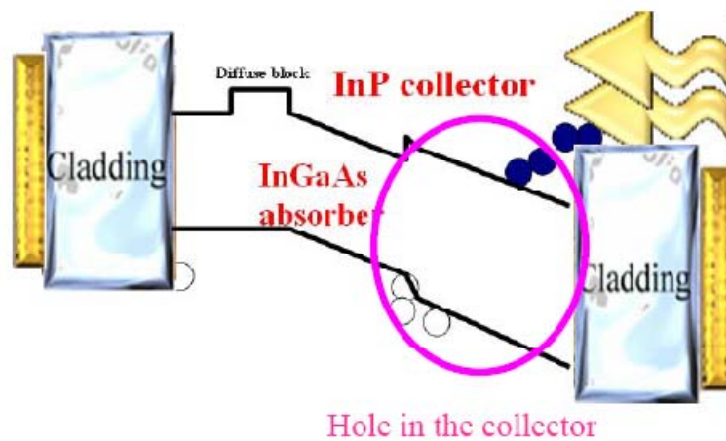


Figure 2- 12 A schematic band diagram of UTC-PD while incident light of wavelength 800nm

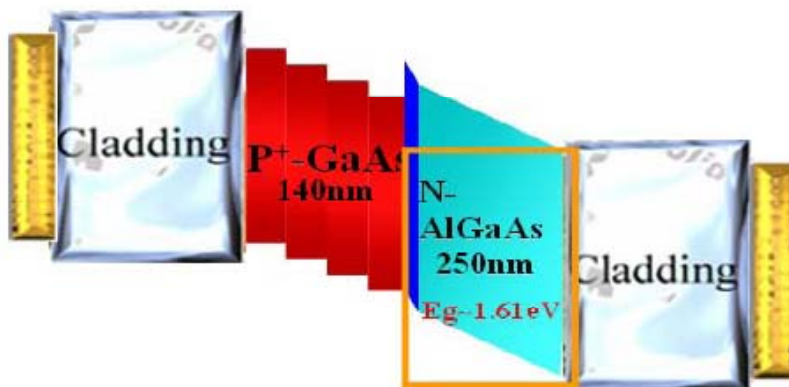


Figure 2- 13 A schematic diagram of UTC-PD design

To solve above problem, we design a collector layer with broad energy band ( $E_g \sim 1.61\text{eV}$ ) which could avoid unnecessary electron pairs generated in collector layer.[31] Moreover, the absorption layer is designed by optimizing doping

concentration of absorption layer which shape of energy band become stair step as shown in figure 2-15.

Such design could increase self-induced electrical field and speed up electrons to pass through conductor layer. Besides, we utilize the effect of UTC-PD that bandwidth increasing with optical power to surpass bandwidth performance of traditional PIN PD. The using of GaAs/AlGaAs in absorption layer and transmission layer make our device a high performance sub-THz transmitter at wavelength range of 850nm.

## 2-5 STR-PD Integrated with Slot Antennas

Both low-temperature-grown GaAs (LTG-GaAs) [6][7] and Uni-traevling-carrier photodiode (UTC-PDs)[6] based photonic-transmitters capture many attentions due to their excellent high-speed and high-power performance. However, under high reverse bias voltages, both devices usually suffer from the saturation of output THz power. Such phenomenon can be attributed to the intervalley scattering of photo-generated electrons and life-time increasing effect [9] for the cases of UTC-PDs and LTG-GaAs based photodetectors, respectively. On the other hand, for most reported photonic-transmitters operating in millimeter and sub-millimeter wavelengths regimes, Si lenses are usually required for increasing the antenna radiation efficiency [6,7,33]. However, this integration will not only increase the cost of packaging but decrease some THz radiation due to the coupling loss into dielectric material [10]. In addition, the distance from the center to the edge of the Si-lens is also an obstacle to the optical beam coupled into the side-illumination photodetectors. In this paper, we demonstrated a novel photonic structure, which is composed of a LTG-GaAs based edge-coupled separated-transport-recombination photodiode (STR-PD) and a micromachined co-planar-waveguide (CPW) fed slots antenna. Under femto-second optical pulse excitation, our device radiates strong sub-THz waves ( $\sim 5\mu\text{W}$  averaged power) at the designed resonant frequency ( $\sim 500\text{GHz}$ ) without using Si-lens. By adopting the LTG-GaAs based STR-PD as the active part of our transmitter, the reported saturation phenomenon of traditional LTG-GaAs based photonic-transmitter, under high applied external electrical fields, [6,9] has also been eliminated.

### ***Device Structure:***

The top-view of demonstrated THz photonic-transmitter is shown in Figure1, which is composed of a high-speed edge-coupled STR-PD [11], a radio frequency (RF) isolation bias tee, and an co-planar-waveguide (CPW) fed slots antenna [6,22]. We adopted such kind of antenna as our radiator due to being easily integrated with the active STR-PD and higher radiation power than spiral antennas at the designed resonant frequency. The RF isolation bias tee, which operates as an inductance, avoids the high frequency ac current leaking into the dc probe pad and decreases the radiation efficiency. By using the techniques of selective wet chemical etching and back-side lithography, fraction of GaAs substrate, which below the slots antenna can be removed and the fabricated slots antenna will stand on the AlGaAs membrane with a 5 $\mu$ m thickness. Except for the membrane slots antenna, other area of the photonic-transmitter chip is still above a robust GaAs substrate to endure the wire-bonding process for device package. With a relatively thin membrane ( $\sim$ 5 $\mu$ m), compared with the operating wavelength (hundreds of  $\mu$ m) of THz signal, the problem of substrate mode can be eliminated [35] and the radiated THz power can be enhanced without using Si-lens. The inset in *figure 2-16* shows the simulated frequency response of our transmitter without considering the influence of active photodiode. We can clearly see the designed resonant frequency of slots antenna is around 500GHz. Regarding with the active part of our demonstrated transmitter, it is a STR-PD and has been demonstrated in our previous work [34]. A LTG-GaAs layer with an extremely short carrier lifetime [36] is inserted in the center of its active region to serve as a recombination center and two surrounded high-quality GaAs-based depletion layers serve as depleted transport layers [34]. Compared with the traditional p-i-n photodiode, STR-PD can minimize the space-charge-screening

effect under high-power operation and exhibit much better speed and output power performance under both pulse-mode and continuous-wave operations [34,37].

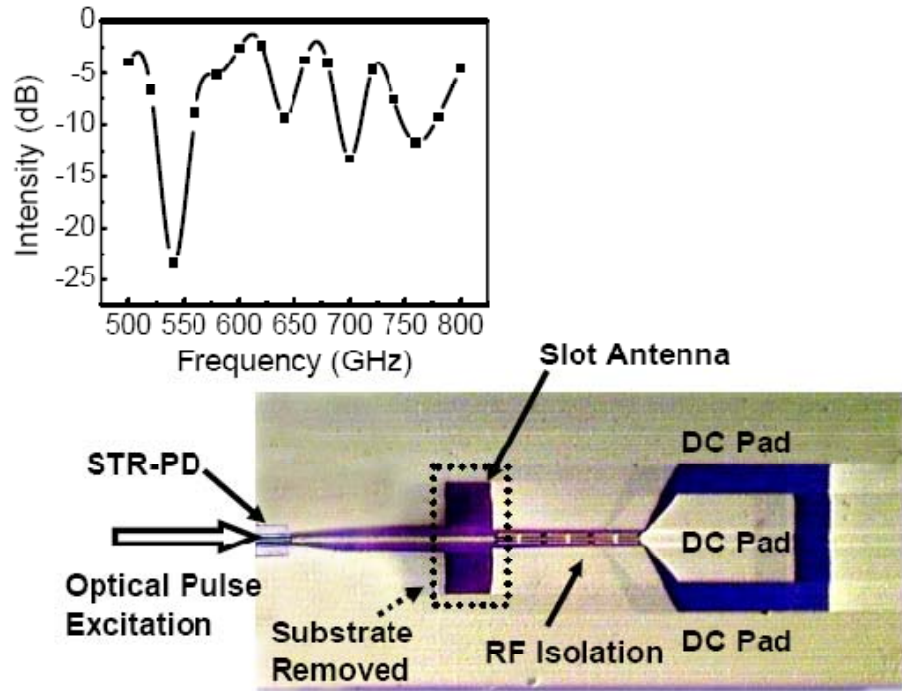


Figure 2- 14 Top-view of fabricated photonic-transmitter.

( The left side arrow indicates the direction of input optical pulse. The inset shows the simulated frequency response of slot antenna. A significant resonance at around 500GHz operating frequency has been observed .)

## **2-6 STR/ UTC-PD integrated with Circular Antenna**

To make a fair comparison of their dynamic performance, both the STR-PD and UTC-PD based transmitters share the same geometric structure. A top-view and conceptual cross-sectional view are shown in Figure 2-17 (a). The antenna design adopted in this work is a co-planar-waveguide (CPW) fed circular disk monopole antenna [38]. As can be seen in the cross-sectional view, part of the GaAs substrate of both devices just below the circular disk of the antenna has been removed by selective wet etching and back-side lithography to enhance the THz emission of the emitter without necessitating the integration of an additional Si-lens [29]->[39]. Furthermore, a tapered and periodically corrugated edge, which is specified for inductance, can be seen on the top-view of the device. A circular disk antenna is integrated to improve the radiation characteristics, particularly at frequencies near the higher band edge [38].

Figure 2-17 (b) shows the simulated frequency response of the microwave reflection parameter (S11) for the antenna structure. By using the -10dB line on the y-axis as a reference it can be seen that there is low reflection loss (<-10dB) for most of the frequency component (100GHz to 350GHz) in the simulated frequency band (70GHz to 350GHz) [20]. The inset to Figure 1 shows the simulated waveforms for the radiated electrical pulse from our substrate-removed antenna. The electrical pulse from the photodiode is considered Gaussian in shape with a full-width half maximum (FWHM) around 4ps. The simulation is carried out with a finite-difference time-domain simulation tool (SEMCAD, Schmid & Partners Engineering. AG, Zurich, Switzerland).

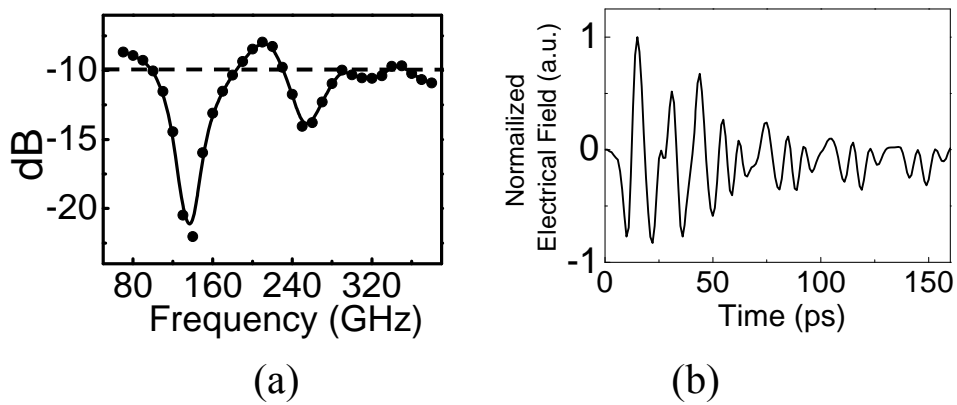
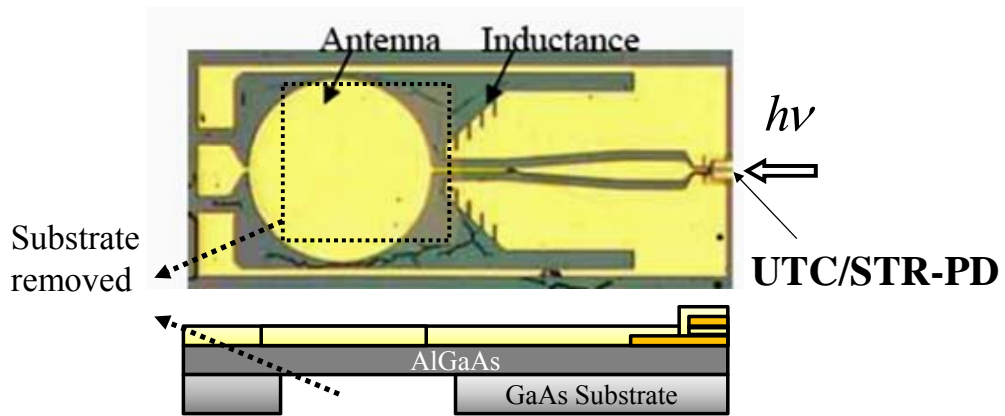


Figure 2- 15 Top-view and cross-sectional view of the demonstrated sub-THz PT.

Inset (a) shows the simulated frequency response of the designed antenna. Inset (b) shows the simulated impulse response of the antenna.

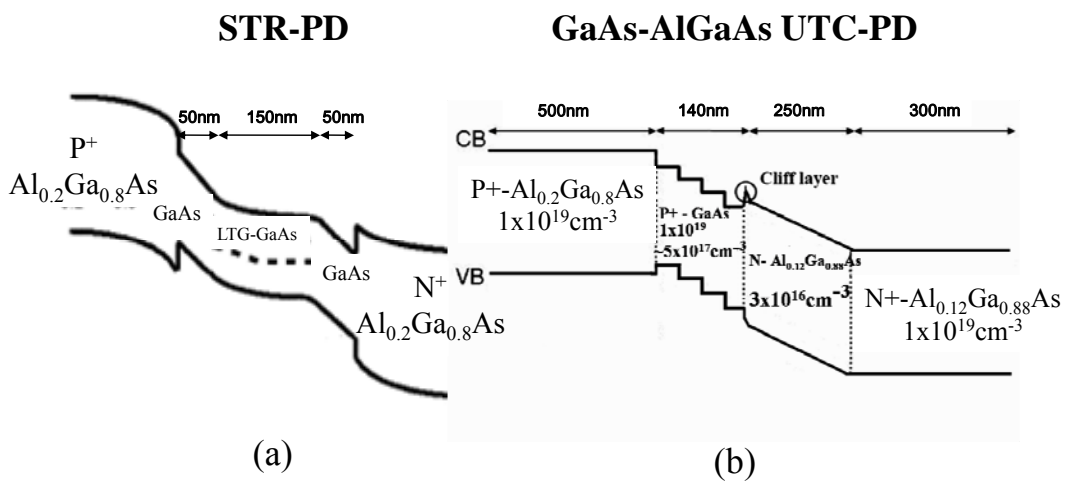


Figure 2- 16 Conceptual band diagrams of the demonstrated



Figure 2-18 shows conceptual band diagrams of the demonstrated (a) STR-PD (b) and UTC-PD [22,25]. In the STR-PD, a LTG-GaAs layer with a short carrier lifetime (less than 1 ps) is inserted into the center of the absorption region and surrounded by two high quality GaAs-based photo-absorption layers to serve as a recombination center. As shown in (a), the external applied electric field is concentrated in the two GaAs layers. This is due to the high defect density and field-screening effect of the inserted LTG-GaAs layer [22]. These two photo-absorption layers can, thus, be treated as a “transport layer” or “depletion layer” in our structure. They have much higher mobility compared to the LTG-GaAs and the concentration of the applied electric field. The STR-PD demonstrates superior output power performance over that of the traditional p-i-n PD even though the thickness of the total absorption layer is the same [22]. This is due to the fact that in the STR-PD the real drift-distance of photo-generated carriers can be roughly approximated by the thickness of the one-sided GaAs based transport layer (a thickness of only 50nm) instead of the total absorption region (with a thickness of up to 250nm). A smaller drift-distance means that a shorter drift-time, less SCS effect in the absorption region, and a higher saturation power can be expected [13]. Furthermore, the inserted LTG-GaAs based recombination center has high resistivity, which can also reduce the junction capacitance (RC-limited bandwidth) over that of the traditional p-i-n PD with its thin absorption (depletion) layer for high-power performance [22].

The UTC-PD is composed of a GaAs based photo-absorption layer with a graded p-type doping profile, which acts to accelerate the drift-velocity of the photo-generated electrons [19] and the  $\text{Al}_{0.15}\text{Ga}_{0.85}\text{As}$  based collector layer. The graded doping profile of the absorption layer has a larger slope, which induces the

appropriate built-in electric field (2.1 to 84 kV/cm) and ensures the occurrence of electron drift for the over-shoot velocity. Thus our UTC-PD has a more significant bandwidth enhancement effect under a much lower output photocurrent density than the traditional InP based UTC-PD [19]. The collector layer consists of an n-type doped ( $3 \times 10^{16} \text{ cm}^{-3}$ )  $\text{Al}_{0.15}\text{Ga}_{0.85}\text{As}$  layer, 250nm in thickness, with a bandgap of around 1.61eV. This enables one to avoid the undesired photo-absorption process that occurs around the 800nm wavelength excitation. The n-type doping in the collector layer can also suppress the current blocking effect and further improve the high power performance of UTC-PD [13]. An n+ doped ( $5 \times 10^{18} \text{ cm}^{-3}$ )  $\text{Al}_{0.15}\text{Ga}_{0.85}\text{As}$  cliff layer is inserted between the collector layer and the absorption layer [40]. A UTC-PD structure that utilizes only electrons as the active carriers has superior high-power performance to the traditional p-i-n PD due to the much higher drift-velocity of the electrons than of the holes, and the great reduction in the drift-time of the photo-generated carriers. In short, we use different approaches to shorten the drift-time of photo-generated carriers: one approach is the reduction of the effective carrier drift-distance in the STR-PD and the other is the increasing of the drift-velocity in the UTC-PD. Both of these structures exhibit superior high-power performance over that of a p-i-n PD with the same total depletion layer thickness [40].

## Reference

- [1] H. Eisele, A. Rydberg, and G. I. Haddad, "Recent advances in the performance of InP Gunn devices and GaAs TUNNET diodes for the 100–300-GHz frequency range and above," *IEEE Trans. Microwave Theory Tech.*, vol. 48, pp. 626–631, Apr. 2000.
- [2] N. Orihashi, S. Suzuki, and M. Asada, "One THz harmonic oscillation of resonant tunneling diodes," *Appl. Phys. Lett.*, vol.87, 233501,2005.
- [3] R. Köhler, A. Tredicucci, F. Beltram, H. E. Beere, E. H. Linfield, A. G. Davies, D. A. Ritchie, R. C. Iotti, and F. Rossi, "Terahertz semiconductor-heterostructure laser" *Nature*, vol. 417, pp156-159, May, 2002 .
- [4] S. Barbieri, J. Alton, S. S. Dhillon, H. E. Beere, M. Evans, E. H. Linfield, A. G. Davies, D. A. Ritchie, R. Kohler, A. Tredicucci, and F. Beltram, "Continuous-wave operation of terahertz quantum-cascade lasers," *IEEE J. Quantum Electron.*, vol. 39, pp. 586–591, April, 2003.
- [5] C. Walther, M. Fischer, G. Scalari, R. Terazzi, N. Hoyler, and J. Faist, "Quantum cascade lasers operating from 1.2 to 1.6 THz" *Appl. Phys. Lett.*, vol. 91, 131122, Sep., 2007.
- [6] H. Ito, T. Furuta, F. Nakajima, K. Yoshino, T. Ishibashi, "Photonic Generation of Continuous THz Wave Using Uni-Traveling-Carrier Photodiode" *J. of Lightwave Technol.*, 23, 4016, 2005.
- [7] M.-C. Tien, H.-H. Chang, J.-Y. Lu, L.-J. Chen, S.-Y. Chen, R.-B. Wu, W.-S. Liu, J.-I. Chyi, and C.-K. Sun, "Device saturation behavior of submillimeter-wave membrane photonic transmitters," *IEEE Photon. Technol. Lett.*, 16, 873, 2004.

- [8] S. Verghese, K. A. McIntosh, and E. R. Brown, "Highly Tunable Fiber-Coupled Photomixers with Coherent Terahertz Output power", *IEEE Trans. Microwave Theory Tech.*, 45, 1301, 1997.
- [9] S. M. Duffy, S. Verghese, K. A. McIntosh, A. Jackson, A. C. Gossard, and S. Matsuura, "Accurate modeling of dual dipole and slot elements used with photomixers for coherent terahertz output power," *IEEE Trans. Microwave Theory Tech.*, vol. 49, pp. 1032 – 1038, June 2001.
- [10] H. Togo, P.-C. P. Sah, N. Shimizu, and T. Nagatsuma, "Gigabit impulse radio link using photonic signal-generation techniques," in *Eur. Microwave Conf. 2005*, vol. 1, pp. 4–7, Oct. 2005.
- [11] T. -A. Liu, G. -R. Lin, Y.-C. Chang, C.-L. Pan, "Wireless audio and burst communication link with directly modulated THz photoconductive antenna," *Optic. Express*, vol.13, Issue 25, pp. 10416-10423, Dec., 2005.
- [12] Lothar Möller, John Federici, Alexander Sinyukov, Chongjin Xie, Hee Chuan Lim, and Randy C. Giles, "Data encoding on terahertz signals for communication and sensing," *Opt. Lett.*, vol. 33, pp. 393-395, Feb. 2008.
- [13] K. Kato, "Ultrawide-Band/High-Frequency Photodetectors," *IEEE Trans. Microwave Theory Tech.*, vol. 47, pp. 1265-1281, Jul., 1999.
- [14] L. Y. Lin, M. C. Wu, T. Itoh, T. A. Vang, R. E. Muller, D. L. Sivco, and A. Y. Cho, "High-power High-speed Photodetectors Design, Analysis, and Experiment Demonstration," *IEEE Trans. Microwave Theory Tech.*, vol. 45, pp. 1320-1331, Aug., 1997.
- [15] S. Demiguel, N. Li, X. Li, X. Zheng, J. Kim, J. C. Campbell, H. Lu, and A. Anselm, "Very High-Responsivity Evanescently Coupled Photodiodes Integrating a Short Planar Multimode Waveguide for High-Speed Applications," *IEEE*

- Photon. Technol. Lett., vol. 15, pp.1761-1763, Dec., 2003.
- [16] Y.-S. Wu, J.-W. Shi, P.-H. Chiu, and Wei Lin “High-Performance Dual-Step Evanescently-Coupled Uni-Traveling-Carrier Photodiodes” IEEE Photon. Technol. Lett., vol. 19, pp. 1682-1684, 2007.
- [17] Y.-L. Huang and C.-K. Sun, “Nonlinear saturation behaviors of high-speed p-i-n photodetectors,” J. of Lightwave Technol., vol. 18, pp. 203-212, Feb., 2000.
- [18] H. Ito, S. Kodama, Y. Muramoto, T. Furuta, T. Nagatsuma, T. Ishibashi, “High-Speed and High-Output InP-InGaAs Unitraveling-Carrier Photodiodes,” IEEE J. of Sel. Topics in Quantum Electronics, vol. 10, pp. 709-727, Jul./Aug., 2004.
- [19] J.-W. Shi, Y.-T. Li, C.-L. Pan, M. L. Lin, Y. S. Wu, W. S. Liu, and J.-I. Chyi, “Bandwidth enhancement phenomenon of a high-speed GaAs-AlGaAs based unitraveling carrier photodiode with an optimally designed absorption layer at an 830nm wavelength” Appl. Phys. Lett, vol. 89, pp.053512 2006.
- [20] Yu-Tai Li, J.-W. Shi, C.-Y. Huang, N.-W. Chen, S.-H. Chen, J.-I. Chyi, and Ci-Ling Pan, “Characterization of Sub-THz Photonic-Transmitters Based on GaAs/AlGaAs Uni-Traveling Carrier Photodiodes and Substrate-Removed Broadband Antennas for Impulse-Radio Communication,” IEEE Photon. Technol. Lett., vol. 20, pp.1342-1344, Aug., 2008.
- [21] X. Li, N. Li, S. Demiguel, X. Zheng, J. C. Campbell, H. H. Tan, and C. Jagadish, “A Partially Depleted Absorber Photodiode With Graded Doping Injection Regions,” IEEE Photon. Technol. Lett., vol. 16, pp.2326-2328, Oct., 2004.
- [22] J.-W. Shi, H.-C. Hsu, F.-H. Huang, W.-S. Liu, J.-I. Chyi, Ja-Yu Lu, Chi-Kuang Sun, and Ci-Liang Pan, “Separated-Transport-Recombination p-i-n Photodiode for High-speed and High-power Performance” IEEE Photon. Technol. Lett, vol.

17, pp. 1722-1724, Aug., 2005.

- [23] S. Gupta, J. F. Whitaker, and G. A. Mourou, "Ultrafast Carrier Dynamics in III-V Semiconductors Grown by Molecular-Beam Epitaxy at Very Low Substrate Temperatures," *IEEE J. of Quantum Electronics*, vol. 28, pp.2464-2472, Oct., 1992.
- [24] K. Kato, "Ultrawide-Band/High-Frequency Photodetectors," *IEEE Trans. Microwave Theory Tech.*, vol. 47, pp. 1265-1281, Jul., 1999.
- [25] Kirk Steven Giboney, Ph. D. Thesis, University of California at Santa Barbara, 1995
- [26] Yi-Jen Chiu, Ph. D. Thesis, University of California at Santa Barbara, 1999
- [27] S. Gupta, J. F. Whitaker, and G. A. Mourou, "Ultrafast Carrier Dynamics in III-V Semiconductors Grown by Molecular-Beam Epitaxy at Very Low Substrate Temperatures," *IEEE J. of Quantum Electronics*, vol. 28, pp.2464-2472, 1992.
- [28] J. P. Ibbetson, Ph. D. Thesis, University of California at Santa Barbara, 1998.
- [29] J.-W. Shi, Y.-H. Chen, K. G. Gan, Y. J. Chiu, John. E. Bowers, M.-C. Tien, T.-M. Liu, and C.-K. Sun, "Nonlinear Behaviors of Low-Temperature-Grown GaAs-Based Photodetectors Around 1.3- $\mu$ m Telecommunication Wavelength" *IEEE Photon. Tech. Lett.*, vol. 16, pp.242-244, Jan., 2004.
- [30] C.-K. Sun, Y.-Hung Chen, J.-W. Shi, Y.-J. Chiu, K. G. Gan, and J. E. Bowers, "Electron relaxation and transport dynamics in low-temperature-grown GaAs under 1eV optical excitation" *Appl. Phys. Lett.*, vol. 83, pp. 911-913, Aug., 2003.
- [31] M. Levinshtein, S. Rumyantsev, and M. Shur, *Handbook Series of Semiconductor Parameters*, World Scientific, Singapore, 1996.
- [32] N. Li, X. Li, S. Demiguel, X. Zheng, J. C. Campbell, D. A. Tulchinsky, K. J. Williams, T. D. Isshiki, G. S. Kinsey, and R. Sudharsanan,

- “High-saturation-current charge-compensated InGaAs-InP uni-traveling-carrier photodiode” *IEEE Photon. Tech. Lett.*, vol. 16, pp. 864-866, 2004.
- [33] N. Zamdmer, Q. Hu, K. A. McIntosh, and S. Verghese, “Increase in response time of low-temperature-grown GaAs photoconductive switches at high voltage bias,” *Appl. Phys. Lett.*, vol. 75, pp. 2313–2315, Oct. 1999.
- [34] K. S. Giboney, M. J. W. Rodwell, and J. E. Bowers, “Traveling-wave photodetector theory,” *IEEE Trans. Microw. Theory Tech.*, vol. 45, no. 8, pt. 2, pp. 1310–1319, Aug. 1997.
- [35] K. C. Gupta, R. Garg, I. Bahl, and P. Bhartia, *Microstrip Lines and Slotlines*. Boston, London: Artech House, 1996.
- [36] J. W. Shi, Y.-T. Li, C.-L. Pan, M. L. Lin, Y. S. Wu, W. S. Liu, and J. I. Chyi, “Separated-transport-recombination p-i-n photodiode (STR-PD) with high-speed and high-power performance under continuous-wave (CW) operation,” in *Conf. Laser and Electro-Optics (CLEO/QELS 2006)*, 2006, OSA Tech. Dig., Paper CTuS6.
- [37] D. H. Martin and E. Puplett, “Polarised interferometric spectrometry for the millimeter and submillimeter spectrum,” *Infrared Phys.*, vol. 10, pp. 105–109, Jun. 1970.
- [38] Y.-C. Liang and N.-W. Chen, “An ultra-broadband coplanar waveguide-fed circular monopole antenna,” *EuCAP 2007*, Edinburgh, UK, Nov., 2007.
- [39] G. M. Rebeiz, “Millimeter-wave and terahertz integrated circuit antennas,” *Proceedings of IEEE*, vol. 80, pp. 1748-1770, 1992.
- [40] H. Ito, S. Kodama, Y. Muramoto, T. Furuta, T. Nagatsuma, T. Ishibashi, “High-Speed and High-Output InP-InGaAs Unitraveling-Carrier Photodiodes,” *IEEE J. of Sel. Topics in Quantum Electronics*, vol. 10, pp. 709-727, Jul., 2004.

# Chapter 3 Photoconductive Antennas

In this chapter, we introduce the background of THz radiation and describe the motivation of this research about ion-implanted material for photoconductive antennas. The basic theories about THz radiation generated from dipole antenna are mentioned both on pulse and CW mode. Finally, the results are analyzed and a summary and future work of this research work will be given.

## 3-1 Introduction

A primary technique of generating short pulses of microwave and THz waves is by irradiating a biased semiconducting photoconductor with femtosecond (fs) optical pulses.[1] The semiconductor materials reported span Cr-doped GaAs [2], ion-implanted silicon-on-sapphire (SOS) [3], GaAs thin films grown by low temperature molecular beam epitaxy (LT-GaAs)[4] and InP[5]. Of all these materials, LT-GaAs, which has been developed initially for mitigating back-gating and side-gating effects in GaAs integrated circuits, enjoys the advantages of high dark resistivity, high breakdown field strength, ultrashort carrier lifetime and relatively high carrier mobility simultaneously. Unfortunately, there always exist variations of film properties in LT-GaAs caused by the difficulties of measuring and controlling the wafer temperature during epitaxial growth. On the other hand, ion implantation into GaAs wafers has been researched quite extensively for making pulsed THz devices.

The implanted species include proton [9,10], nitrogen [10,11], arsenic [10,12,13] and oxygen[10, 13]. According to Salem et al [10], these materials all make good pulsed THz emitters except the nitrogen-implanted GaAs. Furthermore, Salem et al.



points out the comparative advantage of oxygen implanted GaAs over arsenic implanted GaAs in terms of the emitted THz power. [13] More recently, attention has shifted to the emitted power and power conversion efficiency [15] of THz emitters.

Surprisingly, Zhao et al [14] reports a very simple structure fabricated by directly painting two silver-paste electrodes on a semi-insulating GaAs wafer separated by a wide gap of at least 0.4mm. Yet the device can emit 40 $\mu$ W of THz power with a peak at 0.5 THz. This power level is just surpassed by that of Taylor et al [15], where a very sophisticated epitaxial structure consisting of a distributed Bragg reflector and an active composite film composed of ErAs particles embedded in GaAs has been employed. This device emits 44  $\mu$ W with a peak at 0.3 THz when pumped by only 8.7mW of laser power, meaning a record high conversion efficiency of about 0.5%. Inspired by this result and that of Salem et al [13], we investigated the fabrication and characterization of high power THz photoconductive (PC) dipole antennas using oxygen-implanted GaAs (GaAs:O). As a control, we also fabricated identical devices on LT-GaAs and compared the performance between devices made from these two materials. GaAs:O has been selected in this investigation because it is not difficult to prepare. Kang et al [16] and Lederer et al [17] have separately measured subpicosecond carrier trapping time in oxygen-doped GaAs epilayer and subpicosecond response time in oxygen-implanted GaAs, respectively. The high resistivity of the oxygen-implanted GaAs is guaranteed as a result of the midgap level introduced by oxygen.

Before embarking in a detailed study of GaAs:O and related PC devices, one should know what the advantage of GaAs:O materials is, and also its disadvantage. Its first advantage comes from its preparation method. The ion implantation method has two main advantages compared with the Low temperature MBE (Molecular Beam

Epitaxy) or MOCVD (Metalorganic chemical vapor deposition). One is its reproducibility. User can easily repeat the preparation condition time by time, without changing too much in the material characteristics from sample to sample. The other one is its tailor ability. The properties of material can be tailored by selected suitable implant energy, ion dosage and the post annealing temperature. With this kind of preparation method, one can grow materials with certain characteristics easily, according to his (her) own purpose. And, as the oxygen is common component of air, it is easy to be found and extracted for implantation usage comparing with other kind of ions, which need to be bombarded out from bulk material or powder. And oxygen is harmless (nontoxic) and cheaper comparing with those ions like As<sup>+</sup>, Er<sup>+</sup>, and therefore it will cause less risk on Environmental pollution

The defects caused by the O<sup>+</sup> ion in GaAs material endows other advantages for GaAs:O materials, as listed in the following:

1. High dark resistance. As mentioned above, the energy level formed by Oxygen ions in the material is close to the Fermi level, which makes the material close to electrical neutral. The general resistivity of GaAs:O can be as high as 10<sup>6</sup>Ωcm.

2. A reasonable carrier lifetime (in subpicosecond range). O<sup>+</sup> ions form lots of defects (carrier trapping center) in the GaAs material during the implantation process. The higher defects concentration in it, the shorter carrier lifetime (carrier trapping time) it will have.

3. High saturation level. The existing of O<sup>+</sup> defects increases the saturation level of GaAs:O material. Comparing with LTG GaAs material, GaAs:O has higher pump power saturation level and bias field saturation level. These allow one to add higher pump power and bias onto the PC devices, which at the end generate higher output power of THz wave.

As mentioned above, in THz generation area, GaAs:O material has been demonstrated in pulsed generation mode by B.Salem, et al.[16,18] (A group in Canada). They used multi-implanted GaAs:O with a dosage level  $10^{13}\text{cm}^{-2}$  to study its THz wave generation performance, and compared it with other kinds of ion-implanted material, such as GaAs:As, GaAs:H, and GaAs:N. But they haven't compared the generation performance of GaAs:O with LTG GaAs, which occupies the dominative position of PC devices at 800 nm pumping range. And they haven't gone further and compared the effect of dosage in the power generation and THz spectrum. There still lots of space were left for one to do further study on this area, even without including the possible application using GaAs:O based PC devices. Following their work, we have demonstrated our partial study work on GaAs:O based THz PC devices in pulsed generation mode [19], and the CW THz generation mode in the middle of 2007[20],which will be discussed later, respectively. For CW terahertz generation from GaAs:O, it is almost at the same time (a little early than ours), another group from Germany, I.Camara Mayorga et al. [17] published their very detailed study works on the high energy ion (2 and 3 MeV) implanted GaAs:O material. It should be cheerful that on this road we are not lonely. They have compared the THz wave generation performance of GaAs:O material not only with different implant energy and dosage, but also other material like GaAs:N. Their hard work promotes the study on GaAs:O material in CW THz area to a new high level.

## **3-2 Basic Theory**

This mechanism of generated THz radiation from the biased photoconductive switch is generally based on the theory, which is called “current surge model” [21].

We will discuss the basic theory of this model in detail in next chapter. According to this model, as the energy of the input laser is higher than the energy of bandgap of photoconductor, then electron-hole pairs are excited and the mechanism of generated THz radiation can occur.

In briefly, the electromagnetic field of THz radiation is generated from a transient current which is generated on the surface of the photoconductor. The pulse laser generates carriers instantaneously. We add a bias to accelerate the carriers. Then, the resultant transient current, or be called current surge, produces an electric field on the surface of the photoconductor. This surface electric field is regarded as the source of the THz radiation. *Figure 3-1* shows the setup for this method.

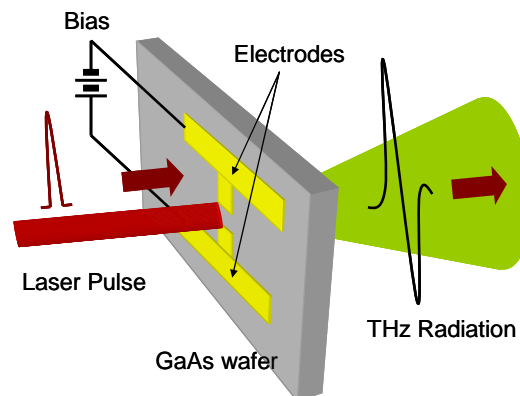


*Figure 3- 1 A schematic diagram for pulsed THz generation by PC antenna*

We put two electrodes on the top of substrate which can use different materials, such as GaAs, low temperature grown GaAs (LT-GaAs). This photoconductor behaved as an isolation without illuminate optical source. When we give the voltage across two electrodes and illuminate the region between two electrodes, the substrate becomes conducting. Under the influence of the applied electric field, current starts to flow. A time dependent current can also radiate transient electric field with a higher efficiency than optical rectification. The

frequency contents of this transient are determined by the transient behavior of the current and have 3dB bandwidth of 1 THz typically and roughly.

### ***Drude-Lorentz model***

For the calculation of carrier transport and THz radiation in a biased semiconductor, the one-dimensional Drude-Lorentz model is used. When a biased semiconductor is pumped by a laser pulse with photon energies greater than the band gap of the semiconductor, electrons and holes will be created in the conduction band and valence band, respectively. The carrier pumped by ultrashort laser pulse is trapped in the mid-gap states with the time constant of the carrier trapping time. The time-dependence of carrier density is given by the following equation.

$$\frac{dn(t)}{dt} = -\frac{n(t)}{\tau_c} + G(t) \quad (3-1)$$

Where  $n(t)$  is the density of the carrier,  $G(t)$  is the generation rate of the carrier by the laser pulse, and  $\tau_c$  is the carrier trapping time. The generated carriers will be accelerated by the bias electric field. The acceleration of electrons (holes) in the electric field is given by

$$\frac{d\nu_{e,h}(t)}{dt} = -\frac{\nu_{e,h}(t)}{\tau_s} + \frac{q_{e,h}}{m_{e,h}} E \quad (3-2)$$

Where  $\nu_{e,h}(t)$  is the average velocity of the carrier,  $q_{e,h}$  is the charge of an electron (a hole),  $m_{e,h}$  is the effective mass of the electron (hole),  $\tau_{e,h}$  is the momentum relaxation time, and  $E$  is the local electric field. The subscript e and h represent electron and hole, respectively. The local electric field  $E$  is smaller than

the applied bias electric field  $E_b$  due to the screening effects of the space charges,

$$E = E_b - \frac{P}{\alpha\varepsilon} \quad (3-3)$$

Where P is the polarization induced by the spatial separation of the electron and hole,  $\varepsilon$  is the dielectric constant of the substrate and  $\alpha$  is the geometrical factor of the PC material. The geometrical factor  $\alpha$  is equal to three for an isotropic dielectric material. It is noted that both, the free and trapped carriers contribute to the screening of the electric field. The time dependence of polarization P can be written as

$$\frac{dP}{dt} = -\frac{P}{\tau_r} + J \quad (3-4)$$

Where  $\tau_r$  is the recombination time between an electron and hole. In the equation (3-4), J is the density of the current contributed by an electron and hole,

$$J = en\nu_h - en\nu_e \quad (3-5)$$

Where e is the charge of a proton. The change of electric currents leads to electromagnetic radiation according to Maxwell's equations. In a simple Hertzian dipole theory, the far-field of the radiation  $E_{\text{THz}}$  is given by

$$E_{\text{THz}} \propto \frac{\partial J}{\partial t} \quad (3-6)$$

To simplify the following calculations, we introduce a relative speed  $\nu$  between an electron and hole,

$$\nu = \nu_h - \nu_e \quad (3-7)$$

Then the electric field of THz radiation can be expressed as

$$E_{\text{THz}} \propto e\nu \frac{\partial n}{\partial t} + en \frac{\partial \nu}{\partial t} \quad (3-8)$$

The first term on the right hand side of the equation (3-8) represents the

electromagnetic radiation due to the carrier density change, and the second term represents the electromagnetic radiation which is proportional the acceleration of the carrier under the electric field.

### ***CW THz generated by Photomixing***

CW THz wave can be generated through photomixing which produces optical intensity beating at THz frequencies by mixing two single-mode lasers or mode beating within a single laser. The combination of two waves with slightly different frequencies is equivalent to a wave which envelope is modulated by the difference frequency. The intensity-modulated beam will excite the electron-hole pairs in PC antennas then accelerated by the bias voltage applied to the PC antennas. The generated THz frequency is as the same as the optical beating frequency.

When two electric fields with slightly different frequencies propagate collinearly into biased PC antennas, beating signal will be radiated. Set two parallel, scalar electric fields as:

$$\begin{aligned} E_1(t) &= E_{10}(t)\text{Cos}(w_1t + \phi_1) \\ E_2(t) &= E_{20}(t)\text{Cos}(w_2t + \phi_2) \end{aligned} \quad (3-9)$$

Where  $E_{10}$ ,  $E_{20}$ ,  $w_1$ ,  $w_2$ ,  $\phi_1$  and  $\phi_2$  are the amplitude, angular frequency and constant phases of wave 1 and wave 2, respectively. And the total electric field is the superposition of the two waves:

$$E(t) = E_1(t) + E_2(t) = E_1\text{Cos}(w_1t + \phi_1) + E_2\text{Cos}(w_2t + \phi_2) \quad (3-10)$$

From the simulated curves of figure 2-1-2, we can see that the total electric field has the waveform with a slowly various envelope and a fast carrier frequency inside.

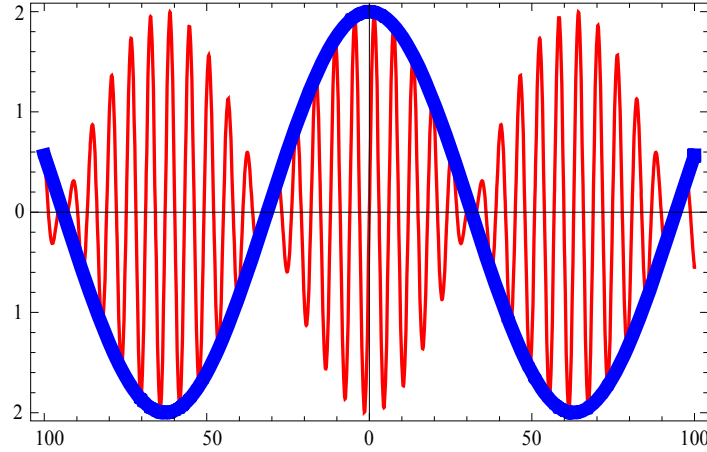


Figure 3- 2 The simulated curves of two wave with slightly different frequencies.

(The thin curve is the sum of the two waves. The thick curve is the plot of the wave with frequency of  $(\omega_1 - \omega_2)/2$ )

The laser frequency is about  $10^{15}$  Hz, but the fast detector response time  $T$  is just about  $10^{-12}$  s. We can ignore these faster terms in equation (2.1-26), so the equation can be written as:

$$\begin{aligned}
 I_{beat}(t) &= \frac{c\epsilon_0 E_1^2}{2} + \frac{c\epsilon_0 E_2^2}{2} + c\epsilon_0 E_1 E_2 \text{Cos}[(\omega_1 - \omega_2)t + (\phi_1 - \phi_2)] \text{Sinc}\left[\frac{(\omega_1 - \omega_2)T}{2}\right] \\
 &= I_1 + I_2 + 2\sqrt{I_1 I_2} \text{Cos}[\Omega t + \phi]
 \end{aligned}
 \tag{3-11}$$

The first two terms are the average intensities of wave 1 and wave 2, respectively.  $\Omega$  is the difference of angular frequency between two waves.  $\phi$  is the phase different of the two waves (figure 3-2).

### 3-3 Material of Photoconductive Antenna

*Low-temperature (LT) grown GaAs*



Low-temperature (LT) grown GaAs is widely used as the photoconductive substrate of PC antennas for generation and detection of THz radiation because of the high resistivity ( $10^7 \Omega cm$ ) [11-22] and good mobility ( $100-300 cm^2/Vs$ ) [12-13-23-24], in addition to short carrier lifetime ( $< 1ps$ ) [14-15-25-26]. These excellent characteristics are however difficult to reproduce from sample because the quality of the material depends critically on both the growth temperature and the post growth thermal annealing conditions. An alternative material was reported to be promising as the substrate material of PC antennas, which is the arsenic ion-implanted GaAs [16-27]. These materials exhibit good structural and electrical properties and show ultrafast optoelectronic response. It is again possible to improve the carrier mobility of these ion-bombarded materials using postimplantation thermal annealing process. Good control over the overall fabrication process allows studies of the influence of parameters such as the ion-implantation dose, the ion energy, and the thermal annealing conditions on the PC antenna characteristics.

#### ***Material of ion-implanted GaAs***

The arsenic (As) ion implanted GaAs PC antennas have shown to be better THz emitters than those made on semi-insulating (Si) GaAs substrates [17-20 28-31]. It has demonstrated that the terahertz emission property of arsenic ion-implanted GaAs has almost the same characteristics with Low-temperature (LT) grown GaAs. Such enhancement results from ultrafast carrier recombination associated with the presence of the implantation-induced defects. On the other hand, several groups have shown good characteristics of THz emitters with the use of PC antennas made on GaAs substrates grown by the Czochralski method when these devices are photoexcited near the anode. Although defects seem to play a crucial role in the characteristics of THz PC antenna emitters, there are very few studies that investigate the role of defects on

these characteristics. Ion-implantation using other types of ions has already been used successfully to reduce the carrier lifetime in Si GaAs. For example, subpico-second lifetime can be obtained in GaAs:H GaAs:N and GaAs:O [32-37].

In this study, we report the fabrication and characterization of THz emitters on multi-implanted GaAs:O, one of which is capable of emitting a record high power of 48  $\mu$ W within 0.1-0.5THz when excited by 25mW of laser power. We also show that emitters made on either GaAs:O or LT-GaAs exhibit similar power levels. The experimental results and discussions will be described in below.

Our implantation design was to get as a uniform distribution of oxygen ions as possible in the top 1 $\mu$ m layer of the GaAs substrate so that most of the pump power could be absorbed. The implantation was carried out in a 2MV tandem accelerator, where the cost of implantation limited us to the following two sets of conditions: (High-Dose)  $1 \times 10^{14}/\text{cm}^2$  at 1200keV,  $6 \times 10^{13}/\text{cm}^2$  at 800keV and  $6 \times 10^{13}/\text{cm}^2$  at 500keV; and (Low-Dose)  $4 \times 10^{13}/\text{cm}^2$  at 1200keV,  $2.5 \times 10^{13}/\text{cm}^2$  at 800keV and  $2.5 \times 10^{13}/\text{cm}^2$  at 500keV. The peak ion concentration calculated from SRIM2003 simulation was around  $2.3 \times 10^{18}/\text{cm}^3$  in the High-Dose samples. The substrates were high-resistivity ( $>10^8 \Omega\text{cm}$ ) semi-insulating GaAs wafers. Rapid thermal annealing (RTA) under  $\text{N}_2$  gas environment at 550 $^\circ\text{C}$  or 500 $^\circ\text{C}$  for 60s was performed with a GaAs cap wafer on all the implanted wafers to prevent loss of As.

### **3-4 Antenna Types**

We used the dipole antenna as the antenna structure in our experiment. Large signal and high bandwidth can be obtained from this kind of structure [38]. The photoconductive antenna structure is shown in *Figure 3-3*. Knon et al. proved that

the spectral response of the PC antenna for broadband detection is mainly determined by the temporal behavior of the number of photo-excited carriers [26].

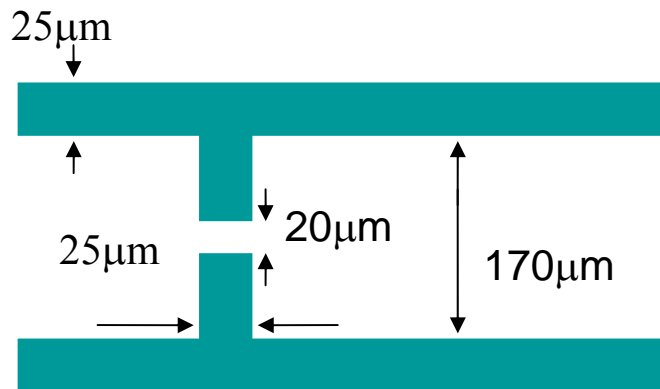


*Figure 3- 3 Schematic diagram of the PC antenna*

Recently, Salem et al. [17] improved the characteristics of GaAs substrate and generated THz waves by implanting oxygen ion. Normally, oxygen ion is considered as dust (a disadvantage) for electrical devices fabrication during the process, as its existence will make the contacts to be not Ohmic-contact. But, in the THz generation, it can become advantages. As the electrical level formed by oxygen ion in GaAs is close the Femi-level, it makes the oxygen ion implanted GaAs close to electrically neutral and has comparative high resistance. This kind of material also have high breakdown voltage; and short carrier lifetime by implanted under certain high dosage and annealed under suitable annealing temperature.

### **3-5 Properties of Photoconductive Antennas**

#### *Carrier life time measurement*

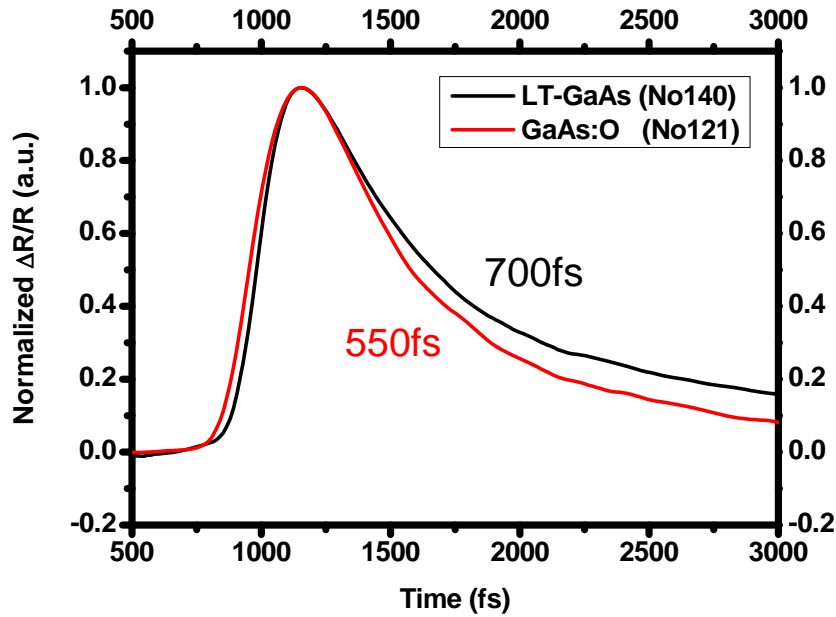


Figure 3- 4 The measurement of carrier life time with both materials

By optimize the dosage and the implanted energy to match the requirements. Considering the cost of time for RBS facility, we prepared two kinds of materials which have different carrier life times and mobilities as the same dipole antenna structure. In implanting process, multi-implants dosage concentrations is *low dose*  $2.5 \times 10^{13}$  ions/cm<sup>2</sup> (500Kev & 800Kev) and  $4 \times 10^{13}$  ions/cm<sup>2</sup> (1200kev). After implantation process, we performed the thermal annealing by RTA (Rapid Thermal Annealing) under N<sub>2</sub> gas environment and use a GaAs cap to prevent As ion absorption. In our experiment, we performed annealing at 500°C for 60s. (For reference, under 500°C for 60s annealing, the resistance of this GaAs:O substrate is close to  $1.26 \times 10^7$  (Ω/sq)) and we also measured the carrier life time of both materials by optical-pump probe measurement. The carrier life time of GaAs:O is 550fs and LT-GaAs is 700fs. The fitting curve are shown in figure 3-4.

**Conductivity measurement**

We also calculated the conductivity of GaAs:O and LT-GaAs. The conductivity of GaAs:O is  $3.8 \times 10^{-2} \Omega^{-1} \text{cm}^{-1}$  and LT-GaAs is  $1.7 \times 10^{-4} \Omega^{-1} \text{cm}^{-1}$ , the measurement are shown in figure 3-5 and 3-6.

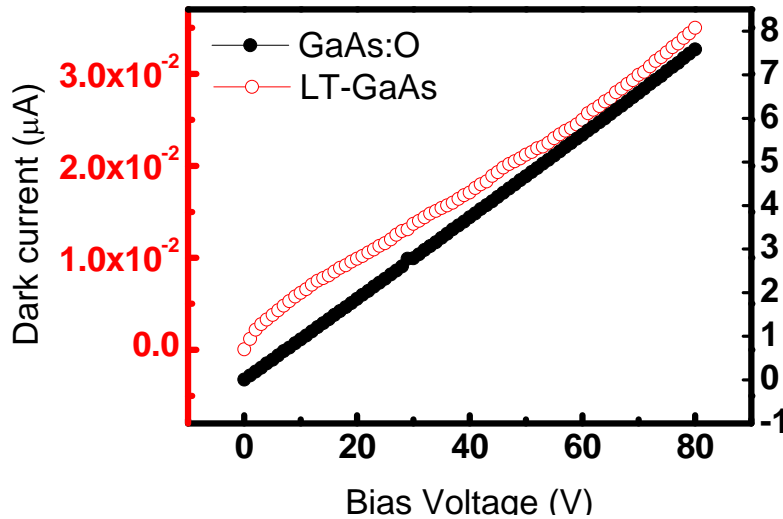


Figure 3- 5 I-V Curve of GaAs:O and LTG-GaAs

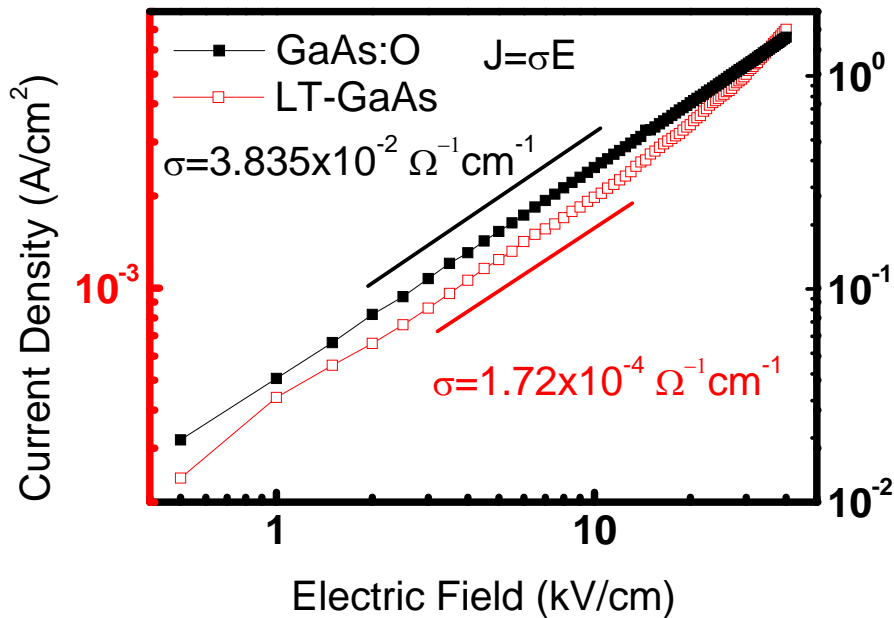


Figure 3- 6 Current density v.s. Electrical field of LTG-GaAs and GaAs:O

**Current-voltage (I-V) curve (Pulse mode)**

Figure 3-7 shows the current-voltage characteristics result of the PC dipole

antenna with the same structure, one of material is GaAs:O and the other is LT-GaAs. The beam illuminated at the gap of PC antenna, with incident power of 30mW. We also measured the dark current which was without the pump power. It can easily confirm from Figure 3-7 that the I-V curve is a linear curve at low bias voltage and a quadratic curve at higher bias voltage. This means that the current is proportion to the bias we gave at low bias voltage and quadratic proportion to higher bias voltage. We can observe that increasing ratio of GaAs:O is higher than LT-GaAs. We observe that the dark current of the GaAs :O is higher than LT-GaAs, the net photocurrent of GaAs:O is 3 times to that of the LT-GaAs when the bias is at 80V and there is no saturation effect in current bias curve for both materials pumping with pulse laser.

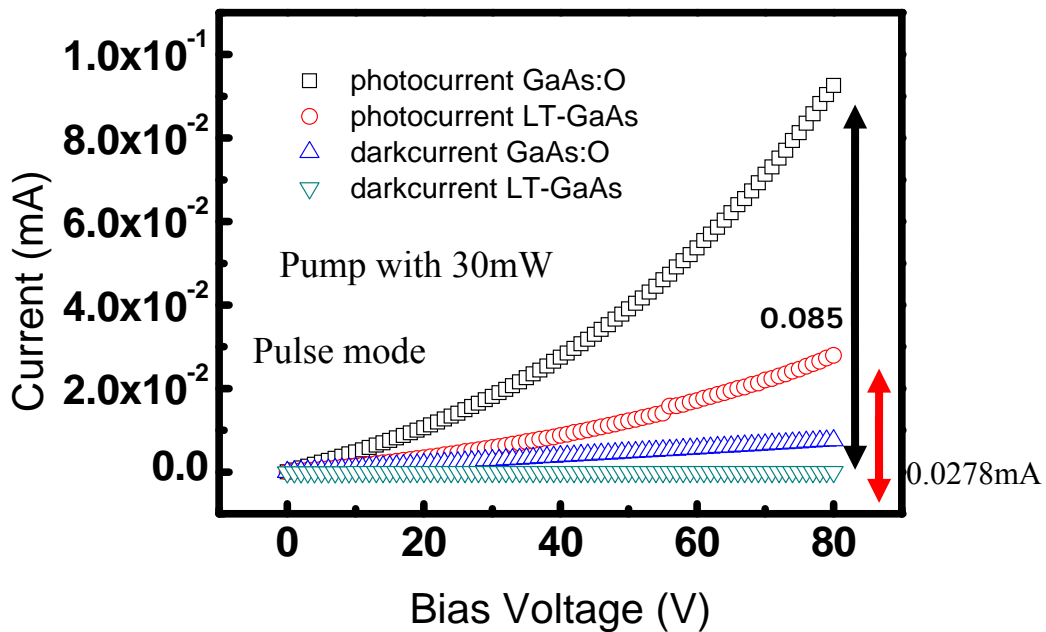


Figure 3- 7 I-V curve of GaAs:O antennas and LT-GaAs antennas under pulse excitation

**Current-voltage (I-V) curve (CW mode)**

In this section we used two frequency dependent laser diodes to produce beating at

THz frequency. Then we illuminated laser beams to the antenna with the same structure under different fabricated material. Figure 3-8 shows the current-voltage characteristic result, one of material is GaAs:O and the other is LT-GaAs. The incident power was 180mW and the beam illuminated to the gap of PC antenna. We measured the dark current without pump power before. It can easily confirm from Figure 3-8 that the I-V curve is a linear curve at high bias voltage and a sub-linear curve at lower bias voltage, the sub-linear region is due to the electron drift velocity saturation [45] and super-linear region is due to the increase of carrier life time [46], and it means that the current is proportion to the bias we gave at higher bias voltage and sub-linear proportion to lower bias voltage. We can also observe that increasing ratio of GaAs:O is higher than LT-GaAs. Although that the dark current of the GaAs:O is higher than LT-GaAs, the net photocurrent of GaAs:O is 3 times to LT-GaAs and there is no current saturation effect in both material pumping with CW laser.

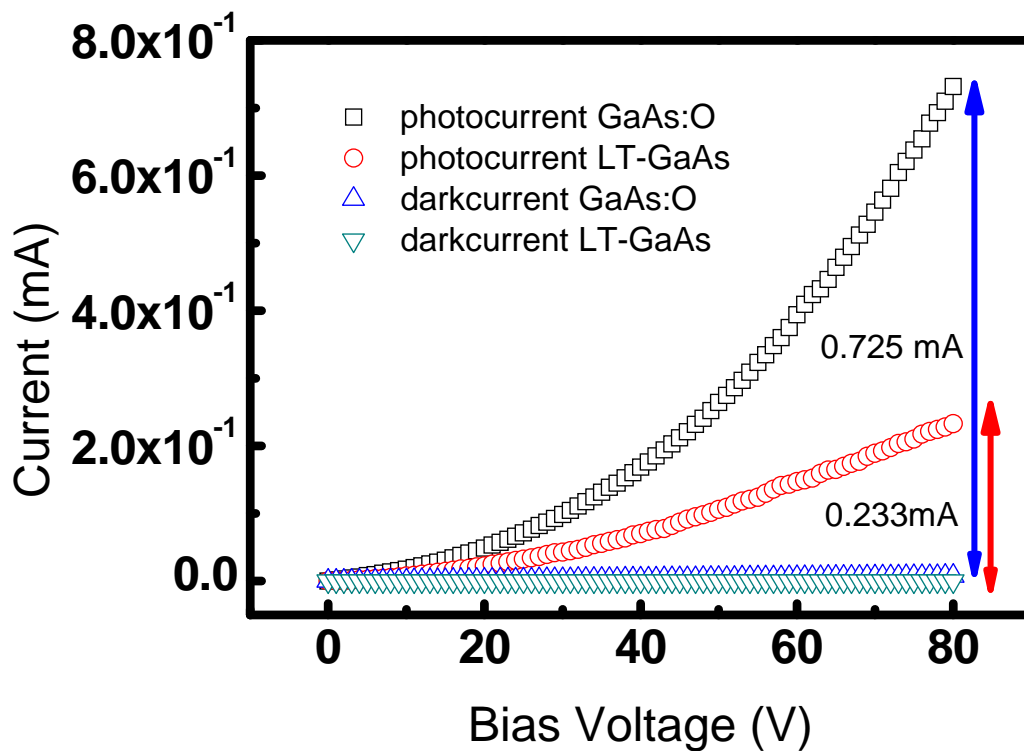


Figure 3- 8 I-V curve of GaAs:O antennas and LT-GaAs antenna under CW laser pumping

## Reference

- [1] M.S.Sherwin, S. C.A, and P. H. Bucksbaum, "Opportunities in THz Science," Arlington, VA February 12-14, 2004.
- [2] G. Mourou, C. V. Stancampiano, A. Antonetti, and A. Orszag, *Appl. Phys. Lett.* 39, 295-296, 1981.
- [3] M. Vanexter and D. R. Grischkowsky, *IEEE Tran. on Microwave Theory and Techniques* 38, 1684-1691, 1990.
- [4] F. W. Smith, H. Q. Le, V. Diadiuk, M. A. Hollis, A. R. Calawa, S. Gupta, M. Frankel, D. R. Dykaar, G. A. Mourou, and T. Y. Hsiang, *Appl. Phys. Lett.* 54, 890-892, 1989.
- [5] J. T. Darrow, B. B. Hu, X. C. Zhang, and D. H. Auston, *Opt. Lett.* 15, 323-325, 1990.
- [6] F. W. Smith, A. R. Calawa, C.L. Chen, L.J Mahoney, M.J. Manfra, J.C. Huang, and F.H. Spooner, *High Speed Semiconductor Devices and Circuits*, 1987.
- [7] *Proceedings, IEEE/Cornell Conference on Advanced Concepts in*, 229-238, 1987.
- [8] M.Y. Frankel, J.F. Whitaker, G.A. Mourou, F.W. Smith, and A.R. Calawa, *IEEE Tran. on Electron Devices* 37, 2493-2498, 1990.
- [9] K. A. McIntosh, K. B. Nichols, S. Verghese, and E. R. Brown, *Appl. Phys. Lett.* 70, 354-356, 1997.
- [10] C. S. Wong, J. M. Dai, and H. K. Tsang, *Appl. Phys. Lett.* 75, 745-747 (1999).  
B. Salem, D. Morris, V. Aimez, J Beerens, J. Beauvais, and D. Houde, *Journal of Physics-Condensed Matter* 17, 7327-7333, 2005.
- [11] F. Peter, S. Winnerl, S. Nitsche, A. Dreyhaupt, H. Schneider, and M. Helm,



- Appl. Phys. Lett. 91, ,2007.
- [12] T. A. Liu, M. Tani, and C. L. Pan, J. Appl. Phys. 93, 2996-3001, 2003.
- [13] B. Salem, D. Morris, Y. Salissou, V. Aimez, S. Charlebois, M. Chicoine, and F. Schiettekatte, Journal of Vacuum Science & Technology A 24, 774-777, 2006.
- [14] G. Zhao, R. N. Schouten, N. van der Valk, W. T. Wenckebach, and P. C. M. Planken, Review of Scientific Instruments 73, 1715-1719, 2002.
- [15] Z.D. Taylor, E.R. Brown, J. E. Bjarnason, M. P Hanson, and A. C. Gossard, Opt. Lett. 31, 1729-1731, 2006.
- [16] J. U. Kang, M. Y. Frankel, J. W. Huang, and T. F. Kuech, Appl. Phys. Lett. 70, 1560-1562, 1997.
- [17] B. Salem, D. Morris, Y. Salissou, V. Aimez, S. Charlebois, M. Chicoine, and F. Schiettekatte, "Terahertz emission properties of arsenic and oxygen ion-implanted GaAs based photoconductive pulsed sources," Journal of Vacuum Science & Technology A, vol. 24, pp. 774-777, May-Jun 2006.
- [18] I. C. Mayorga, E. A. Michael, A. Schmitz, P. van der Wal, R. Gusten, K. Maier, and A. Dewald, "Terahertz photomixing in high energy oxygen- and nitrogen-ion-implanted GaAs," Applied Physics Letters, vol. 91, pp. -, Jul 16 2007.
- [19] B. Salem, D. Morris, V. Aimez, J. Beerens, J. Beauvais, and D. Houde, "Pulsed photoconductive antenna terahertz sources made on ion-implanted GaAs substrates," Journal of Physics-Condensed Matter, vol. 17, pp. 7327-7333, Nov 23, 2005.
- [20] Chen Kejian, Li Yutai, Cheung Wingyiu, Wang Weiwen, Pan Ciling, and Chan Kamtai, "THz WAVES GENERATED BY OXYGEN IMPLANTED GaAs," in 2007 International Symposium on Antennas and Propagation Niigata Convention

Center, Niigata, Japan, 2007.

- [21] K. Chen, Y. Li, W. Cheung, W. Wang, C. Pan, and K. Chan, "CW Sub-Terahertz wave generation by GaAs:O Materials," in Lasers and Electro-Optics - Pacific Rim, 2007. CLEO/Pacific Rim 2007.
- [22] Smith, F.W. Smith, F. W.; Le, H. Q.; Diadiuk, V.; Hollis, M. A.; Calawa, A. R.; Gupta, S.; Frankel, M.; Dykaar, D.R., "Picosecond GaAs-based photoconductive optoelectronic detectors." Appl. Phys. Lett. Vol.54, 890, 1989.
- [23] M. Tani, K. Sakai, and H. Mimura, "Ultrafast Photoconductive Detectors Based on Semi-Insulating GaAs and InP" Jpn. J. Appl. Phys., Part2, Vol.36, L1175, 1997
- [24] D. C. Look, Thin Solid Films 231, 61, 1993.
- [25] C. Ludwig and J. Kuhl, "Studies of the temporal and spectral shape of terahertz pulses generated from photoconducting switches." Appl. Phys. Lett. Vol.69, 1194, 1996.
- [26] S. Kono, M. Tani, And K. SaKai, "Ultrabroadband photoconductive detection: comparison with free-space electro-optic sampling" Appl. Phys. Lett., Vol.79, No.7, pp. 898-900, 2001.
- [27] A. Claverie, F. Namavar, and Z. Lilorntal-Weber, "Formation of As precipitates in GaAs by ion implantation and thermal annealing." Appl. Phys. Lett. Vol.62, 1271, 1993.
- [28] Liu T-A, Tani M and Pan C-L "THz radiation emission properties of multienergy arsenic-ion-implanted GaAs and semi-insulating GaAs based photoconductive antennas" J. Appl. Phys. Vol.93, 2996, 2003.
- [29] Lin G-R, and Pan C-L "Characterization of optically excited terahertz radiation from arsenic-ion-implanted GaAs" Appl. Phys B Vol.72, 151, 2001.

- [30] Lloyd-Hughes J, Castro-Camus E, Fraser M D, Jagadish C and Johnston M B  
Phys. Rev. B 70 235330, 2004.
- [31] Liu T-A, Tani M, Nakajima M, Hangyo M and Pan C-L “Ultrabroadband terahertz field detection by photoconductive antennas based on multi-energy arsenic-ion-implanted GaAs and semi-insulating GaAs.” Appl. Phys. Lett. Vol.83, 1322, 2003.
- [32] M. Lambsdorff, J. Kuhl, J. Rosenzweig, A. Axmann, and Jo. Schneider, “Subpicosecond carrier lifetimes in radiation-damaged GaAs.” Appl. Phys. Lett. Vol.58, 1881, 1991.
- [33] M. J. Lederer, B. Luther-Davies, H. H. Tan, C. Jagadish, M. Haiml, U. Seifner, and U. Keller, “Nonlinear optical absorption and temporal response of arsenic- and oxygen-implanted GaAs.” Appl. Phys. Lett. Vol.74, 1993, 1999.
- [34] B. Salem, D. Morris, V. Aimez, J. Veerens, J. Beauvais and D. Houde. “Pulsed photoconductive antenna terahertz sources made on ion-implanted GaAs substrates” J. Phys.: Condens. Matter 17 7327-7333, 2005.
- [35] M. Mikulics, E. A. Michael, M. Marso, M. Lepsa, A. van der Hart, and H. Lüth, A. Dewald, S. Stanček and M. Mozolik, P. Kordoš, “Traveling-wave photomixers fabrication on high energy nitrogen-ion-implanted GaAs”, Appl. Phys. Lett. Vol.89, 071103, 2006.
- [36] B.Salem, D.Morris, Y.Salissou, V.Aimez and S.Charlebois, M.Chicoine, F. Schiettekatte, “Terahertz emission properties of arsenic and oxygen ion-implanted GaAs based photoconductive pulsed sources” J.Vac.Sci. Technol. A 24(3), pp.774-777, 2006.
- [37] B.Salem, D.Morris, V.Aimez, J. Beauvais and D. Houde, “Improved characteristics of a terahertz set-up built with an emitter and a detector made on

proton-bombarded GaAs photoconductive materials” *Semicond. Sci. Technol.* Vol.21, 283-286, 2006.

- [38] P. Uhd Jepsn, R. H. Jacobsen, and S. R. Keiding, “Generation and detection of terahertz pulses from biased semiconductor antennas,” *J. Opt. Soc. Am. B*, **Vol.13**, pp. 2424-2436, 1996.

# Chapter 4 Experimental Methods for Characterization of THz Waves

## 4-1 Introduction

In order to identify characterizations of our THz devices, power and electrical field measurement system at this range is needed. There are lots of tools could be used for this frequency range recently and following are brief introduction of some instruments in our experiments. First, power of THz radiation is measured by liquid-helium cooled bolometer. As for some devices designed in the sub –THz, for example, W-band, a RF power meter is usually used. Besides, to further study the radiated electrical field, there are different ways which are developed in recent years, such as photoconductive antenna and electro-optic sampling (EO sampling).

Far-infrared (FIR), submillimeter wave and millimeter wave can be detected by Bolometer. A hot electron bolometer is a device, which absorbs the incident radiation to change the electron's temperature. Its resistance will respond for it correspondingly. A traditional bolometer consists of a heat-sensitive detection element mounted inside a heat sink and physically supported by a thermally conductive physical supporter. The most common systems are helium-cooled Si, Ge and InSb bolometer. It can measure the radiation power lower in nanowatt region, but it losses the information of phase and frequency. Because of this, using bolometer to detect the power of THz radiation usually accompanies Martin-Puplett interferometer [1]. By using combined system, we can obtain the interferogram of THz radiation [2].

Using PC antenna as the detector is one of detecting THz radiation ways [3]. When the incident THz radiation illuminates the PC antenna, it induces transient current and then accelerate electron by probe beam. There are two factors determine the spectral bandwidth in this detector. One of them is the photocurrent response (i.e. carrier lifetime) and the other one is the frequency dependence of the antenna structure [4-5]. In general, the low frequency cutoff of the detectors results from the collection efficiency of the dipole, while the upper frequency limit is determined by the photocarrier response. The photocurrent response is the convolution of the optical pulse duration and the impulse current of the photoswitch across the photoconductive antenna on pulse mode.

There are two advantages of Electro-Optical (EO) sampling, one is broad bandwidth spectrum and the other is easy to implement. Recently, technique of EO sampling has become an alternative to photoconductive (PC) detection [a6]. The Zinc-Blende crystal was used to measure THz radiation based on the Pockels effect [6]. When we vary the temporal delay between pump and probe beam, the synchronous probe beam will probe the transient change of refractive index result from THz radiation changing the refractive index. There is a trade-off in this method, thick crystal will introduce longer interaction length but reduce the frequency response.

## **4-2 Power Measurement**

### **4-2-1 Bolometer**

Figure 4-1 shows the looks of our bolometer and its structure drawing including

a helium vessel. Table 4-1 shows specifications in details of the bolometer, which has a spectrum response  $100\text{cm}^{-1}$  to  $3\text{ cm}^{-1}$ .

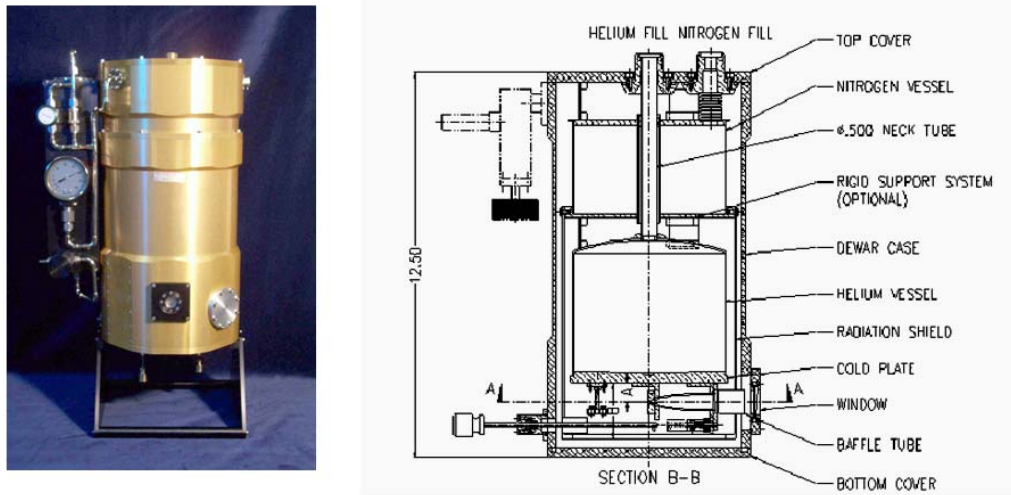


Figure 4- 1 Schematic diagram of a bolometer and its structure drawing

Table 1 Specification of the bolometer used in our measurement

Dewar	HDL-5		
Operating Temp	4.2K		
Effective cone area	0.50 " diameter		
Frequency Response	350 Hz (3db)		
Input focal ratio	3.8		
Spectral response	600 $\text{cm}^{-1}$ to 200 $\text{cm}^{-1}$	NEP.	$\sim 3.0 \times 10^{-13} \text{ w/Hz}^{1/2}$
Spectral response	375 $\text{cm}^{-1}$ to 4 $\text{cm}^{-1}$	NEP.	$\sim 2.5 \times 10^{-13} \text{ w/Hz}^{1/2}$
◆ Spectral response	100 $\text{cm}^{-1}$ to 3 $\text{cm}^{-1}$	NEP.	$\sim 1.5 \times 10^{-13} \text{ W/Hz}^{1/2}$

Before using bolometer to detect THz radiation, we need to calibrate our meter firstly. The output of the bolometer is a voltage signal; it is not directly the power of the THz radiation. We use a blackbody radiation as the thermal source to radiate electric wave for the bolometer which we need to calibrate. According to the literatures [33-34], we can get the following equation (4-1).

$$R_{\text{peak}} = \frac{V_{\text{output}}}{\frac{A_{\text{BB}} A_{\text{d}}}{R^2} F_{\text{F}} \int_{\lambda_1}^{\lambda_2} R(\lambda) \frac{M(\lambda, T)}{\pi} d\lambda} \quad (4-1)$$

Where  $\lambda_1$  and  $\lambda_2$  are the cut-on and cut-off wavelength, which we set from  $100 \mu\text{m}$  to  $3000 \mu\text{m}$ , in the response spectrum of our Si bolometer limited by the window filter.  $R_{\text{peak}}$  is the peak response in the response spectrum.  $R$  is the distance between the bolometer and the blackbody radiation source.  $A_{\text{BB}}$  and  $A_{\text{d}}$  are the area of aperture in the blackbody radiation source and the detective window of bolometer, respectively.  $R(\lambda)$  is the response spectrum of the bolometer which is assumed to have a rectangle shape due to that the response of the Si bolometer is nearly independent of the frequencies from cut-on to cut-off wavelength, although the response of the Si bolometer actually decrease with the decrease of the frequency slightly.  $V_{\text{output}}$  is the voltage value which we obtain in lock-in amplifier.  $F_{\text{F}}$  is the modulation parameter of chopper, which is about 0.5. There is the experiment setup in Figure 3.2-2. Then,  $M(\lambda, T)$  is the absolute power spectrum of the blackbody radiation source, which is the function of wavelengths and temperatures. The formula is given as following equation (3.2-2).

$$M(\lambda, T) = \frac{3.73 \times 10^4}{\lambda^5 (e^{\frac{14388}{\lambda T}} - 1)} \quad (4-2)$$

where the unit is  $\text{Wcm}^{-1}\mu\text{m}^{-1}$ . There is the experiment setup show after calibrate Bolometer, we know that the obtained response is about 50 mV per  $\mu\text{W}$  with the preamplifier gain set to 180 chopping frequency. So we can use the information of the voltage value we measure in experiment to calculate the energy



power of THz radiation. According to our calibration result, the approximate calibration factor is around  $0.1 \mu\text{W}/\text{mV}$ , which means absolute THz power in proportion to measured value of locking amplifier.

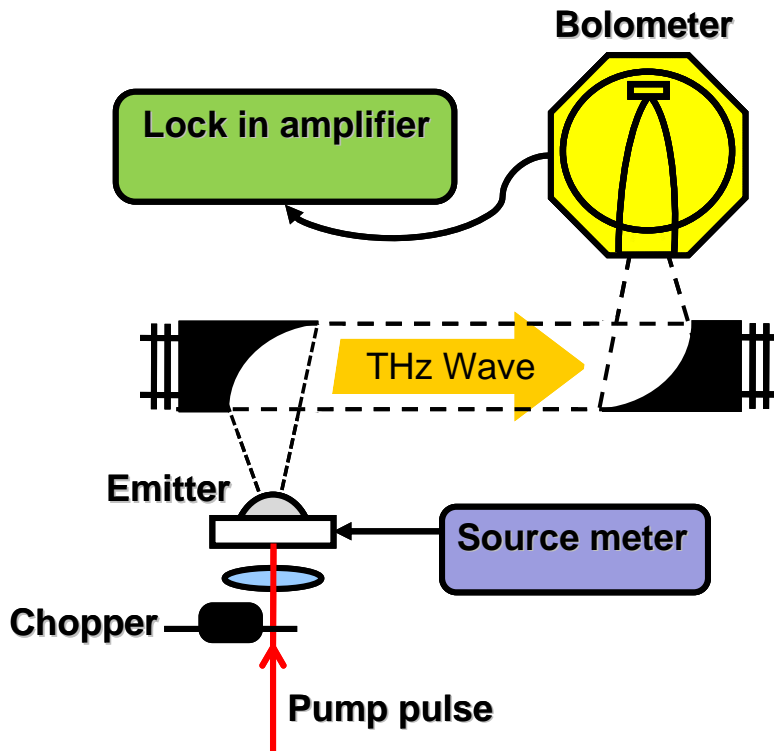


Figure 4- 2 Schematic of experiment setup for measure the electric characteristics of PC antenna.

## 4-3 Waveform of Spectrum Measurement

### 4-3-1 Martin-Puplett Polarization Interferometer

#### *Method & Setup*

The design of the Martin-Puplett polarization interferometer which is based on a concept originally produced by Martin and Puplett in 1969 resembles the

well-know Michelson interferometer, which could be used as THz FTIR. The Martin-Puplett polarization interferometer takes advantage of the polarization of electromagnetic radiation. In the field of THz frequency range, it is the most interferometer system is used. It has also been choice as the spectrometer in sub-millimeter wavelength range. Comparing the classical Michelson interferometer, it offers several advantages. Such as, the modulation efficiency of the polarizing beam splitter is higher and more uniform under wide spectral range. The simplified schematic is shown in Figure 4-3.

We use the parabolic mirror to collect THz radiation and become the parallel beam, then we incident the parallel beam into the Martin-Puplett polarization interferometer system. The spectrometer utilized two wire grid polarizes which will discuss clearly later, used also as the polarizing beam splitters. The reflected and transmitted waves in two arms of the spectrometer have equal intensities while their directions of polarization are orthogonal to each other. The retro-reflector in each arm rotates the polarization of the incident light  $180^\circ$ . The orthogonal transmitted and reflected waves are recombined at wire grid polarizer #2, then propagated through the wire-grid polarizer #1 and be collected by a parabolic mirror. By scanning the movable retro-reflector, the interferogram can be measured by the bolometer and stored by the computer.

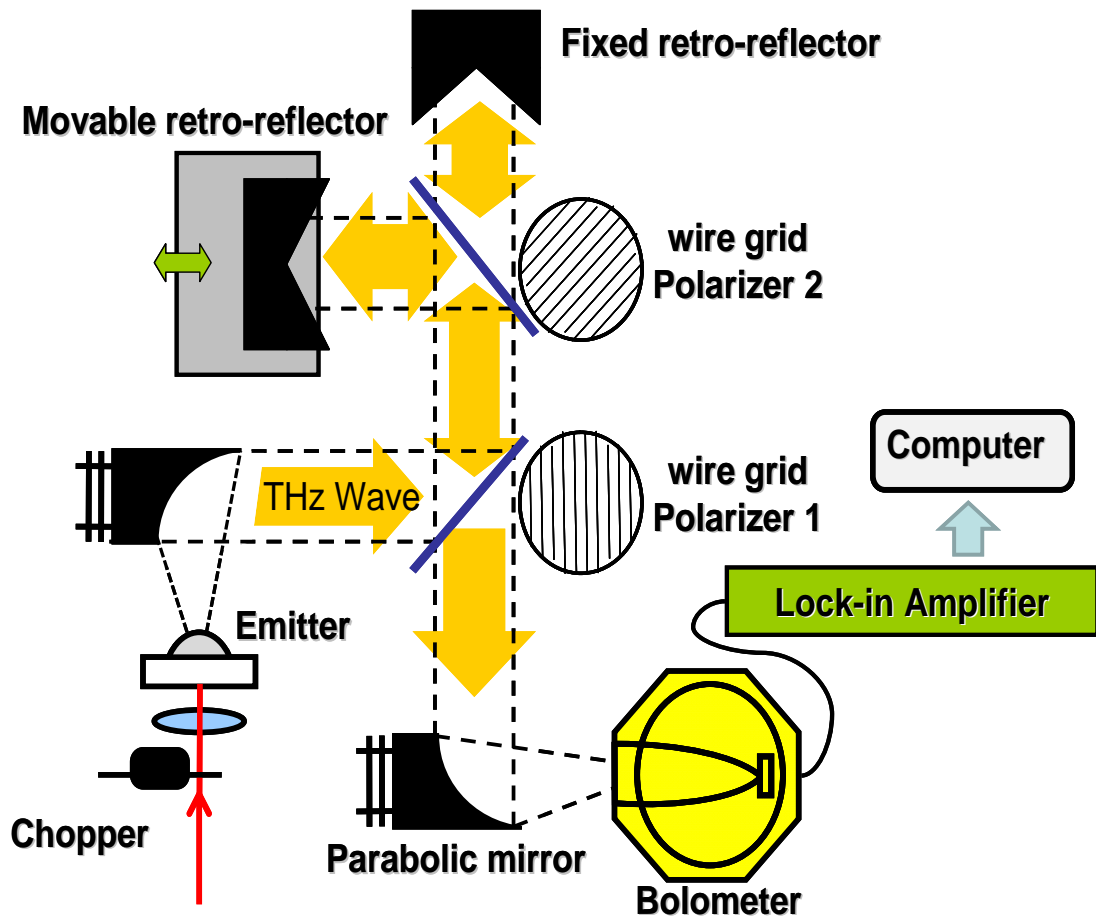


Figure 4- 3 Schematic of a Martin-Puplett-type Fourier Transform Infrared Spectrometer

(FTIR) system

### Wire grids

For far-infrared spectroscopy, an effective polarizer can be made from an array of closely spaced parallel metallic wires, and it is the so-called wire grid. When an incident electric field passes through the wire grid, it can be divided into one component parallel and one perpendicular to the wire. The parallel component induces a counteracting current in the metal and is thus reflected. In another part, the normal component can pass through pass the wire grid with a little attenuation. If the thickness  $d$  of the wires and the spacing  $s$  are small compared to the

wavelength of the incident wave, the modulus of the reflection coefficients for the electric field components parallel and perpendicular to the wires can be calculated by equation (4-3) and (4-4) [7].

$$|r_{\parallel}| = \left[ 1 + \left( \frac{2s}{\lambda} \right)^2 \ln \left( \frac{s}{\pi d} \right)^2 \right]^{-\frac{1}{2}} \quad (4-3)$$

$$|r_{\perp}| = \left[ 1 + \frac{(2\lambda s)^2}{\pi^4 d^4} \right]^{-\frac{1}{2}} \quad (4-4)$$

In our experiment setup, the wire grid we used made of  $10\mu\text{m}$  thick tungsten wire wound on a circular frame placed at a distance of  $45\mu\text{m}$ . The reflectivity of the electric field for these parameters is plotted in Figure 4-4. While the parallel component is reflected nearly perfectly over the whole spectral range, the transmission of the normal component decreases towards higher frequencies. According the experiment result, the frequency of PC antenna we measure would not be higher than 1.5THz. So we can ignore the THz power decrease from the wire grid.

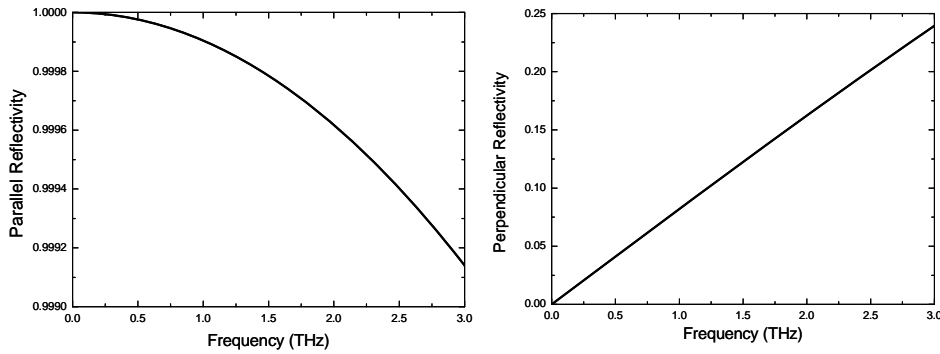


Figure 4- 4 The reflectivity of the electric field dependent with frequency under (a) parallel and (b) perpendicular component.

### 4-3-2 THz Time Domain Spectrometer

The THz time-domain spectroscopy system is shown in Figure 4-5. The incident pump pulse was focused by an objective lens on the biased gap of the PC antenna to generate THz radiation. The THz radiation was collimated and focused by a pair of off-axis parabolic mirror on a PC sampling detector. Which was also a PC antenna mounted on the back of a Si hemispherical lens. The PC detector was gated by femto-second probe beam pulses that were separated from the pump beam pulses by a beam splitter, and the DC photocurrent was induced by the incident electric field of THz radiation on the PC detector.

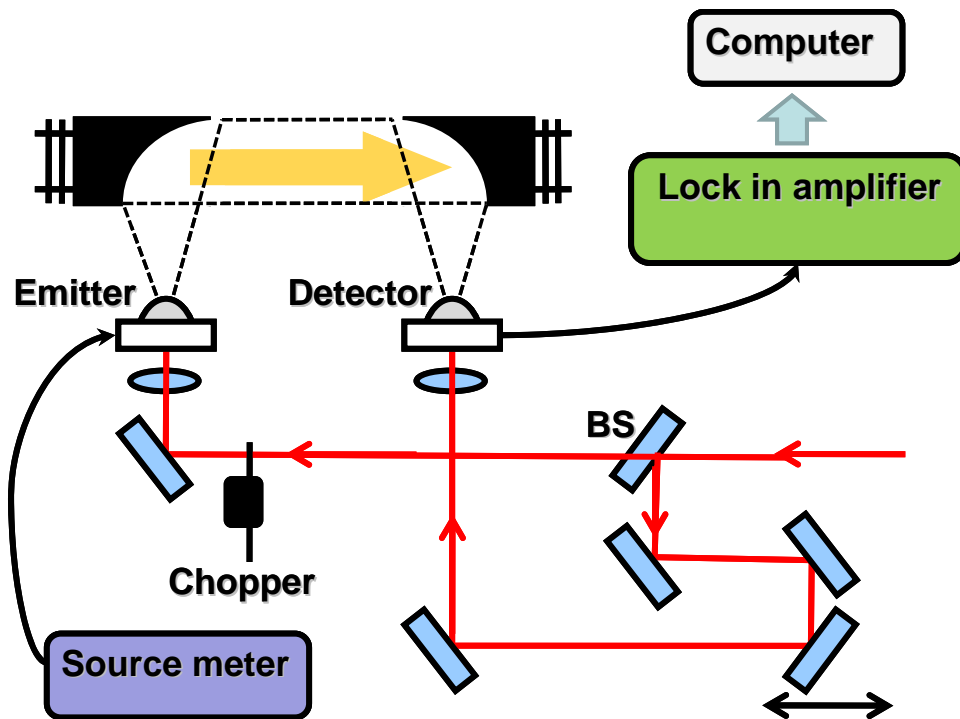
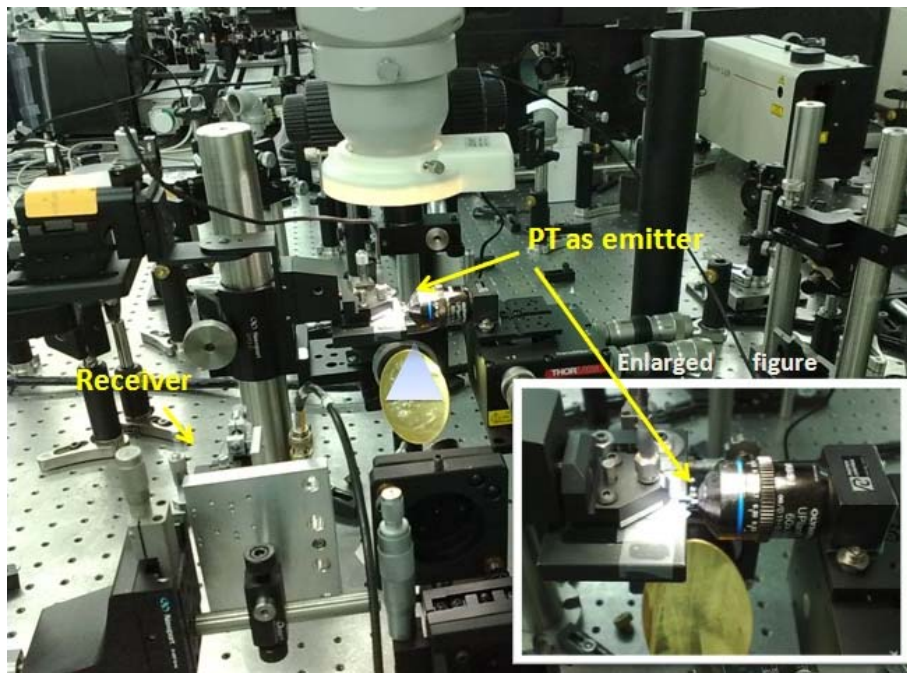


Figure 4- 5 Terahertz Time-Domain Spectroscopy

Using delaying the time of the probe pulse to the pump pulse, the time-domain

waveform of the electromagnetic pulse was obtained. The time resolution was limited by the carrier lifetime of the LT-GaAs used for the PC detector. To increase the signal-to-noise ratio, the pump beam was modulated with a mechanical chopper at 1 KHz, and output signal from the PC detector was measured with a lock-in amplifier and stored by the computer.



*Figure 4- 6 A picture of measured photonic transmitter in a TDS system*

## Reference

- [1] D. H. Martin, and E. Puppelt, “polarized interferometric spectrometry for the millimeter and submillimeter spectrum” *Infrared Physics*, Vol.10, pp. 105-109, 1969.
- [2] O. Morikawa, M. Tonouchi, and M. Hangyo, “sub-THz spectroscopic system using a multimode laser diode and photoconductive antenna” *Appl. Phys. Lett.*, Vol.75, No. 24, pp. 3772-3774, 1999.
- [3] S. kono, M. Tani and K. Sakai, “Coherent Detection of mid-infrared radiation up to 60THz with an LT-GaAs photoconductive antenna” *IEE, Proc-optoelectron*, Vol.149, No. 3, pp. 105-109, 2002.
- [4] Sang-Gyu Park, Michael R. Melloch, and Andrew M. Weiner, “Analysis of Terahertz Waveforms Measured by Photoconductive and electrooptic sampling” *IEEE J. Quantum Electronics*. Vol.35, No. 5, pp. 810-819, 1999.
- [5] S Kono, Masahiko Tani, and Kiyomi Sakai, “Ultrabroadband photoconductive detection: comparison with free space electro optic sampling” *Appl. Phys. Lett.*, Vol.79, No. 7, pp. 898-900, 2001.
- [6] Sang-Gyu Park, M. R. Melloch, and A. M. Weiner, “Comparison photoconductive sampling” *Appl. Phys Lett.*, Vol.73, pp. 3184-3186, 1998.
- [7] J. C. G. Lesurf. “Millimetre-wave optics, devices and systems.” Adam Hilger, January, 1990.

# Chapter 5 Performances of THz and

## Sub-THz Emitters

In this chapter, the measurement result of PC antennas and photonic transmitters are shown and discussed. First, in chapter 5-1 and 5-2, we studied the LTG-GaAs and GaAs:O based PC antennas under pulse and CW excitation respectively. An comparable performance of GaAs:O to serve as substituted material of LTG-GaAs is demonstrated. After that, in chapter 5-3, we discussed the performance of STR-PD combined with slot antenna with a center frequency 500GHz. Such results show our high power and high speed STR-PD could be served as an important part of high power sub-THz emitter. Finally, in the end of this chapter, we further to study in detail the characterization of two high-power photonic transmitters based on two different kinds of high-power photodiodes UTC-PD and STR-PD. Such result help us to learn a fabrication of high power and high speed sub-THz emitter.

### 5-1 LTG-GaAs & GaAs :O PC Antennas under Pulse Excitation

*Figure 5-1* shows the bias voltage dependence of the THz absolute intensity generated from different material with the laser beam focused near its anode with the same antenna structure. They were detected by the bolometer. According the *Figure 5-1*, we can observe that the THz power increases quadratically with the bias at higher bias voltage. GaAs:O has higher photocurrent than LT-GaAs, and GaAs:O



has high power when we biased higher than 60V. The THz peak power of GaAs:O is 5.2mW and LT-GaAs is 3.6mW when biasing at 80V and pumping with 30mW.

GaAs:O generate pulse THz power almost 1.4 times LT-GaAs.

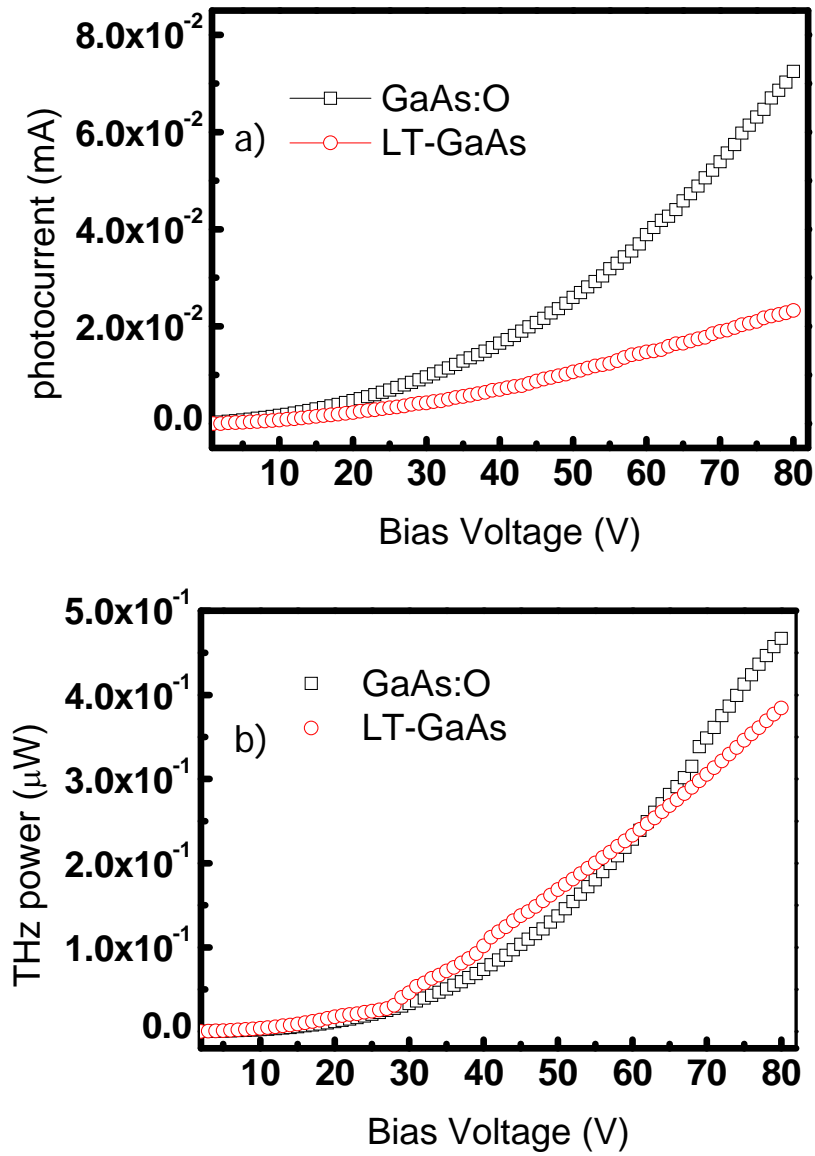


Figure 5- 1(a) Photocurrent-bias (b)THz power-bias curve of GaAs:O and LT-GaAs antenna with the same antenna structure

The increasing ratio of THz power-bias voltage curve of GaAs:O are higher than LT-GaAs, although LT-GaAs has higher THz power at lower bias voltage. And there is no saturation effect in both materials under pulse laser pumping. We used TDS to characterize the GaAs:O and LT-GaAs antenna. Figure 5-2 shows that THz wave form of GaAs:O and LT-GaAs. The measurements are under different bias voltage (20V、40V、60V、80V) and pump power is fixed at 30mW.

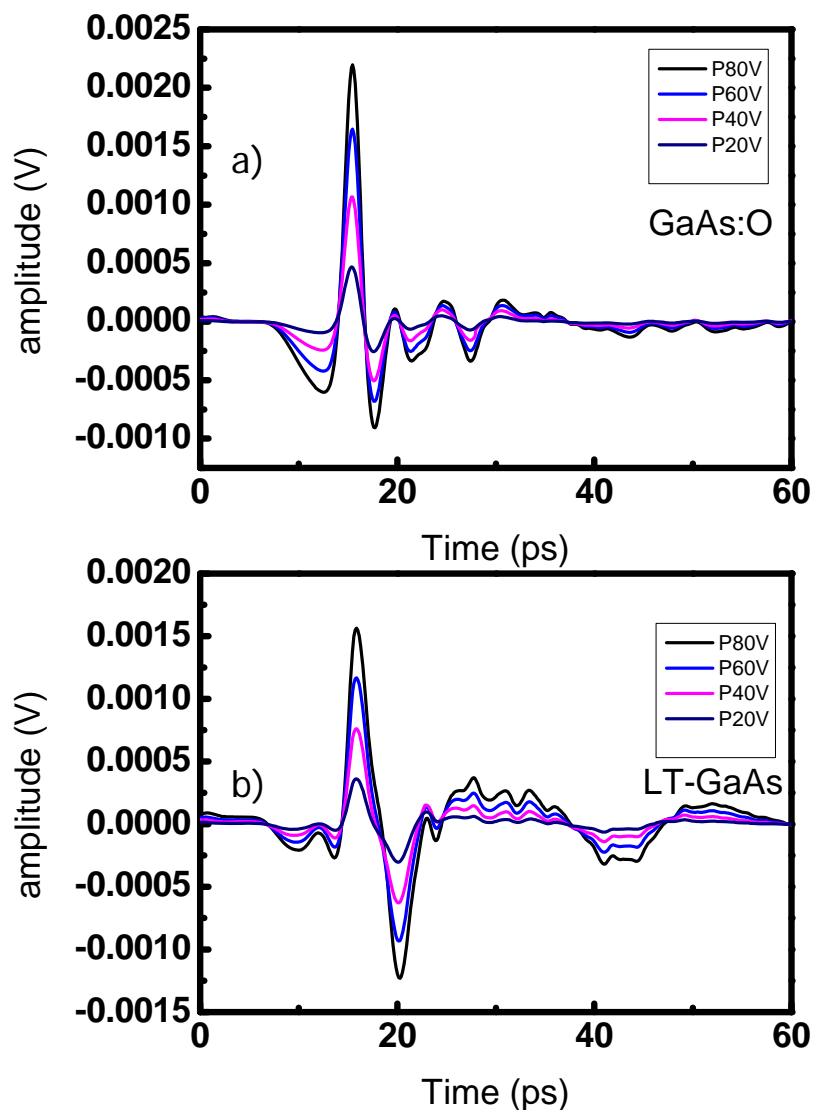


Figure 5- 2 THz time domain waveform of (a) GaAs:O and (b) LT-GaAs at constant pump power 30mW

The THz spectra under different biases are shown in figure 5-3. We observed that the THz peak amplitude increases when bias increases, However, we can't observe any spectral shift, and this also matches with previous literature[24].

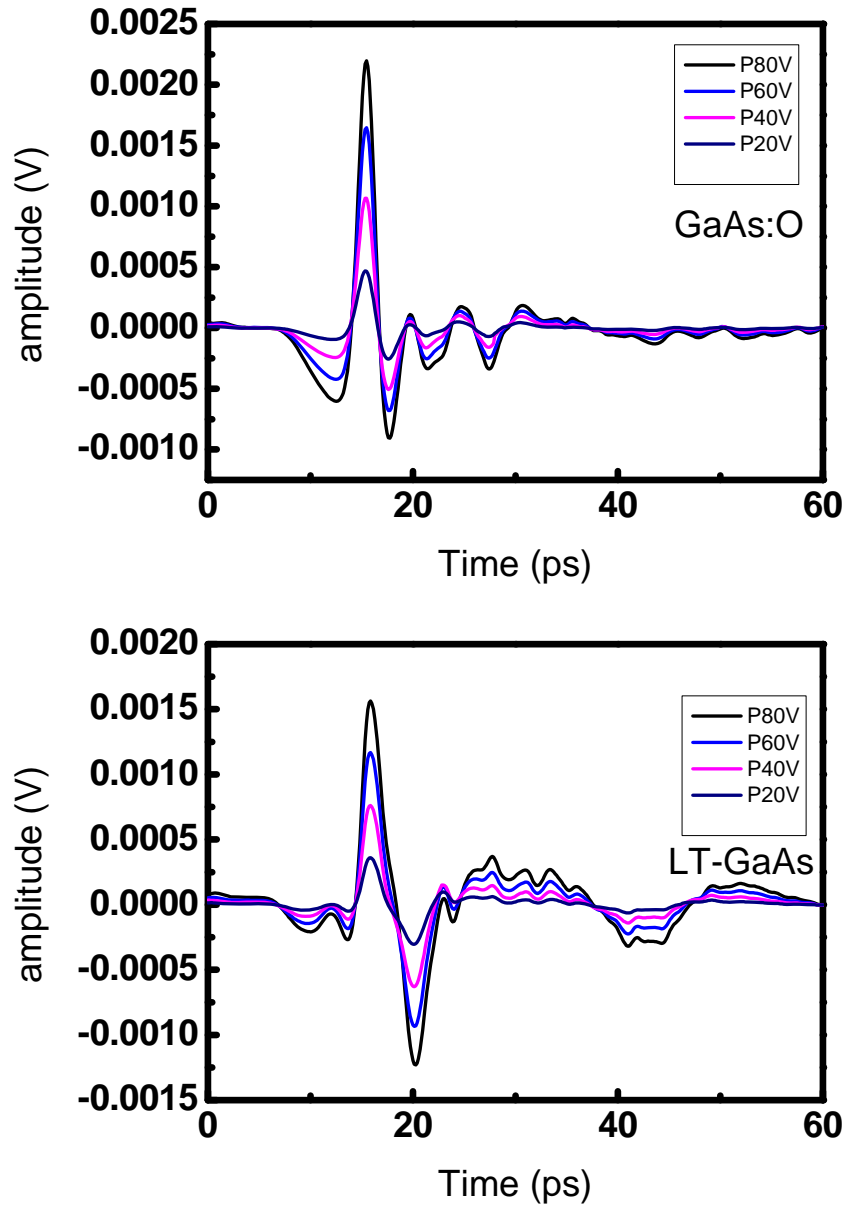


Figure 5- 3 THz spectrum of (a) GaAs:O and (b) LT-GaAs at constant pump power 30mW

Figure 5-4 (a) show that the main peak amplitude of GaAs:O is higher than LT-GaAs under pump 30mW and bias 80V in pulse mode. And we observed both spectra are about 1THz.

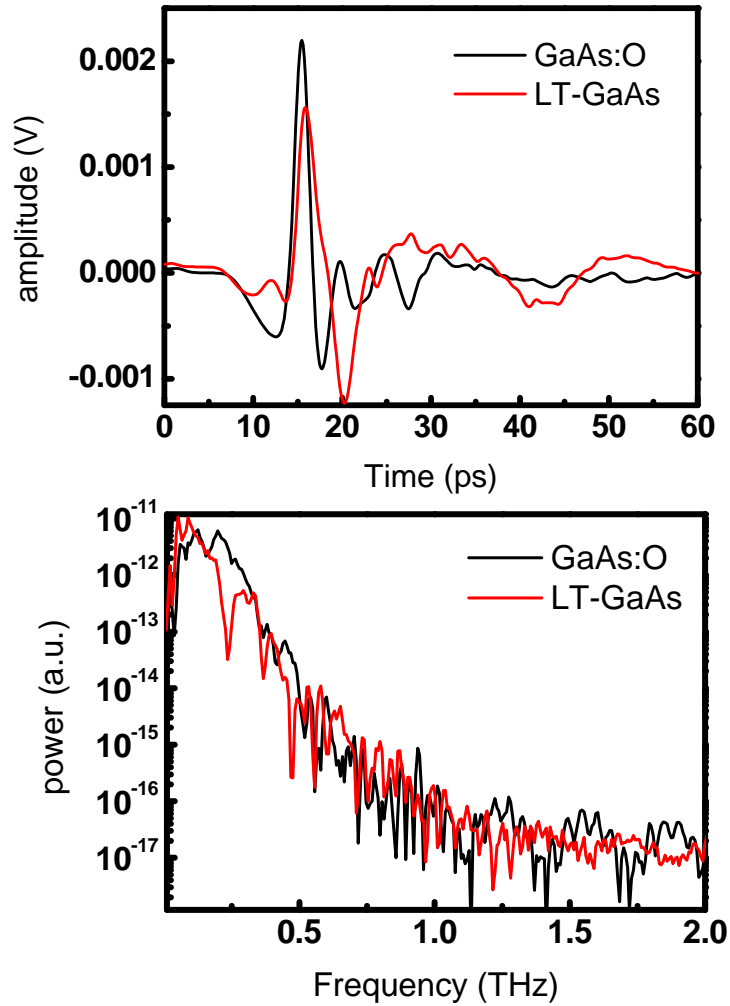
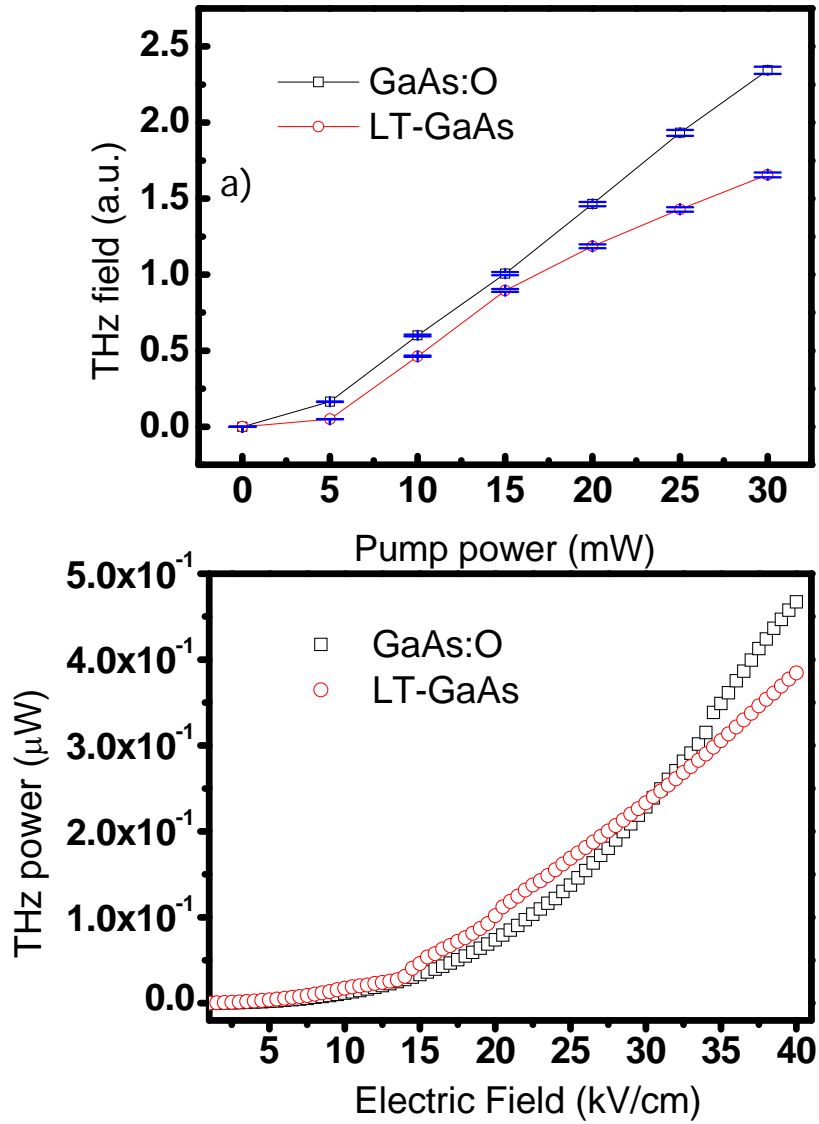


Figure 5- 4 (a) Time domain waveform (b) Spectrum for both materials

Figure 5-5 (a) shows the pump power dependence of the THz intensity measured for our PC antennas using a constant bias voltage of 80V. Figure 5-5 (b) shows the bias voltage dependence of the THz intensity measured for our PC antennas using a constant pump power of 30mW. Due to the low pump power, we

can not observe the strong saturation effect in *Figure 5-5 (a)* in pulse mode. Because the pump power doesn't excite enough carriers to form reverse electric field. And also we can't observe the saturation effect in *Figure 5-5 (b)* due to the low electric field.



*Figure 5- 5 (a) The amplitude-pump power curve at bias voltage 80V (b) The THz power-electric field curve at 30mW.*

## 5-2 LTGaAs & GaAs :O PC Antennas under CW Excitation

Figure 5-6 shows the bias voltage dependence of the photocurrent and the THz absolute intensity generated from different materials with the two laser beams focused near its anode with the same antenna structure.

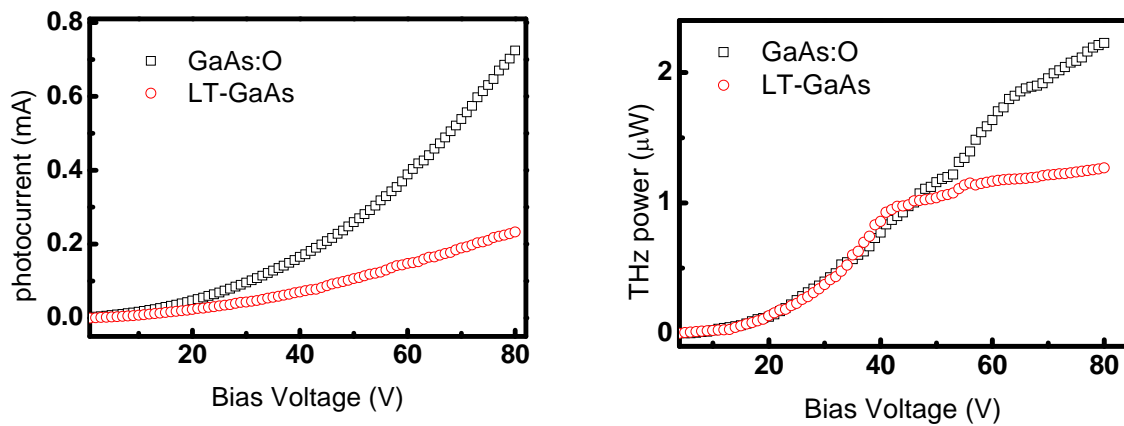


Figure 5- 6 (a) Photocurrent-bias voltage curve and (b) THz power-bias voltage curve of GaAs:O and LT-GaAs fabricated with the same dipole antenna

They are also detected by the bolometer. According the Figure 5-6, we can obtain that the THz power are almost the same for both materials when bias is smaller than 40V, the highest THz power of GaAs:O is  $2.268\mu\text{W}$  and LT-GaAs is  $1.27\mu\text{W}$ . GaAs:O has almost 1.8 times to LT-GaAs and there is no saturation effect in high bias voltage. However we observe THz power saturation effect in low temperature grown GaAs [1].

### *Analysis and Discussion*

Figure 5-7 shows the bias voltage dependence of the photocurrent measured for our photoconductive antennas using a constant pump power of 180mW which are 90mW for each other. According to the result, we observe that the photocurrent ratio of GaAs:O divide to LT-GaAs are increasing when bias is more than 20V, The bias voltage below 20V are not increasing due to non-uniform electric field and low signal-noise ratio. And according to the CW theory, the carrier density is proportional the carrier lifetime ( $n \propto \tau_e$ ), electron drift velocity is proportional the mobility at low electric field ( $v \propto \mu_e$ ) and DC photocurrent is proportional to the carrier lifetime multiple mobility ( $I_{ph}^{DC} = e\tau_e\mu_e$ ), so the mobility of GaAs:O is between 2.5 and 3.75 times to LT-GaAs.

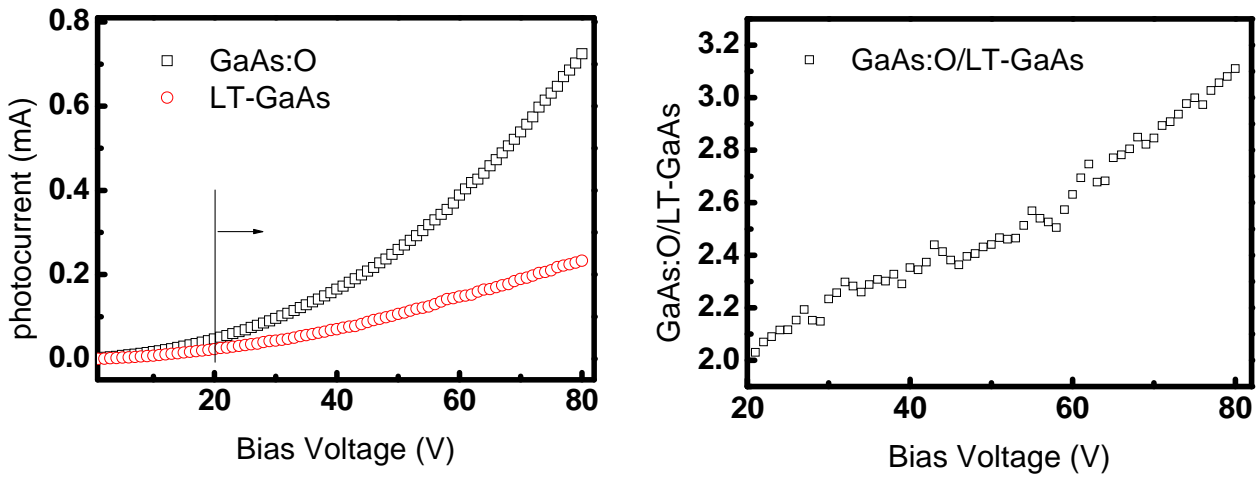


Figure 5- 7 (a) Photocurrent-bias voltage curve of both materials and (b) photocurrent ratio of GaAs:O divide to LT-GaAs

Figure 5-7 (a) (b) (c) (d) show the DC photocurrent-electric field curve of GaAs:N GaAs:O and LT-GaAs. We observe the increase of onset voltage for

quadratic behavior in the I-V curve corresponds to a consistent reduction of saturation in the P-I curve [1]. It means that the efficient of generation THz power with the same photocurrent are different when we implant different dosage density, due to different number of impact ion defects. The absence of additional very large defects (precipitates) which reduce the electron mobility may deteriorate the increase of carrier lifetime with voltage.

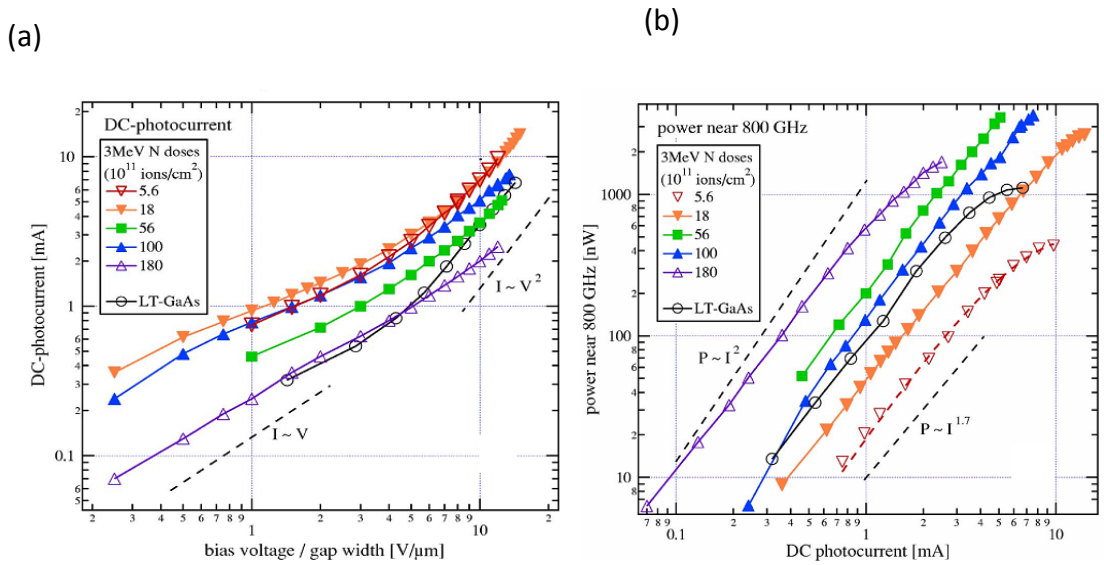


Figure 5- 8 (a) Different dosage density of GaAs:N and LT-GaAs (b) Different dosage density of GaAs:N and LT-GaAs[48]

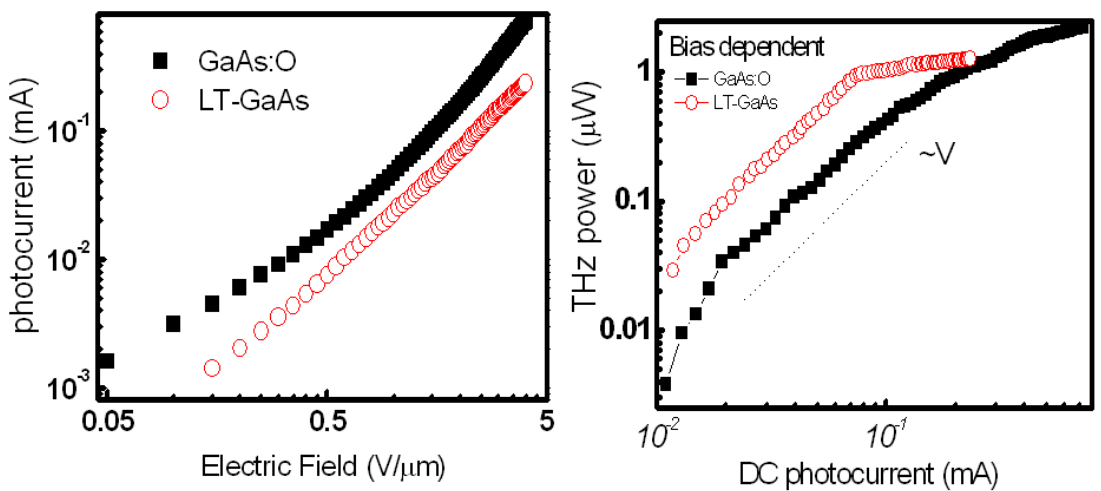


Figure 5- 9 photocurrent-electric field curve and THz power-DC photocurrent curve for

GaAs:O and LT-GaAs DC



In figure 5-9, we observe that THz power of LT-GaAs is saturated by the pump power. The reason of the LT-GaAs saturation is due to radiation field screening. Note that at low optical intensities the values of THz power is linear with optical pump that is the inverse of photoconductance and is greater than load impedance, when the optical intensities increase, the inverse of photoconductance has the same order to load impedance, THz power would respond nonlinear with optical pump power. But we didn't observe saturated effect occurred at GaAs:O, we attribute to higher conductivity compared to LT-GaAs

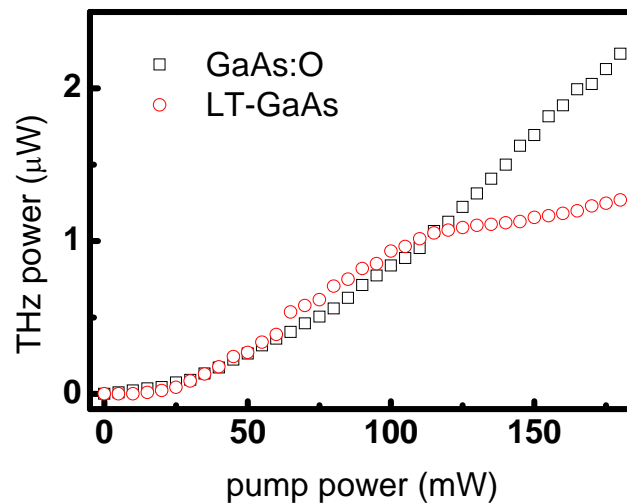


Figure 5- 10 CW THz power-optical pump power for both materials.

In figure 5-10 (a) we observe that photocurrent are super-linear behavior on both materials. The reason that photocurrent has quadratic increasing is due to carrier life time increasing with voltage and that would increase the photoconductance and, consequently, the photocurrent. And under radiation field screening and carrier life time increasing we observe that GaAs:O has slightly saturated. Other effects such as impact ionization may play a role as well.

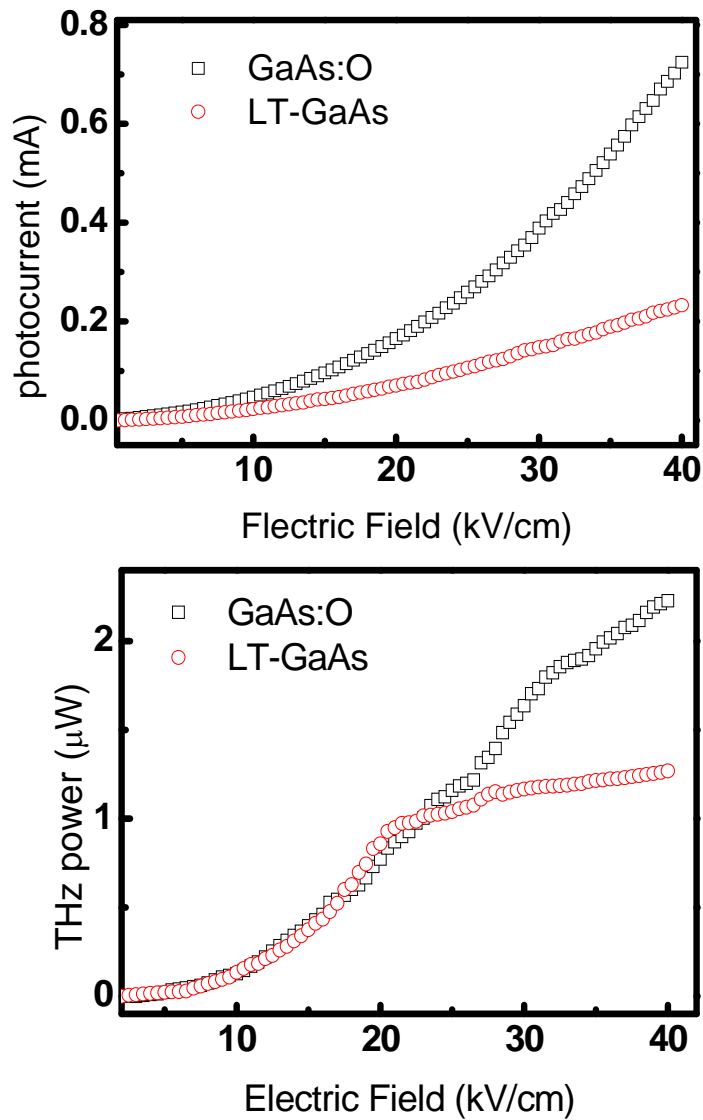


Figure 5- 11 (a) Photocurrent-electric field curve and (b) THz power-electric field curve.

In figure 5-11 show that the spectrum of GaAs:O and LT-GaAs measured by CW heterodyne system. We calculate the resonant frequency the theory value is 0.34THz and our measurement value is 0.36THz. The bandwidth of both materials is about 1THz. They are identical to the value that we measured by THz-TDS system.

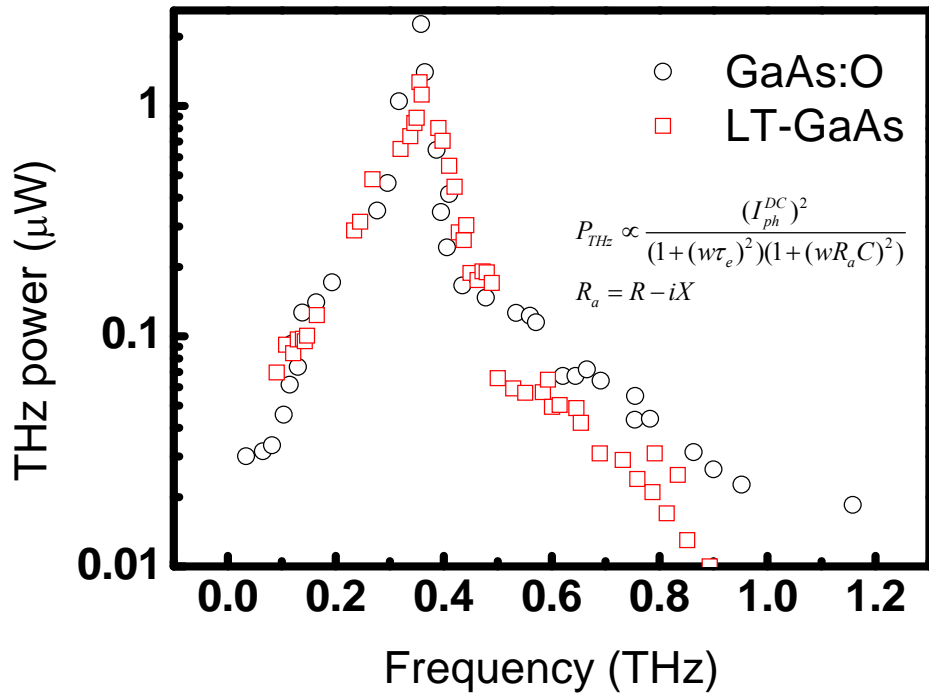


Figure 5- 12 THz spectrum of both materials measured by CW heterodyne system

### 5-3 STR-PD Combined with Slot Antennas

We directly excited our device by use of a femto-second Ti:sapphire ( $\lambda = 800\text{nm}$ ) mode-locked laser to measure the radiated impulse responses of our transmitter. The excitation optical plus, which has the 82MHz repetition rate and 100fs pulse width, was focused by an objective on the input facets of our device. We used two parabolic mirrors to collimate and focus the radiated THz pulse on a liquid-helium-cooled Si bolometer for power measurement. The responsivity of the Si bolometer was calibrated with a blackbody radiation source. We also measured and calibrated the radiated THz beam propagation loss in air by measuring the THz intensity as a function of propagation distance. The propagation loss was about  $0.082\text{ cm}^{-1}$ . The RF spectra and waveforms of radiated signal were measured by a Martin-Puplett-type Fourier Transform Infrared Spectrometer (FTIR) with the same Bolometer as in power measurement. The FTIR system is consisted of two wire grid polarizers, the first one is used as reflector at the input port of system and the second one act as a beam splitter. By scanning the movable retro-reflector, the interference spectrum (waveform) of the input sub-THz wave in the time domain could be obtained. The frequency responses of radiated signal can thus be obtained through the use of Fourier-transform techniques. The measured interference patterns and corresponding transformed spectra of devices with a  $23\ \mu\text{m}$  and a  $60\ \mu\text{m}$  active lengths are shown in *Figure 5-12(a) and (b)* and their insets, respectively. Both devices exhibit significant resonance at around 100GHz and 200GHz frequency, and a significant resonance at the designed resonant frequency ( $\sim 500\text{GHz}$ ) of slots antenna has only been observed for the device with a short active length, as shown in (a).

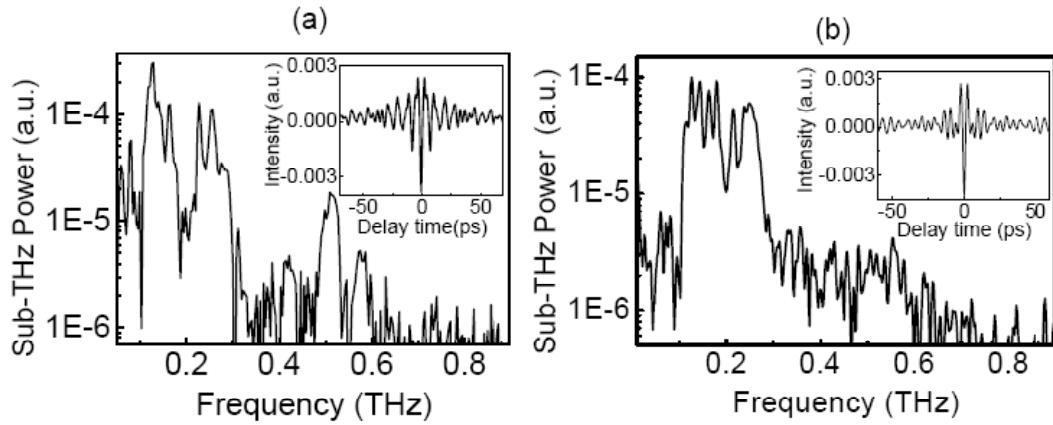


Figure 5- 13 The Fourier-transformed spectra of our photonic-transmitters with different active lengths,  $23\mu\text{m}$  (a) and  $60\mu\text{m}$  (b).

(The insets show the original interfere spectrum in the time domain measured by using the FTIR system)

For the device with a long active length, it should have a poorer speed performance and lower output power in the high frequency regime than a short device. A much less apparent resonance at the designed frequency ( $\sim 500\text{GHz}$ ) of long device has thus been observed. The parasitic oscillations in  $0.1\sim 0.2\text{ THz}$  frequency regime may be attributed to the influence of integrated photodiode, which has not been included in our antenna design.

Figure 5-13 shows the measured sub-THz power versus injected optical power under different reverse bias voltages of devices with a  $23\mu\text{m}$  active length. Under  $\sim 30\text{mW}$  average optical power excitation, as much as  $5\mu\text{W}$  of sub-THz power was measured, which has been calibrated for around  $4.3\text{dB}$  propagation loss after  $12\text{cm}$  propagation. Besides, the output sub-THz power shows a near parabolic relation between the injected optical powers when it's value is below  $10\text{mW}$ .

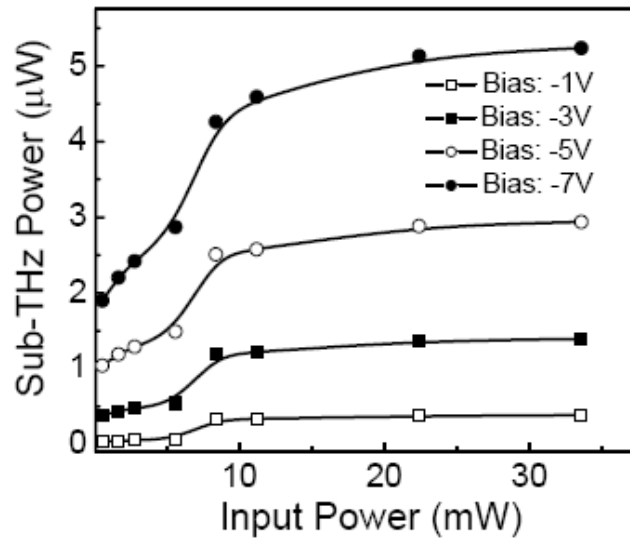


Figure 5- 14 The measured sub-THz intensity vs. optical pumping power under different reverse bias voltages

On the other hand, when the optical power is over such value, saturation phenomenon of sub-THz power has clearly been observed. The saturation phenomenon of output sub-THz power under high optical power excitation may be attributed to the high photocarrier density resulted defect saturation in the LTG-GaAs active layer, thus that carrier lifetime will increase and lead the bandwidth degradation.

The measured bias-dependent sub-THz power of device with a 23 $\mu$ m active length under different optical pumping power is shown in *Figure 5-14*. The inset shows the measured photocurrent versus dc reverse bias under different optical pumping power. The maximum reverse bias voltage (-7V) is limited by the device failure. Regarding with the reported LTG-GaAs based photodetectors and photomixers [3,4,5], they usually suffered from serious bandwidth degradation and the saturation of radiated THz power under high reverse bias voltage and high external applied electric field (>50kV/cm) due to the lifetime increasing effect of

LTG-GaAs [3,6].

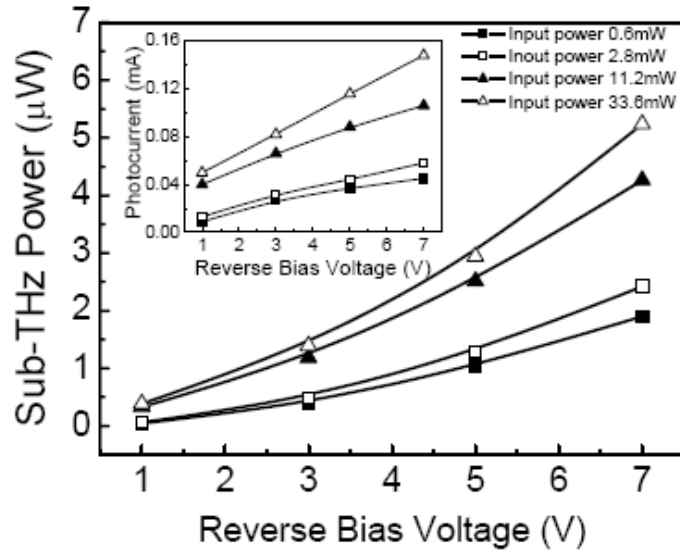


Figure 5- 15 The measured sub-THz intensity vs. reverse bias voltages under different optical pumping power for our photonic-transmitters with a  $23\mu\text{m}$  active length.

(The inset shows the measured output photocurrent vs. reverse bias voltages under different optical pumping power.)

However, for our devices even under a highest reverse bias ( $-7\text{V}$ ), corresponding to an external applied electric field up to  $200\text{kV/cm}$  in the active region, saturation phenomenon of radiated power has not been observed. Furthermore, the output sub-THz power has an ideally quadric relation between reverse bias voltages due to that the output photocurrent is linear proportional to reverse bias voltage, as shown in the inset. The superior bias dependent performance of our transmitter to traditional LTG-GaAs based photomixer is because that, for our STR-PD, the external applied electric field is concentrated in the two high quality GaAs transport layers instead of LTG-GaAs based recombination center [7] and the lifetime increasing effect of LTG-GaAs layer under high electric field ( $>50\text{kV/cm}$ ) can thus be neglected [6].

## 5-4 Comparison of UTC-PT and STR-PT

During device testing, an objective lens with a high numerical aperture (NA) value is used to focus the output of the fs Ti:Sapphire mode-locked laser ( $\lambda=800\text{nm}$ ) onto the edge of our devices. The excitation optical pulse has a repetition rate of 82 MHz and a pulse width of 100fs. Figures 3 (a) and (b) show the bias current versus voltage (I-V) of the two devices under different input powers. The active lengths of the measured UTC-PD and STR-PD based PTs (UTC-PT and STR-PT) is the same, around  $23\ \mu\text{m}$ .

As can be seen in *Figure 3*, the average photocurrent generated by the UTC-PT is much higher than that of the STR-PT, even under lower bias and input pulse energy. This can be attributed to the presence of the LT-GaAs based recombination center inside the STR-PD active layers, which effectively traps the photo-generated carriers and degrades the external quantum efficiency of the device. The generated photocurrent of the UTC-PT increases super-linearly with the reverse bias voltage when it is over 5V. This phenomenon can be attributed to the fact that the value of the external applied electrical field ( $3.6\times 10^5\text{V/cm}$ ) in the  $\text{Al}_{0.12}\text{Ga}_{0.88}\text{As}$ -based collector layer is close to its breakdown field.

A super-linear increase of photocurrent vs. reverse bias voltage has also been observed for the LTG-GaAs based PD [6], which can be attributed to the lifetime increasing effect of LTG-GaAs layer is much less apparent for our STR-PD, perhaps because most of the external electric field is concentrated in the two high quality GaAs transport layers instead of the LTG-GaAs based recombination center, which has a high defect density and field-screening effect under reverse bias voltages



[8]. The lifetime increasing effect can thus be neglected. In addition, the avalanche induced photocurrent in the transport layers is not as significant as the case shown in (a), which may be attributed to the fact that most of the avalanche-generated carriers are also trapped by the recombination centers.

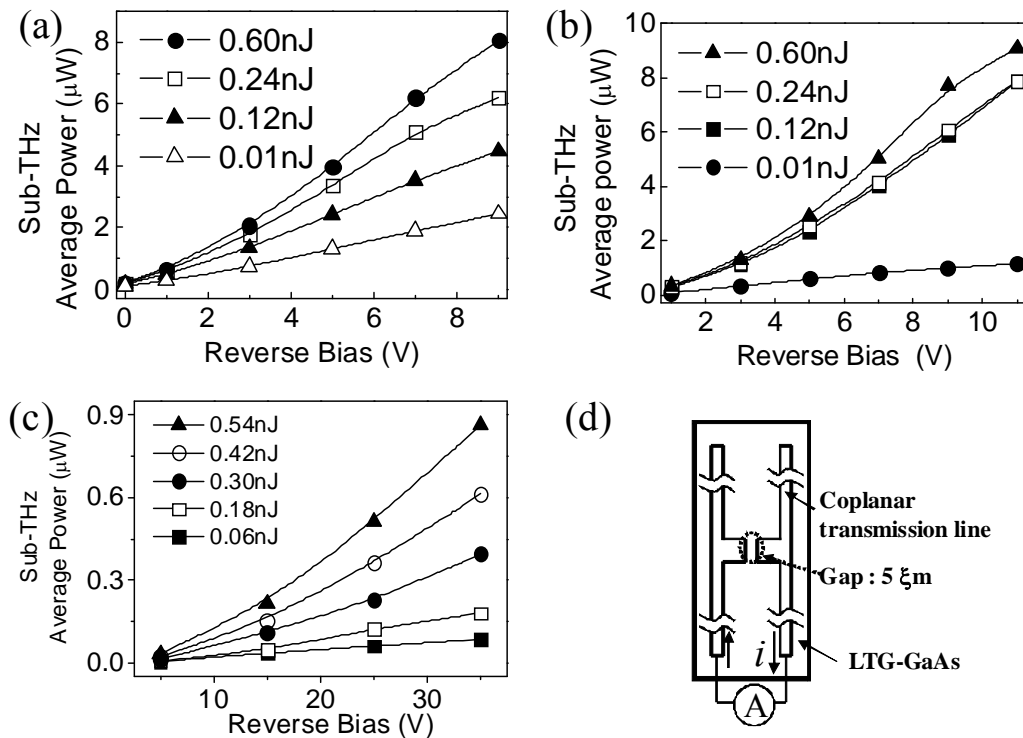


Figure 5-16 The bias dependent measured sub-THz power of (a) UTC-PT, (b) STR-PT, and (c) LTG-GaAs based PC under different optical pulse energy excitation. (d) shows the top-view of PC dipole antenna

The total output power of the two devices was measured by a liquid-Helium cooled Si bolometer, which was carefully calibrated to the black body source. Two parabolic mirrors were used to collimate and focus the generated sub-THz into the bolometer. The propagation loss ( $0.082 \text{ cm}^{-1}$ ) is also calibrated by measuring the THz intensity as a function of the propagation distance at a relative humidity of 40%.

Figures 5-15 (a) and (b) show plots of the sub-THz power of UTC-PT and STR-PT emitted under different optical pumping pulse energies as a function of the bias voltage. As much as  $8 \mu\text{W}$  and  $9 \mu\text{W}$  of maximum sub-THz average power are measured for the STR - and UTC-PT respectively. We can clearly see that although the maximum average photocurrent of the UTC-PT is around four times higher than that of the STR-PT, as shown in Figure 5-15, the maximum average sub-THz power generated by the STR-PT is similar to that of the UTC-PT under a lower excitation optical pulse energy (0.12nJ vs. 0.48nJ). This result indicates that the recombination center in the STR-PD has eliminated most of the DC component of the photocurrent, so the AC component of the optical pulses can be efficiently converted to an electrical AC signal and then radiated into free-space. The STR-PD requires less operation current for the desired radiated power performance which implies that the thermal effect can be minimized during high-power operation.

In addition, as shown in figure 5-15 (a), when the reverse bias of UTC-PD is less than about -5V, the radiated sub-THz power exhibits an ideal quadratic relation to the reverse bias voltage. This is due to the linear dependence of the output photocurrent on the reverse bias voltage ( $<-5\text{V}$ ), as shown in Fig. 5-14(a). When the reverse bias voltage increases further, however, the output sub-THz power exhibits a linear dependence on the bias voltage. This can be attributed to the fact that the value of the external applied electrical field ( $\sim 3.6 \times 10^5 \text{ V/cm}$ ) in the  $\text{Al}_{0.12}\text{Ga}_{0.88}\text{As}$  based collector layer is close to its breakdown field. Thus the avalanche-induced bandwidth degradation phenomenon of the PD limits the super-linear increase of output power versus the bias.

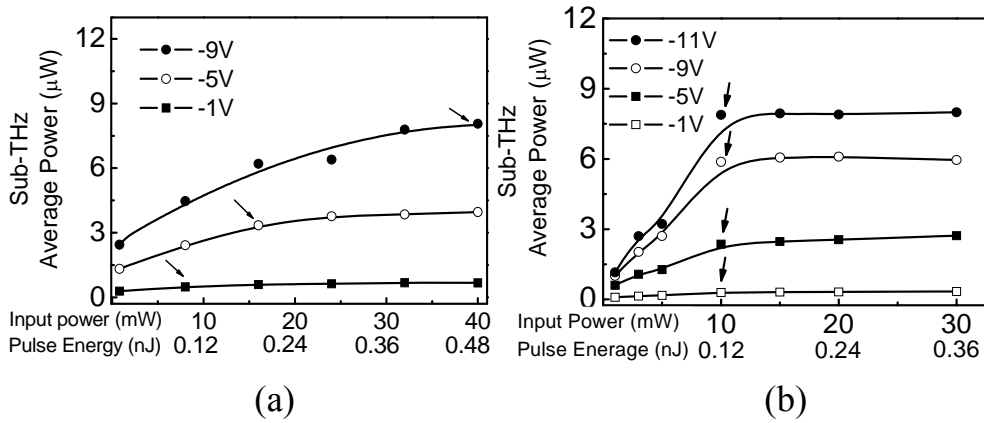


Figure 5- 17 The power dependent measured sub-THz power of (a) UTC-PT and (b) STR-PT under different reverse bias voltage.

As can be seen in Figure 5-14 (a), the measured photocurrent clearly increases super-linearly with the bias voltage when it is over -5V. This indicates that the avalanche phenomenon really does occur. The bias dependent output power of STR-PT shows similar behavior to the measured bias dependent photocurrent, as shown in Figure 5-14(b). When the injected pulse energy increases from 0.01nJ to 0.12nJ, the emitted sub-THz power dramatically increases due to the huge increase of photocurrent; see Figure 5-14 (b). However, when the pulse energy exceeds 0.12nJ, the traces under higher injected pulse energy are crowded due to the phenomenon of recombination center saturation, which will be discussed latter in Figure 5-16.

Figure 5-15 (c) shows the measured bias dependent output sub-THz power from a typical photoconductive (PC) dipole antenna, which is fabricated on the LTG-GaAs layer [9] and mounted on the Si-lens. Such PT has a center frequency at 260GHz with around 1THz bandwidth. The measured values of power are close to those reported for an LTG-PC with an antenna of the same design [9]. Figure 5-15 (d) shows the top-view and geometric size of such device. We can clearly see that both of our

devices can have around 10 times higher output sub-THz power than such LTG-GaAs based traditional PT by use of a much lower reverse bias voltage ( $\sim 10\text{V}$  vs.  $35\text{V}$ ).

Figure 5-16 (a) and (b) shows the measured optical power dependent output sub-THz power under different reverse bias voltage of UTC-PT and STR-PT, respectively. As can be seen, the value of the saturated injected optical pulse energy of the UTC-PT (indicated by arrows in Figure 5-16(a)) increases with the reverse bias voltage. The observed saturation phenomenon of the UTC-PD should be attributed to the electron induced SCS effect in the collector layer [9], which can be minimized by increasing the reverse DC bias voltage [9,10]. On the other hand, the power dependent saturation behavior of the STR-PD is very different from that of the UTC-PD (indicated by the arrows in Figure 5-16(b)).

We can clearly see that the saturation of the optical pulse energy is the same around  $0.12\text{nJ}$  regardless of an increase in the reverse bias voltage. This phenomenon may be attributed to that fact that the dominant saturation mechanism in the STR-PD is the defect saturation of the LTG-GaAs based recombination center, rather than the SCS effect when the effective depletion (transport) layer is as thin as  $50\text{nm}$ . The external applied reverse bias voltage is concentrated in the transport layers and thus has no influence on the saturation point of the recombination centers. The results of the optical simulation show that the coupling efficiency between the injected beam (beam diameter of around  $2\mu\text{m}$ ) and the active waveguide of the STR-PD is around 30%. We can thus roughly estimate that the photo-generated carrier density under  $0.12\text{nJ}$  pulse energy excitation is as high as  $\sim 1 \times 10^{19}\text{cm}^{-3}$ . This value is close to the reported defect density of the LTG-GaAs material [10].

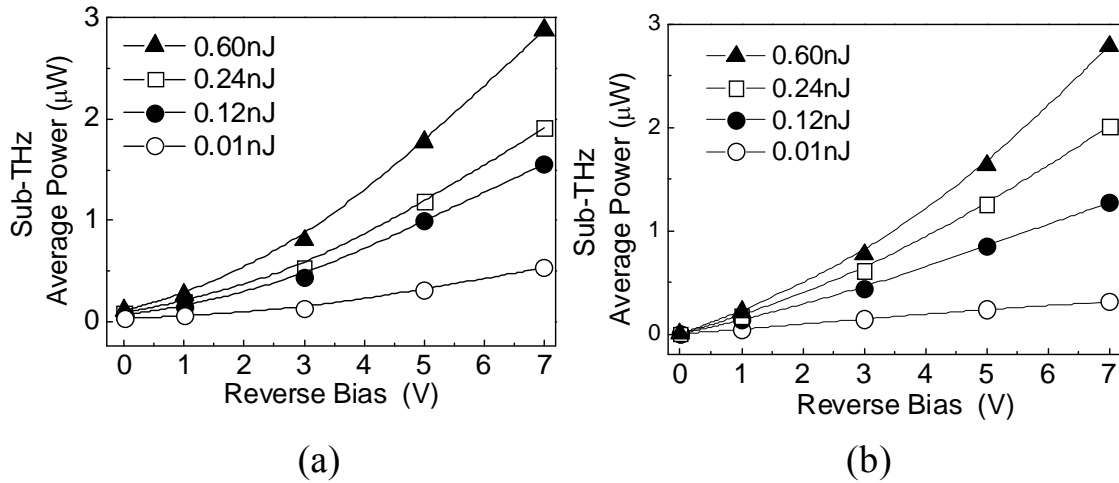


Figure 5- 18 Bias-dependent sub-THz power of (a) UTC-PT and (b) STR-PT with a longer active length of  $60 \mu\text{m}$  under different injected optical pulse energy

Figures 5-17(a) and (b) show plots of the bias dependent emitted sub-THz power of UTC-PT and STR-PT with the same and a longer active length ( $\sim 60 \mu\text{m}$ ) than that of the measured devices ( $\sim 20 \mu\text{m}$ ). The measurement results are shown in *Figures 5-16* for reference. We can clearly see that due to the longer active lengths and poor RC-limited bandwidth, both devices exhibit less than one-half of the maximum output power than that shown in *Figure 5-17* under the same reverse bias voltage and input pulse energy.

We utilized a THz-TDS system [11] to investigate the waveform of the radiated sub-THz impulse that could be applied to the IR communication system. The same mode-locked Ti: sapphire laser was used to pump both devices. The injected optical pulse energy was  $480\text{pJ/pulse}$ . A photo-conductive (PC) dipole antenna, as shown in *Figure 5-15* (d), fabricated on a LTG-GaAs layer and integrated with a Si-lens is used to probing the radiated signal. The direction of the dipole antenna was adjusted

parallel to the direction of the polarization of the radiated sub-THz pulses. With identical PC antenna as the emitter and receiver, our THz-TDS system exhibits a bandwidth exceeding 1THz and a signal-to-noise ratio better than 1000.

Figure 5-18 (a) and (b) shows the measured waveforms of the radiated sub-THz pulses of UTC-PT and STR-PT under the same reverse bias voltage (-9V), respectively. The corresponding Fast-Fourier-Transform (FFT) spectra of UTC-PT and STR-PT are shown in Figures 5-19 (a). The measured waveform and corresponding FFT spectrum of adopted LTG-GaAs PC antenna is shown in (b) for reference.

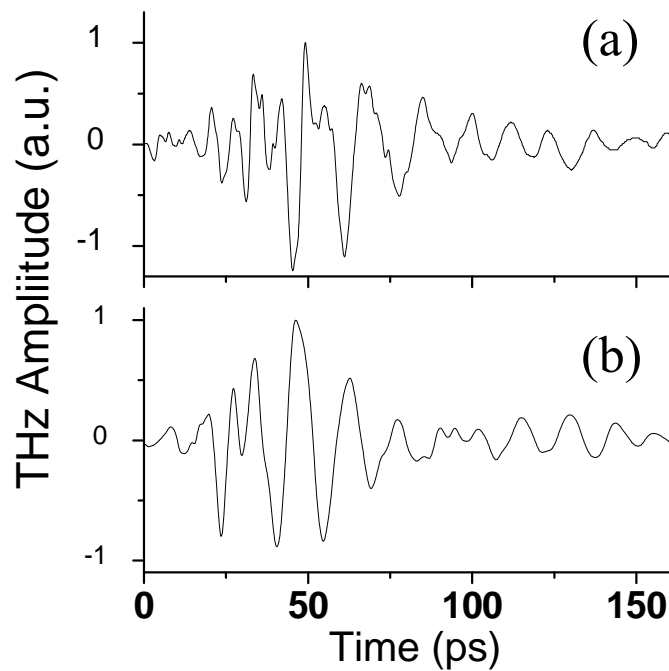


*Figure 5- 19 The radiated waveform of sub-THz pulses for UTC-PT (a) and STR-PT (b).*

As can be seen in Figure 5-18, the shapes of the measured pulses in the time domain are similar for STR-PT and UTC-PT. The measured traces show a fast

oscillation period with a slow-varying envelope, which has an envelope with of around 100ps. The full-width-half-maximums (FWHMs) of the main peaks of the oscillating waveforms are around 3.9ps and 4.4ps for UTC-PT and STR-PT, respectively.

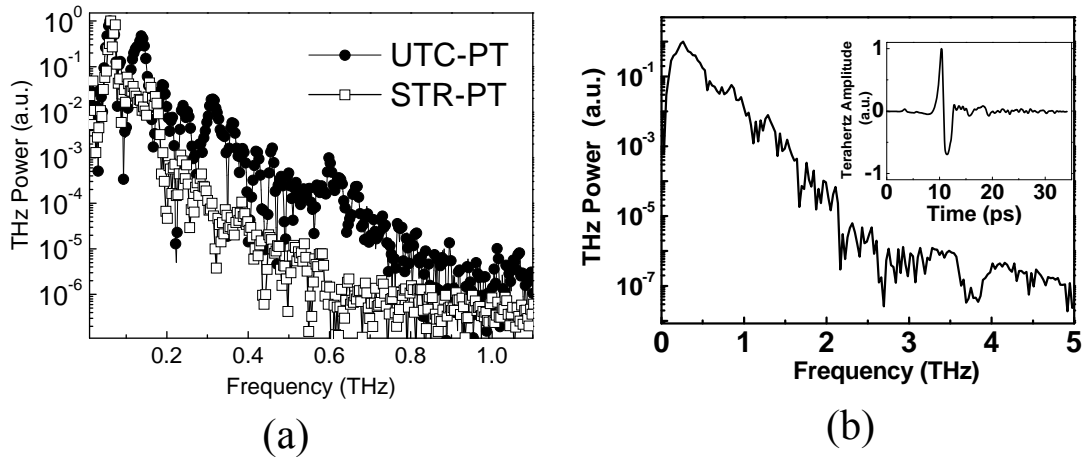


Figure 5- 20 The normalized power spectrum of (a) UTC-PT, STR-PT and (b) LTG-GaAs based PC antenna. The inset shows the measured waveform of PC antenna

As shown in Figure 5-19(a), the bandwidth of both devices cover from near DC to around 250GHz. We defined the bandwidth of device as its THz power drops to around  $10^{-2}$ , as shown in the y-axis of Figure 5-19(a). Furthermore, STR-PT, exhibits a more serious high-frequency ( $>200$ GHz) roll-off than does the other, UTC-PT, which indicates that the speed performance of integrated UTC-PD may be better than that of the STR-PD. More detailed experiments are necessary and will be performed in future to accurately extract the optical-to-electrical (OE) 3-dB bandwidth of the two devices.

Table 2 The list of measurement results of UTC-PT and STR-PT

	UTC-PT	STR-PT
Envelope FWHM	47.2ps	57.0ps
FWHM of main pulse	3.9ps	4.4ps
Max average power	8 $\mu$ W	9 $\mu$ W
Peak power	9.2mW	7.8mW
Experimental Bandwidth	250GHz	200GHz

The measured bandwidths of both devices are somewhat smaller but comparable to that obtained in the simulation result (100GHz to 350GHz) of the antenna. The bandwidth limitation may be attributed to the serious high-frequency roll-off of the active devices when the operating frequency exceeds 300GHz. The observed ringing (oscillation) is consistent with the simulation result, and can be attributed to the influence of the integrated antenna on the radiated impulse response. As a first approximation, the photo-generated electrical pulse from the UTC-PD can be considered to be Gaussian in shape. It exhibits a frequency response from the DC to hundreds of GHz. However, the integrated antenna functions like a “filter”, in the sense that it passes (radiates) a specific band of frequencies associated with the multi-resonance feature of the antenna structure. Hence, the frequency components outside the operating band of the antenna are suppressed in the radiated field, which leads to the ringing of the measured pulse. Observed ringing can also be attributed to multiple reflections between the substrate-removed antenna and chip boundaries, where the GaAs substrate has not been removed with a microwave probe. Similar



phenomena have been reported for InP UTC-PD based photonic transmitters and explained by the same mechanism [12].

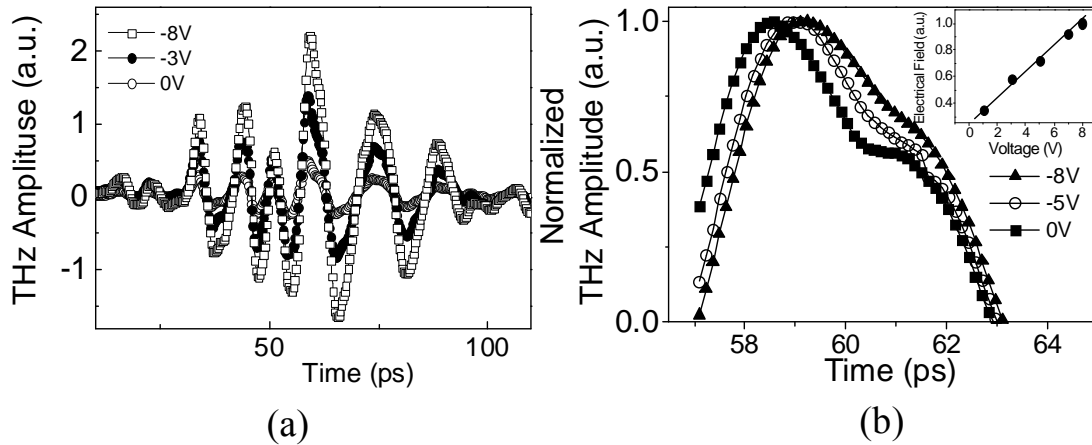


Figure 5- 21 Bias dependent waveforms of the radiated sub-THz pulses for (a) UTC-PT and (b) the normalized and enlarged main peak. The inset shows the normalized peak values versus reverse bias.

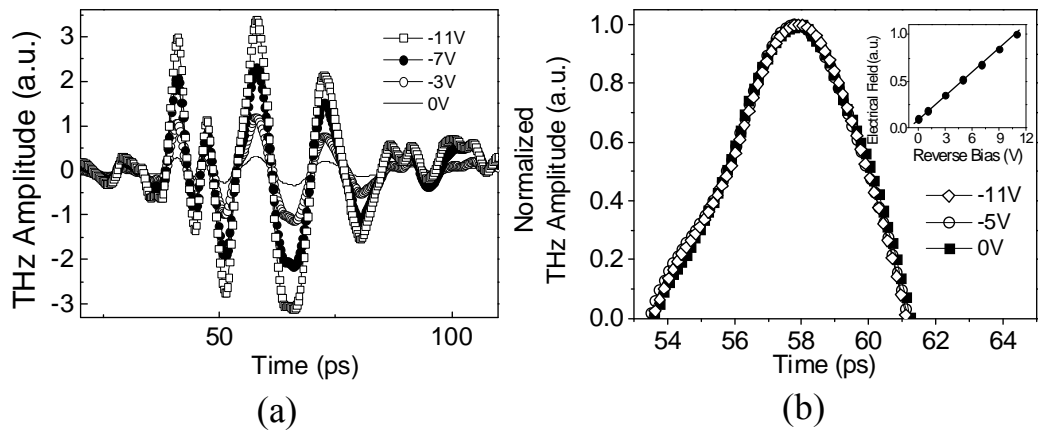


Figure 5- 22 Bias dependent waveforms of the radiated sub-THz pulses for (a) STR-PT (b) and the normalized and enlarged main peak. The inset shows the normalized peak values versus reverse bias.

Using the average measured power and pulse shapes, we can roughly estimate the peak-power of both devices. They are calculated by the integrated ratio of the area

of squared THz amplitude in time domain. The measured and calculation results are summarized in detail in Table 2. We can clearly see that the STR-PT has a comparable radiated peak-power ( $\sim 9.2\text{mW}$ ), and FFT bandwidth ( $\sim 250\text{GHz}$ ) under a much lower operation current than does the UTC-PT. By using the bias modulation technique, a photonic transmitter could serve as a sub-THz emitter and data modulator [12,13]. As a result, we measure the bias dependent sub-THz waveforms of both devices in detail using the same THz-TDS system.

Figures 5-20 (a) and 5-21 (a) show the measured waveforms for the UCT-PT and STR-PT under different reverse bias voltages and fixed optical pumping pulse energy ( $\sim 480\text{pJ/pulse}$ ). Figures 5-20 (b) and 5-21 (b) show the normalized main peak pulses for (a). We can clearly see that both devices exhibit excellent linearity, which means that the shape of the measured waveforms remain unchanged from zero-bias to high bias operation, even under high peak-power output ( $\sim 7.8\text{mW}$ ) [14]. Figure 5-20 shows the case for UTC-PT, where the bias voltage sweeps from 0 to 8 V, and the peak-electrical field increases about five times (0.5 to 2.4). The results for the STR-PT are shown in Figure 10. Its peak-electrical field increases about 11 times (0.3 to 3.4) as the bias voltage sweeps from 0 to 11V. These measurements results are an indication of the potential of these two devices to serve as sub-THz emitters and data modulators, using the bias modulation technique [12,13] with much lower driving voltages than that of the traditional PC-antenna [15].

## Reference

- [1] E. A. Michael, I. Camara Mayorga, and R. Gusten, "Terahertz continuous-wave large-area traveling-wave photomixers on high-energy low-dose ion-implanted GaAs", *Appl. Phys. Lett.* **90**, 171109, 2007.
- [2] K.-G. Gan, J.-W. Shi, Y.-H. Chen, C.-K. Sun, Y.-J. Chiu, and J. E. Bowers, "Ultrahigh power-bandwidth-product performance of low-temperature-grown GaAs based metal–semiconductor–metal traveling-wave photodetectors," *Appl. Phys. Lett.*, vol. 80, pp. 4054-4056, May, 2002.
- [3] M.-C. Tien, H.-H. Chang, J.-Y. Lu, L.-J. Chen, S.-Y. Chen, R.-B. Wu, W.-S. Liu, J.-I. Chyi, and C.-K. Sun, "Device saturation behavior of submillimeter-wave membrane photonic transmitters," *IEEE Photon. Technol. Lett.*, vol. 16, pp. 873-875, March, 2004.
- [4] S. Verghese, K. A. McIntosh, and E. R. Brown, "Highly tunable fiber-coupled photomixers with coherent terahertz output power", *IEEE Trans. Microwave Theory Tech.*, vol. 45, pp. 1301-1309, Aug., 1997.
- [5] S. M. Duffy, S. Verghese, K. A. McIntosh, A. Jackson, A. C. Gossard, and S. Matsuura, "Accurate modeling of dual dipole and slot elements used with photomixers for coherent terahertz output power," *IEEE Trans. Microwave Theory Tech.*, vol. 49, pp. 1032-1038, June, 2001.
- [6] N. Zamdmer, Qing Hu, K. A. McIntosh, and S. Verghese, "Increase in Response Time of Low-Temperature-Grown GaAs Photoconductive Switches at High Voltage Bias" *Appl. Phys. Lett.*, vol. 75, pp. 2313-2315, Oct., 1999.
- [7] S. Verghese, K. A. McIntosh, and E. R. Brown, "Highly tunable fiber-coupled

- photomixers with coherent terahertz output power”, *IEEE Trans. Microwave Theory Tech.*, vol. 45, pp. 1301-1309, Aug., 1997.
- [8] J.-W. Shi, H.-C. Hsu, F.-H. Huang, W.-S. Liu, J.-I. Chyi, Ja-Yu Lu, Chi-Kuang Sun, and Ci-Liang Pan, “Separated-Transport-Recombination p-i-n Photodiode for High-speed and High-power Performance” *IEEE Photon. Technol. Lett.*, vol. 17, pp. 1722-1724, Aug., 2005.
- [9] H. Ito, S. Kodama, Y. Muramoto, T. Furuta, T. Nagatsuma, T. Ishibashi, “High-Speed and High-Output InP-InGaAs Unitraveling-Carrier Photodiodes,” *IEEE J. of Sel. Topics in Quantum Electronics*, vol. 10, pp. 709-727, Jul./Aug., 2004.
- [10] J. P. Ibbetson and U. K. Mishra, “Space-charge-limited currents in nonstoichiometric GaAs,” *Appl. Phys. Lett.*, vol. 68, pp. 3781–3783, 1996.
- [11] T. -A. Liu, G. -R. Lin, Y.-C. Chang, C.-L. Pan, “Wireless audio and burst communication link with directly modulated THz photoconductive antenna,” *Optic. Express*, vol.13, Issue 25, pp. 10416-10423, Dec., 2005.
- [12] A. Hirata, T. Furuta, H. Ito, and T. Nagatsuma, “10-Gb/s millimeterwave signal generation using photodiode bias modulation,” *J. Lightw. Technol.*, vol. 24, no. 4, pp. 1725–1731, Apr. 2006.
- [13] Y.-S. Wu, Nan-Wei Chen, and J.-W. Shi, “A W-Band Photonic Transmitter/Mixer Based on High-Power Near-Ballistic Uni-Traveling-Carrier Photodiode (NBUTC-PD),” *IEEE Photon. Technol. Lett.*, vol. 20, pp. 1799-1801, Nov., 2008.
- [14] E. Ivanov, S. Diddams, and L. Hollberg, “Study of the Excess Noise Associated with Demodulation of Ultra-Short Infrared Pulses,” *IEEE Trans. on Ultrasonics, Ferroelectrics, and Frequency Control*, 1068-1074 , 2005.
- [15] T. -A. Liu, G. -R. Lin, Y.-C. Chang, C.-L. Pan, “Wireless audio and burst

communication link with directly modulated THz photoconductive antenna,”  
Optic. Express, vol.13, Issue 25, pp. 10416-10423, Dec., 2005.

# Chapter 6 Sub-THz Impulse Radio

## Communication

### 6-1 Introduction

The great demand for new high bandwidth services is beginning to drive the deployment of fiber access networks around the world. However, in some areas, it may be too costly to deploy optical fiber, hence; high data rate wireless communication is a good solution. Ultra-wideband (UWB) system is traditionally considered as impulse radio [1], using very narrow pulses for data communications, wherein each transmitted pulse occupies the whole UWB bandwidth. This is a carrierless system, transmitting in a way such that it does not interfere largely with other traditional “narrow band” and continuous (CW) wave carrier used in the same frequency band. However, the Federal Communications Commission (FCC) and International Telecommunication Union (ITU) now define UWB as the emitted signal with bandwidth exceeding the lesser of 500 MHz or 20% of the center frequency. This means, for example, orthogonal frequency division multiplexing (OFDM) signal can be considered UWB under these regulations. Because of this, we will use the term UWB-impulse radio (UWB-IR) to distinguish it from other UWB technologies in this work.

The repetition rate of the pulses in UWB-IR system may be low for pulse-based radars and imaging systems. On the other hand, we can use high repetition rate UWB-IR for communication systems. Due to the ultra-short pulses used in the

UWB-IR system, the signal pulses can be readily distinguished from the unwanted multipath reflections in time domain. Consequently, multipath fading can be easily filtered or ignored. Hence the UWB-IR has the benefits of relative immunity to multipath fading [2]. The large bandwidth of the UWB-IR system enables high data rates (Gb/s), particularly for short-range indoor applications [2]. Besides, the UWB-IR transmitters (Tx) and receivers (Rx) usually do not require expensive and complicated components, such as modulators, demodulators, and intermediate-frequency (IF) stages. This can reduce the cost, size, and power consumption of the UWB-IR systems when compared with conventional narrowband communication systems. Previous studies primarily focused on the multipath immunity of the UWB-IR systems [2, 3].

Nonetheless, atmospheric turbulence will lead to a time-varying fading in the received signal, which can introduce significant amplitude fluctuations and greatly limit the transmission distance and reliability of the UWB-IR system. In this work, we propose and demonstrate through numerically analysis that Manchester coding can improve the transmission fidelity of the UWB-IR system. A specific example of UWB-IR system, Terahertz (THz) communication system will be used in this analysis. Using sub-picosecond optical-pulse-triggered photoconductive antennas, electromagnetic pulses with center frequency of sub-THz (~200-300 GHz) and nearly unity fractional bandwidth can be generated and received. Wireless communication systems up to millimeter wave band have been reported [4-8]. A wireless audio THz communication link using impulse radio has been experimentally demonstrated recently by our group [9].

Here, we demonstrate sub-THz communication link by using photonic transmitters and PC antenna as emitters respectively, and measure frequency response

of system, which provide us important previous work for future application. After that, we analyze the feasibility of using Manchester coding to improve the THz transmission. Numerical analysis comparing both conventional on-off-keying (OOK) and Manchester coded transmissions shows that Manchester coding can provide significant improvement in the presence atmospheric turbulence effects.

## **6-2 Frequency Response of Communication Link System**

### **◆ *Spiral antenna on LTG-GaAs PC antenna based TDS system for Sub-THz communication link***

In figure 6-1, the system of spiral antenna on LTG-GaAs PC antenna based TDS system for Sub-THz communication link is shown. Two spiral antenna printed on LTG-GaAs PC antennas are adopted as emitter and receiver in the TDS system. The inset of figure 6-1 shows its time domain electrical field form and power spectrum. The lower center frequency around 50 GHz and 200 GHz of noise floor is measured, which may provide us higher transmission power compared with LTG-GaAs based dipole antenna.

By using AO modulator, we can modulate generated sub-THz by modulating excitation input pulse laser. The measured frequency response of the system is shown in figure 6-2 while applied voltage on emitter is around 10 Vp-p. The excitation input power is around 20 mW after AO modulator and such power is under proper operation condition and photo current. The frequency response of the communication link by AO modulator is around 2 MHz, which is enough for video communication link.



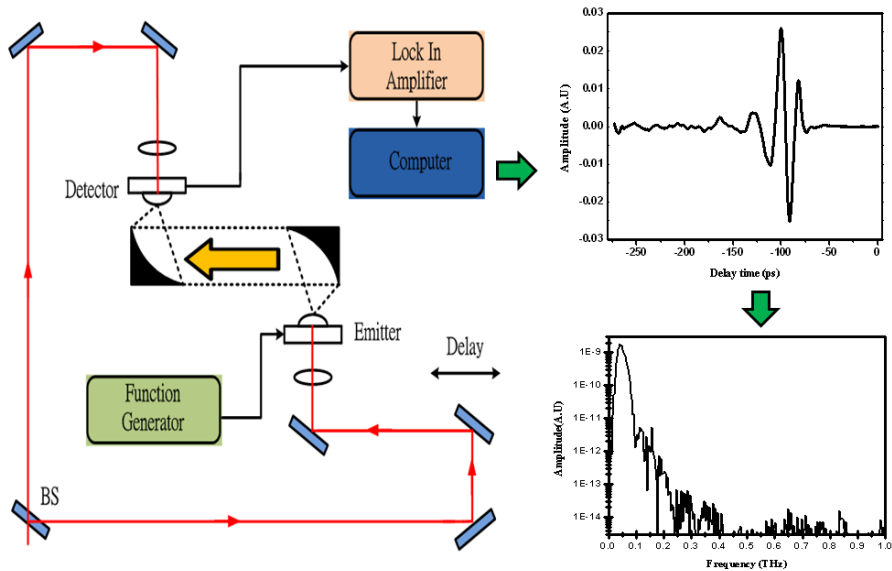


Figure 6- 1 Schematic diagram of spiral antenna on LTG-GaAs PC antenna based TDS system for Sub-THz communication link

However, the main frequency response limitation is come from receiver we used—PC antennas, which has poor frequency response. As a result, the measured 3-dB frequency response in this system is several kHz, which is similar to our previous work. Around -20 dB received signal is measured while modulated frequency is around 50 kHz. We also demonstrate the video transmission by

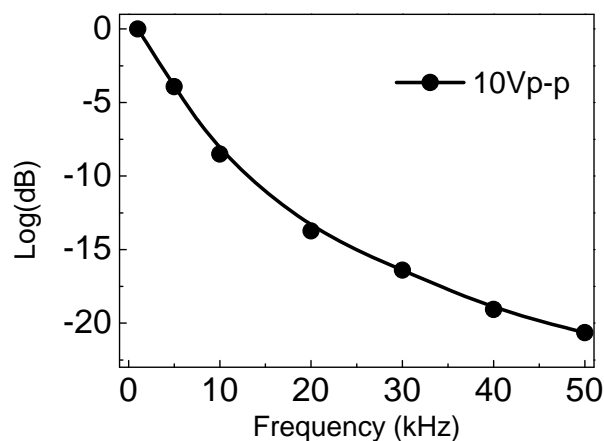


Figure 6- 2 Frequency response of spiral antenna based communication link system

modulating input pulse laser with CCD signal which has shown in figure 6-3. The received signal after current amplifier is also shown in figure 6-3 and distortion result from bandwidth limitation could be observed.

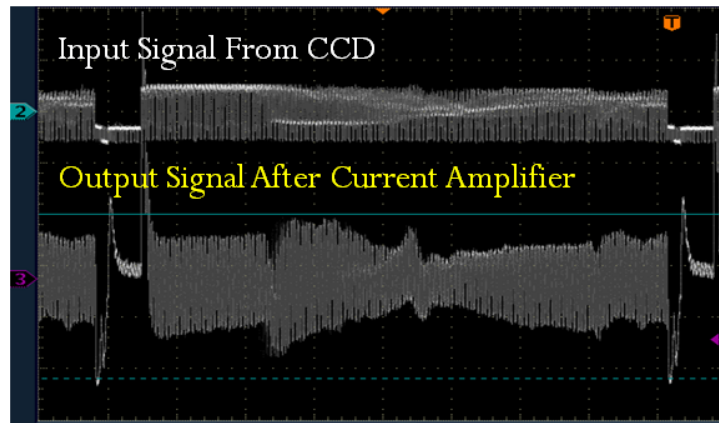


Figure 6- 3 The input image signal from CCD and received signal after current amplifier

◆ **Photonic transmitter and W-band power detector based system for Sub-THz communication link**

In order to avoid above bandwidth limitation, we further adopted photonic transmitter as emitter and w-band power detector as receiver to set up a communication link system, which is shown in figure 6-4.

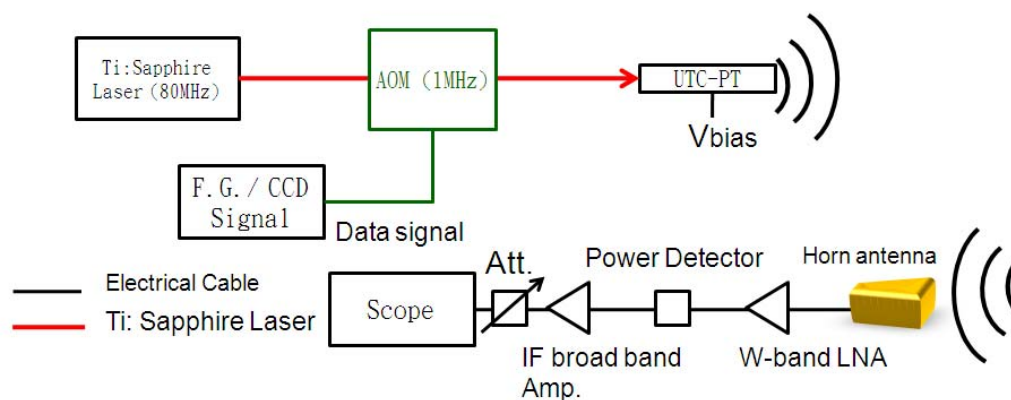
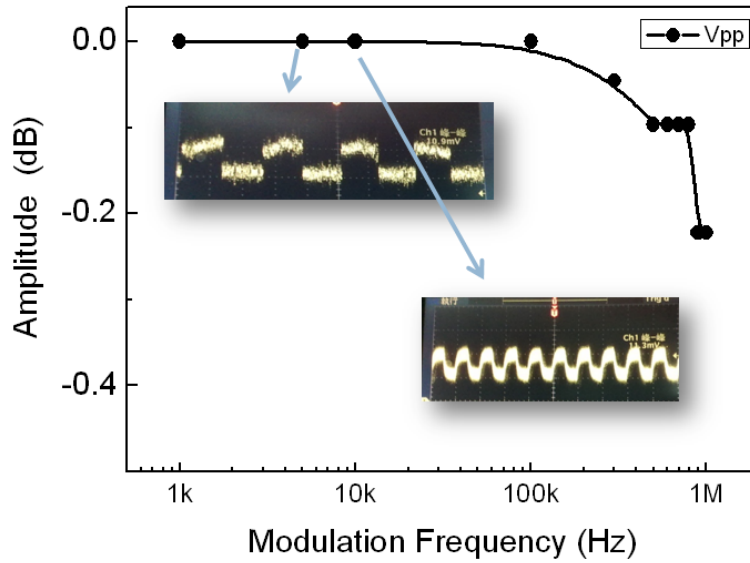


Figure 6- 4 Schematic diagram of sub-THz communication link system by using Photonic transmitter and W-band power detector



*Figure 6- 5 Frequency response of communication link based on photonic transmitter and W-band power detector*

The excitation pulse laser is also modulated by an AO modulator and we also detector the generated signal by w-band power detector (DXP08) which is connected with a horn antenna. After pass through low noise amplifier (LNA) and IF amplifier, the received modulated signal could be measured. The modulation bandwidth in this architecture is modulation speed (2MHz), which could be improved by using higher speed modulator. The frequency response of this communication is shown in figure 6-5 and a 3-dB modulation bandwidth higher than 1MHz could be measured.

### **6-3 Manchester Coding to Improve Link Reliability**

We also demonstrate the using of Manchester coding to enhance the reliability of ultra-wideband (UWB) – impulse radio (IR) transmission system through a broadband photoconductive (PC) antenna based time-domain spectrum system (TDS).(Figure 6-6)

A comparison between on-off-keying (OOK) signal and Manchester coding is introduced in figure 6-7 and figure 6-8. The spiral antenna based transmission system in the experiment is characterized has a center frequency of 50GHz and a broad bandwidth 250GHz (noise floor) which is shown in Figure 6-9.

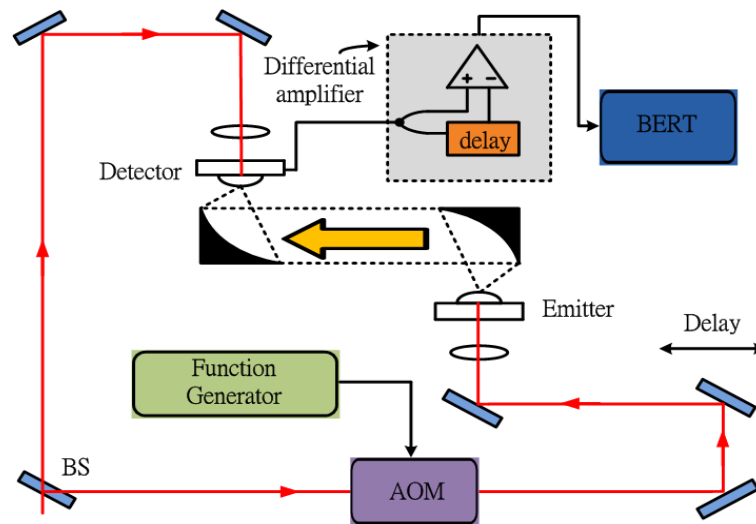


Figure 6- 6 The schematic experiment setup of TDS based transmission system

By using optical modulation, BER around  $10^{-9}$  is measured at transmission data rate 30kbit/s and raised rapidly while data rate increased up to 40 kbit/s in our system. Since the generated signals is higher under higher applied voltage, we also measured BER with the corresponding eye diagrams versus different bias voltage (3V ~ 15V) applied on emitter by using Manchester and OOK coding respectively under the same input power. The result shown in figure 6-10 and 6-11 shows that the receiver sensitivity can be greatly improved using Manchester coding rather than the conventional on-off-keying (OOK) coding in the same presence of turbulence

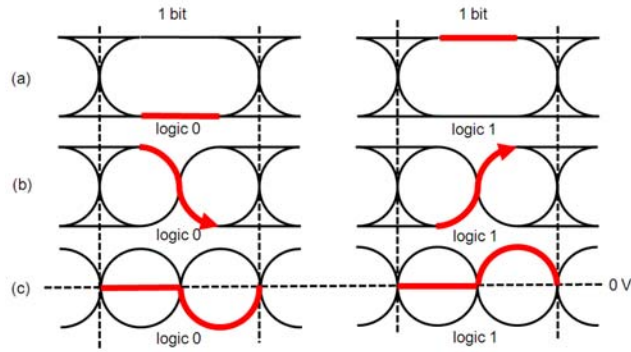


Figure 6- 7 Signal coding : (a) OOK coding (b) Manchester coding, and (c) differentially detected Manchester coding

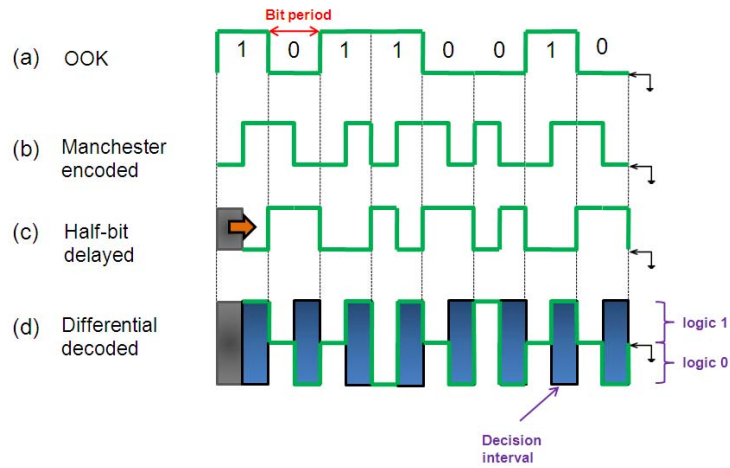


Figure 6- 8 Signal coding : (a) OOK coding (b) Manchester coding, (c) half-bit delayed and (d) differentially detected Manchester coding

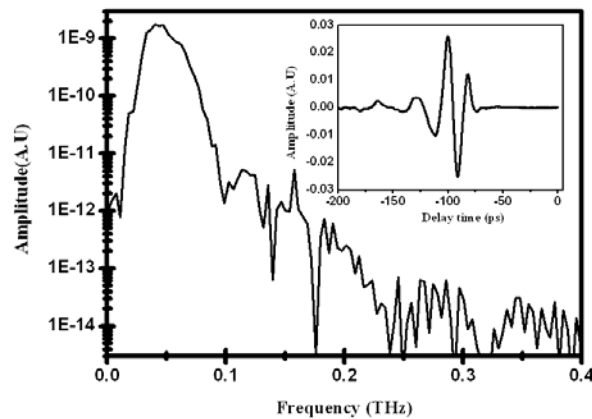


Figure 6- 9 Measured power spectrum and the inset shows the electrical field

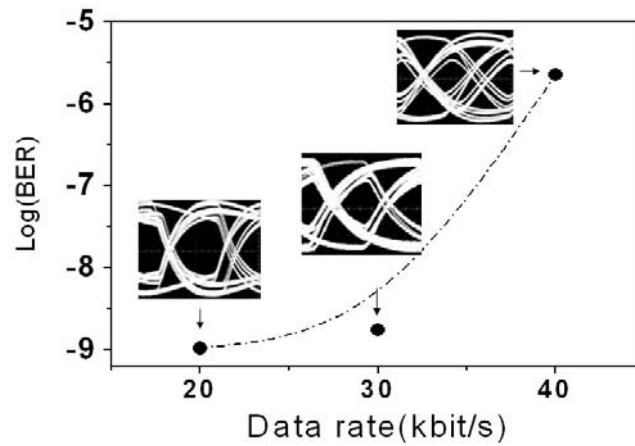


Figure 6- 10 Bit error rate (BER) versus data rate of OOK transmission in our system

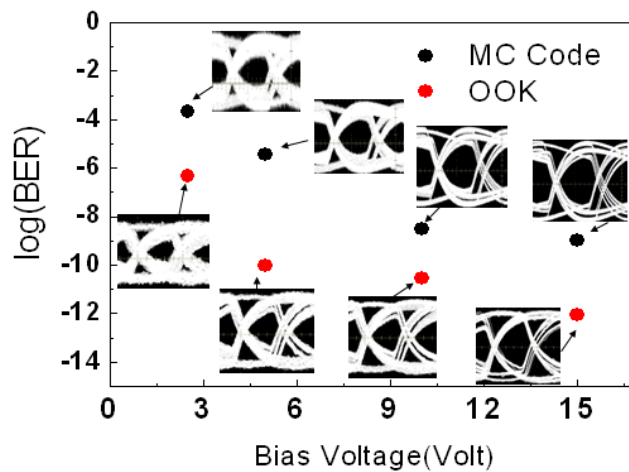
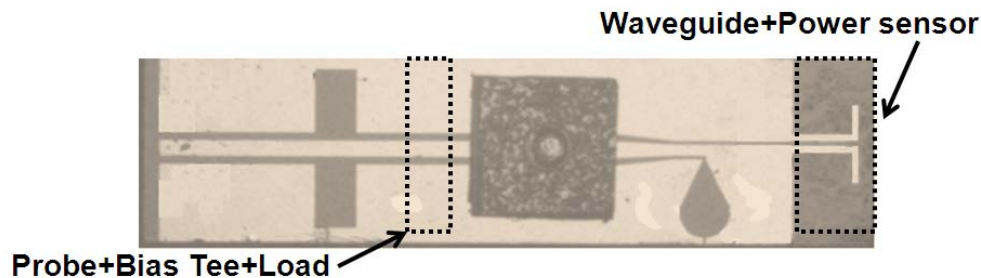


Figure 6- 11 Measured bit error rate (BER) versus different bias voltage applied on emitter by using Manchester and OOK coding respectively.

## 6-4 Impulse Radio Communication under 1550nm Wavelength

By using novel near-ballistic uni-traveling-carrier photodiodes (NBUTC-PDs) based W-band photonic transmitter [10] and a mode-locked laser with a 10GHz

repetition rate, 2.5Gbit/sec impulse-radio wireless data transmission at 100GHz with 3.3m maximum transmission distance have been demonstrated.



*Figure 6- 12 Top view of NBUTC-PT.*

Figures 6-12 shows the top-view of our novel photonic transmitter-mixer, a conceptual diagram of the WR-10 waveguide feeding, and a photograph of our device during measurement. As can be seen in Figure 6-12, the photonic transmitter-mixer is composed of a diced NBUTC-PD with a  $100\mu\text{m}^2$  active area, a planar quasi-yagi antenna, a fan-shaped broadband transition between the co-planar waveguide (CPW) and the coplanar slot-line (CPS), an IF signal input port, a W-band RF choke, and bond pads for flip-chip bonding process on a  $100\mu\text{m}$  thick aluminum-nitride (AlN) substrate for good thermal conductivity.

The schematic setup of impulse communication by optical and bias modulation can be seen in Figure 6-13 and 6-14 respectively. An on-wafer probe is used to input the 2.5Gbit/sec electrical signal and modulate the bias point of the device [11]. Here, we adopted both optical and bias modulation technique [11] to up-convert the 2.5Gbit/sec data to W-band frequency due to that it can re-generate the transmitted signal in base station and has potential to further increase the distance of fiber transmission [12].

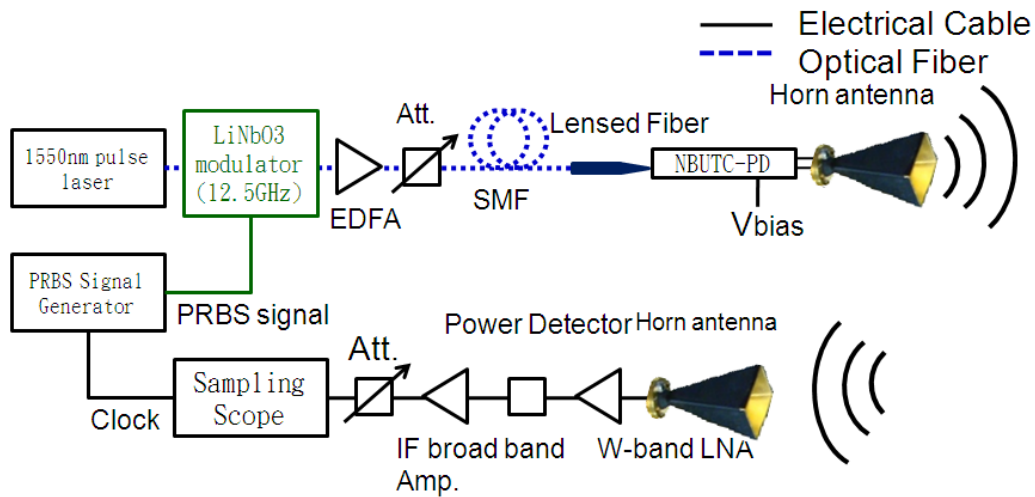


Figure 6- 13 A schematic setup of impulse communication link with optical modulation.

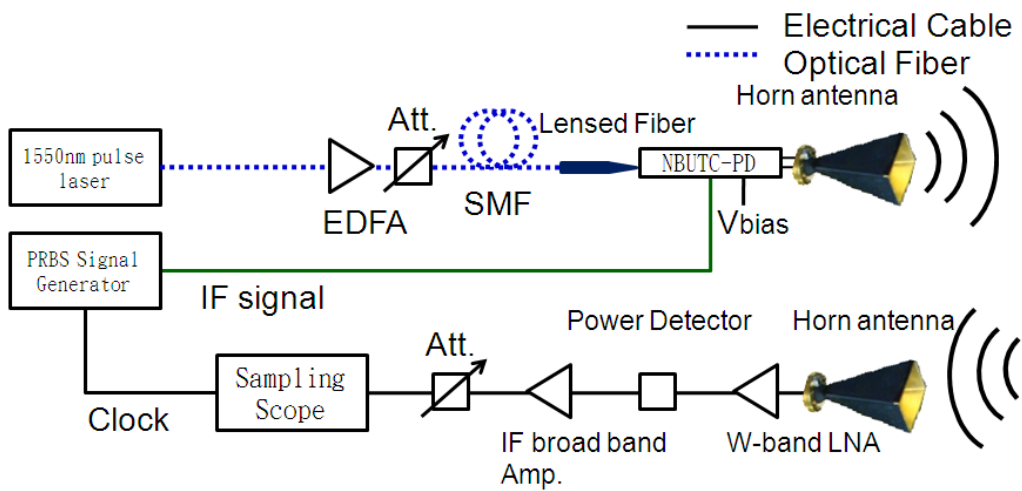
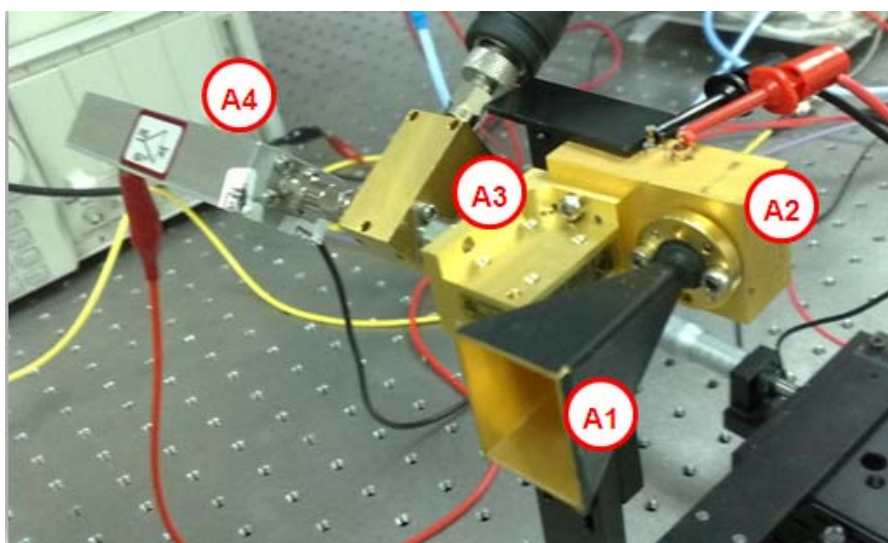


Figure 6- 14 A schematic setup of impulse communication link with bias modulation.

The optical pulse train, which has the Fourier-transformed frequency component around 100GHz, is injected onto the device through the use of a lens fiber and the up-converted (to W-band) data is then radiated through the W-band horn antenna. The optical pulse train with a 10GHz repetition rate is provided by a commercial fiber mode-locked laser. The inset shows the optical pulse shape after passing the EDFA measured by an autocorrelator. The full-width-half-maximum (FWHM) of pulse is around 2.2ps and corresponds to a 110GHz 3-dB bandwidth, which is suitable for our IR data transmission at W-band (75-110GHz). The 2.5Gbit/sec data with PRBS:215-1



is generated by the pattern generator and then fed into the IF input port of our photonic transmitter. The receiver end is composed of a W-band horn antenna, a W-band low-noise-amplifier (LNA), and a fast W-band power detector to detect the envelope of data. The signal detected by the power detector is boosted by an IF amplifier and then fed into a high-speed sampling scope. A picture of receiver end is shown in Fig. 6-15 which marked every components from horn antenna to IF amplifier with A1 to A4.



*Figure 6- 15 Picture of receiver end*

( A<sub>1</sub> : W band horn antenna, A<sub>2</sub>: LNA, A<sub>3</sub> Power detector, A<sub>4</sub> : IF amplifier)

Figure 6-16 (a), (b), (c) and (d) show the received MMW power spectrum through horn antenna, LNA, power detector and IF amplifier, respectively As can be seen, a significant power envelop exists around 100GHz in (a) and a clear IF spectrum with a 2.5Gbit/sec data rate in (c) and (d) can be observed. Figure 6-17 shows the measured bit-error-rate (BER) vs. wireless transmission distance under different conditions including modulation methods, transmission data rate and device current.

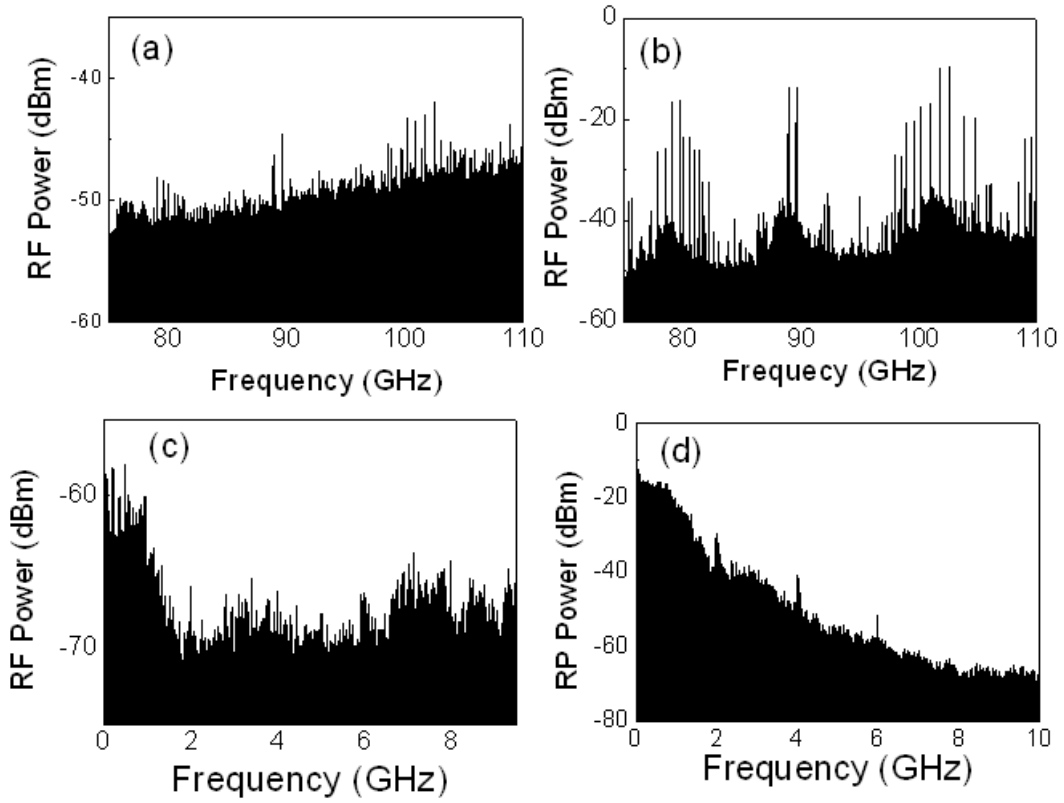


Figure 6- 16 Power spectrum measured at different position.

( a : after horn antenna, b : after LNA, c : after power detector, d : after IF amplifier)

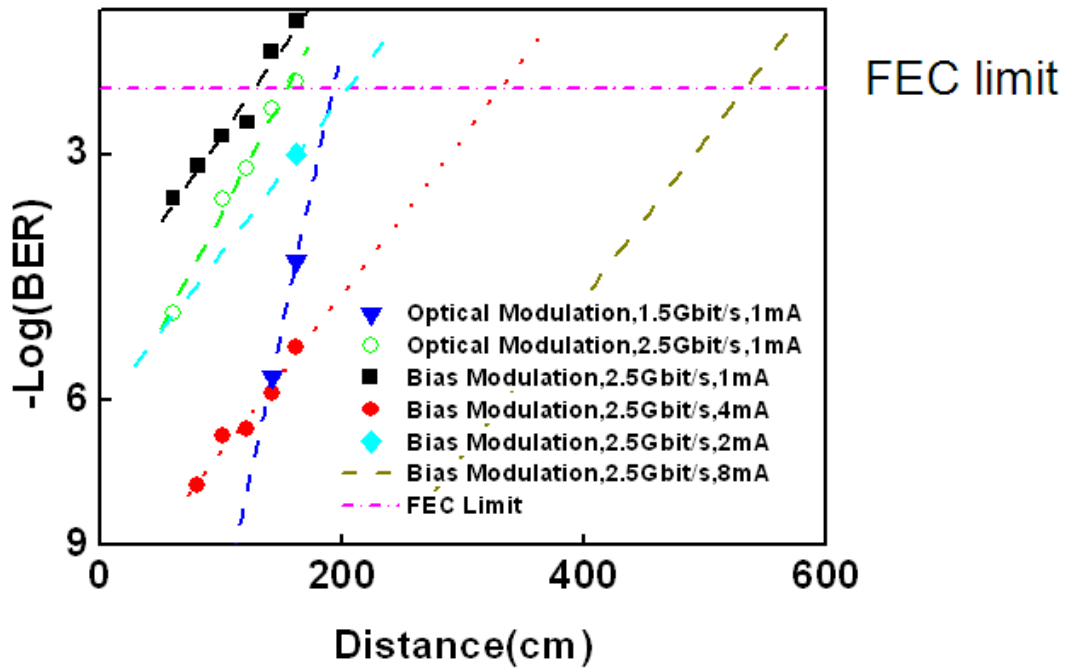


Figure 6- 17 BER versus distance under different modulation speed.

Under a high output averaged photocurrent ( $\sim 4\text{mA}$ ), the forward-error-correction (FEC,  $\text{BER}=3.84\times 10^{-3}$ ) [13] limited transmission distance is around 3.3m. The FEC limited maximum transmission distance for 2.5Gbits/s data rate could be expected is around 550m while output average current is around 8mA.

## Reference

- [1] M. Z. Win, and R. A. Scholtz, "Impulse radio: how it works," *IEEE Commun. Lett.* 2, 36-38, 1998.
- [2] M. Ghavami, L. B. Michael, and R. Kohno, *Ultra Wideband Signals and Systems in Communication Engineering*, Second Edition, John Wiley & Sons, Ltd, 2007
- [3] R. J. –M. Cramer, M. Z. Win, and R. A. Scholtz, "Impulse radio multipath characteristics and diversity reception," *Proc. of ICC*, Atlanta, GA, USA, 3, 1650-1654, 1998.
- [4] E. E. Funk and C. H. Lee, "Free-space power combining and beam steering of ultra-wideband radiation using an array of laser-triggered antennas," *IEEE Trans. Microwave Theory Tech.* 44, 2039–2042, 1996.
- [5] E. E. Funk, S. Ramsey, C. H. Lee, "A photoconductive correlation receiver for time-hopped wireless spread-spectrum radio," *IEEE Microwave and Guided Wave Lett.* 8, 229-231, 1998.
- [6] E. R. Mueller, and A. J. DeMaria, "Broad bandwidth communication/data links using terahertz sources and Schottky diode modulators/detectors," *Proc. of SPIE* 5727, 151-165, 2005.
- [7] T. Kleine-Ostmann, K. Pierz, G. Hein, P. Dawson, and M. Koch, "Audio signal transmission over THz communication channel using semiconductor modulator," *Electron. Lett.* 40, 124-126, 2004.
- [8] L. Moller, J. Federici, A. Sinyukov, C. Xie, H. C. Lim, and R. C. Giles, "Data encoding on terahertz signals for communication and sensing," *Opt. Lett.* 33, 393-395, 2008.

- [9] T. A. Liu, G. R. Lin, Y. C. Chang, C. L. Pan, "Wireless audio and burst communication link with directly modulated THz photoconductive antenna," *Opt. Express*, vol. 13, pp. 10416-10423, 2005.
- [10] Y.-S. Wu, Nan-Wei Chen and J.-W Shi, "A W-Band Photonic Transmitter/Mixer Based on High-Power Near Ballistic Uni-Traveling Carrier Photodiodes (NBUTC-PD)," *IEEE Photon. Technol. Lett.*, vol. 20, pp. 1799-1801, Nov. 1, 2008.
- [11] A. Hirata, T. Furuta, H. Ito, and T. Nagatsuma, "10-Gb/s millimeter-wave signal generation using photodiode bias modulation," *J. of Lightwave Technol.*, vol. 24, pp. 1725-1731, April, 2006.
- [12] H.-C. Chien, A. Chowdhury, Z. Jai, Y.-T. Hsueh, and G.-K. Chang, "Long-Reach 60-GHz Mm-Wave Optical-Wireless Access Network Using Remote Signal Regeneration and Upconversion," in *Proc. ECOC 2008*, Brussels, Belgium, Germany, Sep., 2008, vol. 2, pp. 137-138.
- [13] J. Cartledge, D. Krause, K. Roberts, C. Laperle, D. McGhan, H. Sun, K.-T. Wu, M. Osullivan, and Y. Jiang. "Electronic Signal Processing for Fiber-Optic Communication," *IEEE LEOS NEWSLETTER*, vol. 23, no. 1, pp. 11-15, Feb., 2009.

# Chapter 7 Conclusion and Future Work

## 7-1 Conclusion

In conclusion, several key components of optical-electrical devices for THz and Sub-THz range (0.1~1THz) are demonstrated, which include photoconductive (PC) antennas and photonic transmitters (PTs). First, we demonstrated a photonic-transmitter under PM operations, composed of an STR-PD and a micromachined slot antenna but without the integration with a Si-lens. A strong sub-THz radiation was measured at the designed resonant frequency ( 500 GHz) by the FTIR system. Furthermore, the saturation problem of the radiated THz power, that occurs when a traditional LTG-GaAs-based photomixer is operated under a high reverse bias voltage, has been eliminated. Next, we studied the dynamic behavior of a PT constructed by monolithically integrating a GaAs–AlGaAs-based UTC-PD with a substrate-removed circular disc monopole antenna. The PT radiated sub-THz pulses less than 2 ps in width, with peak power as high as 20 mW and a wide bandwidth (beyond 250 GHz).

In order to further study the performance of these two photo diodes, we investigated in detail the dynamic behaviors of two high-power PTs, which were constructed by monolithically integrating GaAs/AlGaAs-based UTC-PDs and STR-PDs with the same substrate-removed monopole antenna, by use of the THz-TDS system. By shortening the effective carrier drift-distance and increasing the carrier drift-velocity in the STR-PD and UTC-PD we could obtain PT radiated sub-THz pulses with peak powers as high as 8mW and a wide bandwidth (around

250GHz). Furthermore, the output power performance and speed of the STR-PT were comparable to those of the UTC-PT under a much lower operation current, which may minimize the thermal problems encountered under high-power operation. The strong bias dependent high-peak-power performance and excellent linearity of these two devices suggests their suitability for application as photonic emitters and possibly as data modulators in sub-THz IR communication systems.

In the discussion of PC antenna, we compared the emission properties of LT-GaAs photoconductive (PC) antennas with GaAs:O fabricated condition ( $2.5 \times 10^{13}$  ions/cm<sup>2</sup> (500 keV & 800 keV),  $4 \times 10^{13}$  ions/cm<sup>2</sup> (1200 keV)) in the pulse and CW mode. The material GaAs:O can generate higher THz power than LT-GaAs both in pulsed mode and CW mode. The bandwidth of GaAs:O and LT-GaAs are measured about 1THz both under pulse (TDS) and CW (photomixing) pumping. The result shows that GaAs:O is a proper THz emitter material compare with LT-GaAs which is hardly to reproduce.

Finally, we demonstrate sub-THz communication link by using photonic transmitters and PC antenna as emitters respectively, and measure frequency response of system, which provide us important previous work for future application. The feasibility of using Manchester coding to improve the THz transmission is also shown base on the PC antennas based TDS system. Numerical analysis comparing both conventional on-off-keying (OOK) and Manchester coded transmissions shows that Manchester coding can provide significant improvement in the presence atmospheric turbulence effects.

## 7-2 Future Work

Although we have successfully demonstrated high power sub-THz photonic devices under pulse laser excitation with wavelength of 800nm, there are still some problems need to overcome in a real system of application. We can discuss it in several aspects such as improvement of emitter, excitation laser sources and receivers. In the part of improvement of emitters, lower operation voltage of UTC-PD compared with STR-PD could be attributed to damage caused by thermal effect under high power excitation. To solve this problem, a combination UTC-PD with  $\text{Al}_2\text{N}_3$  substrate which has better heat sink performance could be adopted. Such combination could increase radiation power of devices by reducing thermal effect under high power excitation.

In the part of excitation sources, although Ti:Sapphire laser provide us narrow pulse width and high peak power excitation source, there are still some unavoidable problems. For example, cost, volume and pulses repetition rate of Ti: Sapphire laser may be an important restriction for real communication application. The decrease of cost and volume of Ti Sapphire laser may achieved in the future and increasing of repetition rate of Ti : Sapphire laser has also be demonstrated up to 1.5GHz by injection. However, the best solution so far may be using 1550 nm wavelength pulse laser source with high repetition rate up to 1~ 10GHz which has smaller volume compared with Ti : Sapphire laser. The drawback of the source is broader pulse width compared with Ti: Sapphire laser, which is acceptable so far for our communication using.

In the part of receivers, it plays an important role for our communication experiment. LTG-GaAs based photo conductive antennas can receive broadband



radiation signal (0.1~1 THz) but has poor modulation speed due to its printed antenna RC design, which may be improved by change its structure. However, although such photoconductive correlation receiver detection provides us a large dynamic range in the presence of noise and interference, it still has some problem to general communication application. For example, the gating signal is needed for receiver end to decode.

The high frequency power detector with high modulation speed to serve as receive end maybe a good approach. In our research result, we have successfully demonstrated wireless communication with 2.5Gbits/s data rate using a conventional W band power detector. However, the bandwidth limitation above 100GHz is still an obstacle for available electrical detector. The utilization of home-made electrical detector or EO sampling method may be an alternative method to solve the problem. Besides, a novel coding method to improve the performance of impulse communication is also needed, especially for such ultra wide band communication. Influence of dispersion in fiber for data transmission could be expected a serious problem, which could become a key issue for future application.

# Appendix A

Table 3 Detail epitaxial structure of UTC-PD

#	Material	Doping level	Thickness	Description
10	P+-In <sub>0.1</sub> Ga <sub>0.9</sub> As	$>5 \times 10^{19} \text{ cm}^{-3}$	80nm	For the ohmic contact, (Doping density as high as possible)
9	P+-Al <sub>0.2</sub> Ga <sub>0.8</sub> As	$5 \times 10^{19} \text{ cm}^{-3}$	500nm	Top cladding layer, T <sub>g</sub> =normal temperature grown
8	P+-GaAs	1.Top: $1 \times 10^{19} \text{ cm}^{-3}$ 2.5 $\times 10^{18} \text{ cm}^{-3}$ 3.1 $\times 10^{18} \text{ cm}^{-3}$ 4.Bottom: 5.5 $\times 10^{17} \text{ cm}^{-3}$	140nm	Step doping : 1. Top (Highest doping) 2. Bottom Least Doping density
7	N+-Al <sub>0.12</sub> Ga <sub>0.88</sub> As layer	$5 \times 10^{18} \text{ cm}^{-3}$	10nm	Cliff Layer
6	N- Al <sub>0.12</sub> Ga <sub>0.88</sub> As layer	$3 \times 10^{16} \text{ cm}^{-3}$	250nm	Collector Layer
5	N+-Al <sub>0.12</sub> Ga <sub>0.88</sub> As	$5 \times 10^{19} \text{ cm}^{-3}$	300nm	Bottom ohmic contact (Doping density as high as possible)
4	N+-Al <sub>0.25</sub> Ga <sub>0.75</sub> As	$1 \times 10^{19} \text{ cm}^{-3}$	400nm	Bottom cladding layer
3	Al <sub>0.5</sub> Ga <sub>0.5</sub> As	Undoped	2000nm	Optical isolation layer
2	GaAs	Undoped	200nm	Buffer layer
1	S.I. GaAs			Substrate

Table 4 Detail epitaxial structure of STR-PD

T<sub>g</sub> : the growth temperature

T<sub>a</sub> : the annealing temperature

#	Material	Doping level	Thickness	Description
13	P+-In <sub>0.15</sub> Ga <sub>0.85</sub> As	>3 *10 <sup>19</sup> cm <sup>-3</sup> (as high as possible)	20nm	For the ohmic contact ; T <sub>g</sub> = normal temperature grown (600~700°C) (As overpressure)
12	P+-Al <sub>0.2</sub> Ga <sub>0.8</sub> As	3 *10 <sup>18</sup> cm <sup>-3</sup>	400nm	Top cladding layer ; T <sub>g</sub> = normal temperature grown (600~700°C) (As overpressure)
11	P+-Graded layer	3 *10 <sup>18</sup> cm <sup>-3</sup>	20nm	From 0% Al to 20% Al ; T <sub>g</sub> = normal temperature grown (600~700°C) (As overpressure)
10	GaAs	Undoped	50nm	Absorption Layer T <sub>g</sub> = normal temperature ; (As overpressure)
9	AlAs	Undoped	1.5nm	Top diffusion barrier of excess As , T <sub>g</sub> = normal temperature (600~700°C) ; (As overpressure)
8	LT-GaAs	Undoped	150nm	<u>T<sub>g</sub>~200°C</u> (by thermal couple) ; If the growth time of above epi-layers (N+ layers) is less than 30 min , please anneal this layer 10 min. with 600C and As overpressure condition.
7	AlAs	Undoped	1.5nm	Bottom diffusion barrier of excess As , T <sub>g</sub> = normal temperature ;
6	GaAs	Undoped	50nm	Absorption layer
5	N+-Graded layer	1 *10 <sup>19</sup> cm <sup>-3</sup>	20nm	From 30% Al to 0% Al , T <sub>g</sub> = normal temperature grown
4	N+-Al <sub>0.15</sub> Ga <sub>0.85</sub> As	>3 *10 <sup>18</sup> cm <sup>-3</sup>	400nm	The ohmic contact ; Bottom cladding layer T <sub>g</sub> = normal temperature grown
3	Al <sub>0.5</sub> Ga <sub>0.5</sub> As	Undoped	2000nm	Optical isolation layers
2	GaAs	Undoped	200nm	Buffer layer
1	S.I. GaAs			Substrate

# Publication list

## Journal list:

1. Yu-Ping Lan, Yea-Feng Lin, Yu-Tai Li, Ru-Pin Pan, Chao-Kuei Lee and Ci-Ling Pan” Intracavity measurement of liquid crystal layer thickness by wavelength tuning of an external cavity laser diode” ,*Opt. Express*, Vol. 13, No. 20, pp. 7912 October 3, 2005.
2. Jin-Wei Shi , Yu-Tai Li, Ci-Ling Pan, M. L. Lin, Y. S. Wu, W. S. Liu, and J.-I. Chyi ,” Bandwidth enhancement phenomenon of a high-speed GaAs–AlGaAs based untravelling carrier photodiode with an optimally designed absorption layer at an 830 nm wavelength”, *Appl. Phys. Lett.*, 89, 053512, 2006.
3. Hung-Wen Chen, Yu-Tai Li, Jeng-Liang Kuo, Ja-Yu Lu, Li-Jin Chen, Ci-Ling Pan, and Chi-Kuang Sun “Investigation on Spectral Loss Characteristics of Subwavelength THz Fibers.” *Opt. Letters.*, 32 (9), 1017-1019 (2007), selected by *Virtual Journal of THz Science and Technology*, May 2007 .
4. Yu-Tai Li, J.-W. Shi, Ci-Ling Pan, C.-H. Chiu, W.- S. Liu, Nan-Wei Chen, C.-K. Sun, and J.-I. Chyi “Sub-THz Photonic-Transmitters Based on Separated-Transport-Recombination Photodiodes and a Micromachined Slot Antenna.” *IEEE Photon. Technol. Lett.*, 19 (11), 840-842 (2007), selected by *Virtual Journal of THz Science and Technology*, June 2007
5. Tzu-Ming Liu, Ja-Yu Lu, Hung-Ping Chen, Chung-Chiu Kuo, Meng-Ju Yang, Chih-Wei Lai, Pi-Tai Chou, Ming-Hao Chang, Hsiang-Lin Liu, Yu-Tai Li, Ci-Ling Pan, Shih-Hung Lin, Chieh-Hsiung Kuan, and Chi-Kuang Sun, “Resonance-enhanced dipolar interaction between terahertz photons and confined acoustic phonons in nanocrystals,” *Appl. Phys. Lett.*, Vol. 92, art. 093122, 3 March 2008.
6. Ja-Yu Lu, Chin-Ping Yu, Hung-Chung Chang, Hung-Wen Chen, Yu-Tai Li, Ci-Ling Pan, and Chi-Kuang Sun, “Terahertz air-core microstructure fiber,” *Appl. Phys. Lett.* Vol. 92, art. 064105, 11 February 2008.
7. Chia-Jen Lin, Yu-Tai Li, Cho-Fan Hsieh, Ru-Pin Pan, and Ci-Ling Pan, "Manipulating Terahertz Wave by a Magnetically Tunable Liquid Crystal Phase Grating," *Opt. Exp.*, Vol. 16, No. 5, pp. 2995-3001, 3 March 2008.
8. Yu-tai Li, J.-W. Shi, C.-Y. Huang, N.-W. Chen, S-H Chen , J-I Chyi and Ci-Ling Pan, “Characterization of Sub-THz Photonic-Transmitters Based on GaAs/AlGaAs Uni-Travelling Carrier Photodiodes and Micromachined Broadband

- Antennas for Ultra-wideband Communication, *IEEE Photon. Technol. Lett.*, Vol 20, No. 16, pp. 1342-1344, 15 August 2008.
9. Ke-jian Chen, Yu-tai Li, Mong-huan Yang, Wing Yiu Cheung, Ci-Ling Pan, Kam Tai Chan, "Comparison of CW terahertz wave generation and bias-field-dependent saturation in GaAs:O and LT-GaAs antennas," *Opt. Lett.*, Vol. 34, Issue 7, pp. 935-937, April 1, 2009.
  10. Yu-Tai Li, J.-W. Shi, C.-Y. Huang, N.-W. Chen, S.-H. Chen, J.-I. Chyi, Yi-Chao Wang, Chan-Shan Yang and Ci-Ling Pan, "Characterization and Comparison of GaAs/AlGaAs Uni-Traveling Carrier and Separated-Transport-Recombination Photodiode Based High-Power Sub-THz Photonic-Transmitters," Accepted for Publication by *IEEE J. Quantum Electron.*, May 8, 2009.
  11. Chia-Jen Lin, Chuan-Hsien Lin, Yu-Tai Li, Ru-Pin Pan, and Ci-Ling Pan, "Electrically Controlled Liquid Crystal Phase Grating for Terahertz Waves," *IEEE Photon. Technol. Lett.*, Vol. 21, No.11, June 1, 2009.

## Conference List:

### Internal conference

1. Jin-Wei Shi, Yu-Tai Li, Ci-Ling Pan, M.-L. Lin, Y.-S. Wu, W.-S. Liu, J.-I. Chyi; "Separated-Transport-Recombination p-i-n Photodiode (STR-PD) with High-Speed and High-Power Performance under Continuous-Wave (CW) Operation," paper CTuS6, presented at CLEO/QELS 2006, Long Beach, California, May 21-26, 2006.
2. Wei-Wen Wang , Yu-Tai Li, Ci-Ling Pan, "THz Radiation Characteristics of the Photonic-Transmitters Based on Separated-Transport-Recombination Photodiode and Micromachined Slots Antenna," P7, presented at AP-THz 2006 (Asian-Pacific THz Photonics Workshop), Dec. 14, 2006, Hsinchu, Taiwan .
3. Hung-Wen Chen, Ja-Yu Lu, Jeng-Liang Kuo , Yu-Tai Li , Ci-Ling Pan,, Li-Jin Chen, Po-Jui Chiang, Hung-Chun Chang, and Chi-Kuang Sun "Terahertz fiber-based coupler " P3, *ibid.*.
4. Ja-Yu Lu, Yu-Tai Li, Ci-Ling Pan, Chin-Ping Yu, Hung-Chung Chang, Hung-Wen Chen, and Chi-Kuang Sun "Air-core microstructure fiber for terahertz radiation waveguiding," P4, *ibid.*.
5. Hung-Wen Chen, Ja-Yu Lu, Jeng-Liang Kuo , Yu-Tai Li, Ci-Ling Pan, Li-Jin Chen, and Chi-Kuang Sun" Study on attenuation spectrum of subwavelength-diameter thz fibers"P5, *ibid.*.
6. Chia-Jen Lin, Yu-Tai Li , Cho-Fan Hsien, Ru-Pin Pan, and Ci-Ling Pan, "Magnetically controlled liquid crystal terahertz tunable phase grating"P10,

ibid..

7. Jin-Wei Shi, Yu-Tai Li, Ci-Ling Pan, C.-H. Chiu, W.- S. Liu and J.-I. Chyi,” Characterization of a sub-THz photonic transmitter based on a separated-transport-recombination photodiode”, presented at CLEO/QELS 2007 in Baltimore, Maryland, May 6-11, 2007.
8. Ke-jian Chen, Yu-tai Li, WingY-iu Cheung, Wei-wen Wang, Ci-Ling Pan, and Kam Tai Chan, “CW Sub-Terahertz wave generation by GaAs:O Materials,” paper FH1-5, presented at CLEO/Pacific Rim 2007, Seoul, Korea, August 26 - 31, 2007
9. Ke-jian Chen, Yu-tai Li, Wing-yiu Cheung, Wei-wen Wang, Ci-ling Pan, Kam-tai Chan, “THz waves generated by oxygen implanted GaAs”, paper 1C5-5, presented at ISAP2007, Niigata, Japan, August 20-24, 2007
10. Yu-Tai Li, Ci-Ling Pan, J.-W. Shi, Cheng-Yu Huang, Nan-Wei Chen, Shu-Han Chen, J.-i. Chyi, “Sub-THz Photonic-Transmitters Based on GaAs/AlGaAs Uni-Traveling Carrier Photodiode and Micromachined Circular Disk Monopole Antenna for Ultra-Wideband Communication” presented at CLEO/QELS 2008 in San Jose, California, May 4-12, 2008.
11. Yu-Tai Li, Chan-Shan Yang, Ci-Ling Pan, Jin-Wei Shi, C.-Y. Huang, N.-W. Chen, S.-H. Chen, J.-I. Chyi, “Distinct Dynamic Behaviors of High-Power Photonic-Transmitters Based on Uni-Traveling Carrier and Separated-Transport-Recombination Photodiodes”, poster presentation at CLEO/IQEC in Baltimore, May 31-June 5, 2009.

#### **Local Conference:**

1. Yu-Tai Li, Yu-Ping Lan, Yea-Feng Lin, Ru-Pin Pan, Chao-Kuei Lee, Ci-Ling Pan,” Liquid Crystal layer Thickness Measurement By Monitoring Wavelength Change Of An External Cavity Laser Diode” OPT, Taiwan, 2005.
2. Yu-Tai Li, Yu-Ping Lan, Yea-Feng Lin, Ru-Pin Pan, Chao-Kuei Lee, Ci-Ling Pan And Chih-Yu Wang,” Measurement Of Liquid Crystal Layer Thickness By Monitoring Wavelength Change of An External Caviety Layser Diode” Annual Meeting of ROC Taiwan Liquid Crystal Society, Taiwan,2005.
3. Yu-Tai Li, Wei-Wen Wang, Ci-Ling Pan,” Sub-THz Photonic-Transmission Based on Speared-Transport-Recombination Photodide and Micromachined Slot Antenna,” AO-40,presented at OPT2006 (Optics and Photonics Taiwan) ,Dec.15 - 16, 2006, Hsinchu, Taiwan.
4. Ja-Yu Lu, Yu-Tai Li, Ci-Ling Pan, Chin-Ping Yu, Hung-Chung Chang, Hung-Wen Chen, and Chi-Kuang Sun “Air-Core Microstructure Fiber for Terahertz Radiation Waveguide,” presented at OPT2006 (Optics and Photonics Taiwan),Dec.15-16, 2006,Hsinchu, Taiwan

5. Hung-Wen Chen, Ja-Yu Lu, and Li-Jin Chen, Yu-Tai Li, Ci-Ling Pan, Jeng-Liang Kuo and Chi-Kuang Sun” Study on Attenuation Spectrum of Subwavelength-Diameter THZ Fibers” presented at OPT2006 (Optics and Photonics Taiwan), Dec.15-16, 2006, Hsinchu, Taiwan
6. C.-H. Chiu, Jin-Wei Shi, Yu-Tai Li, Y.-S. Wu, W.-S. Liu, J.-I. Chyi, and Ci-Ling Pan,” High-Speed GaAs-AlGaAs Based Unitraveling-Carrier Photodiodes at 830nm Wavelength Regime” presented at OPT2006 (Optics and Photonics Taiwan), Dec.15-16, 2006, Hsinchu, Taiwan
7. Hung-Wen Chen, Ja-Yu Lu, Li-Jin Chen, Po-Jui Chiang, Hung-Chun Chang, Yu-Tai Li, Ci-Ling Pan, Jeng-Liang Kuo and Chi-Kuang Sun “TERAHERTZ FIBER COUPLER ” presented at OPT2006 (Optics and Photonics Taiwan), Dec.15-16, 2006, Hsinchu, Taiwan
8. Chia-Jen Lin, Yu-Tai Li, Cho-Fan Hsieh, Ru-Pin Pan and Ci-Ling Pan, “Tunable Liquid Crystal Phase Grating for Terahertz Beam Splitting”, aE-05, presented at Annual Meeting of the Physical Society, Jan. 28-30, 2008, Hsinchu, Taiwan.
9. Chia-Jen Lin, Yu-Tai Li, Cho-Fan Hsieh and Ru-Pin Pan and Ci-Ling Pan, “Tunable Liquid Crystal Phase Grating for Terahertz Beam Splitting”, aE-05, presented at Annual Meeting of the Physical Society, Jan. 28-30, 2008, Hsinchu, Taiwan.
10. M. H. Yang, Y. T. Li, and Chi Wai Chow and Ci Ling Pan , “利用電光取樣在自由空間下偵測聲光調制之兆赫波通訊傳輸特性”, , paper PE-16, presented at Annual Meeting of the Physical Society, Jan. 28-30, 2008, Hsinchu, Taiwan.
11. Y.T. Li nd W.W. Wang and C.L. Pan and K.J. Chen and J.T. Chen , “低溫成長砷化鎵與多重氧離子佈植砷化鎵光導天線之 THZ 輻射特性之比較” paper CO-004, presented at Annual Meeting of the Optics and Photonics in Taiwan, Nov. 30-Dec.1, 2007, Taichung, Taiwan.
12. C.W. He, Y.L. Lin, Y.T. Li and Ci Ling Pan, Hyeyoung Ahn, K.J. Chen and K.T. Chan, ”CW THz Radiation Generated by Oxygen-ion-implanted GaAs Photoconductive Antenna”, paper PE-67, presented at Annual Meeting of the Physical Society, Jan. 28-30, 2008, Hsinchu, Taiwan.

# Curriculum Vita

## Personal Data:

**Name:** Yu-Tai Li (黎宇泰)

**Data of Birth:** June 13<sup>th</sup>, 1980

**Sex:** Male

**Nationality:** Taiwan (R.O.C.)

**E-mail:** li.liyutai@gmail.com



## Education:

9/2004~ 6/2009 **Ph.D.** in Department of Photonics, National Chiao-Tung University, Hsinchu, Taiwan.

9/2002~6/2004 **M.S.** in Department of Electrophysics, National Chiao-Tung University, Hsinchu, Taiwan.

9/1998~6/2002 **B.S.** in Department of Power Mechanical Engineering, National Tsing-Hua University, Hsinchu, Taiwan.

## Research Experience :

2007~2009 Sub THz wireless communication link

**IMPACT:** 2.5Gbits/s data rate of W band impulse wireless communication link is demonstrated. To the best of author's knowledge, this is the highest data rate even reported for W-band photonic IR communication system.

2005~2007 High speed, high power photonic transmitter investigation

**IMPACT:** Novel sub-THz PTs including UTC-PTs and STR-PTs exciting by Ti:Sapphire Laser are demonstrated and compared in detail.

2004~2005 THz component measurement and investigation.

**IMPACT:** We demonstrate a STR-PT which could radiate high peak power at frequency around 500 GHz, which also eliminate life time increasing effect successfully.

2002~2004 Liquid Crystal Physics,

**IMPACT:** Small and multi area alignment is demonstrated by pulling an etched fiber tip, which is useful for specific OE devices fabrication.

## Honor and Award

2007 Student Paper Award, Optics & Photonics Taiwan



2006 Student Research Award of Ph.D. Student, Department of Photonics, National Chiao-Tung University.

2004 : Member, the Phi Tau Phi Honor Society 斐陶斐榮譽學會.

2003: President's List, Department of Electrophysics, National Chiao-Tung University,